Right Ventricular Biomechanics in Pulmonary Hypertension

by

Danial Sharifikia

BSc, K. N. Toosi University of Technology, 2015

MSc, State University of New York at Binghamton, 2017

Submitted to the Graduate Faculty of the

Swanson School of Engineering in partial fulfillment

of the requirements for the degree of

Doctor of Philosophy

University of Pittsburgh

2020

UNIVERSITY OF PITTSBURGH

SWANSON SCHOOL OF ENGINEERING

This dissertation was presented

by

Danial Sharifikia

It was defended on

October 30, 2020

and approved by

Marc A. Simon, MD, MS, Associate Professor, Departments of Medicine, Bioengineering, Clinical and Translational Science

Kang Kim, PhD, Associate Professor, Departments of Bioengineering, Medicine, Mechanical Engineering and Materials Science

Steven Abramowitch, PhD, Associate Professor, Department of Bioengineering and Clinical and Translational Science Institute

Spandan Maiti, PhD, Assistant Professor, Departments of Bioengineering, Mechanical Engineering and Materials Science

Dissertation Co-Director: Marc A. Simon, MD, MS, Associate Professor, Departments of Medicine, Bioengineering, Clinical and Translational Science

Dissertation Co-Director: Kang Kim, PhD, Associate Professor, Departments of Bioengineering, Medicine, Mechanical Engineering and Materials Science

Right Ventricular Biomechanics in Pulmonary Hypertension

Danial Sharifikia, PhD

University of Pittsburgh, 2020

Pulmonary hypertension (PH) is a disease resulting in increased right ventricular (RV) afterload, myocardial hypertrophy and ventricular remodeling. RV failure remains the main cause of mortality for nearly 70% of PH patients, with 33-38% mortality rates 3 years post-diagnosis. RV biomechanics has been closely linked to physiological function. From a biomechanical perspective, pressure overloaded RV myocardium experiences increased wall thickness, fiber remodeling and increased stiffness to restore the cardiac output.

Despite the development of multiple therapeutics for management of PH, lung transplantation remains the only curative treatment. Moreover, age-related differences exist in the survival rates of PH patients and although the current evidence suggests an association between PH and aging, limited data exist on age-associated differences in RV biomechanical properties.

A major biomechanical remodeling event experienced by the pressure overloaded RV is the reorientation of myofibers forming the RV tissue, which results in altered biomechanical properties and function. However, RV wall thickness in human patients and large animal models complicates the study of fiber reorientation throughout the RV thickness, mainly due to the limited imaging depth of current modalities such as confocal or multi-photon microscopy.

In this work, we aimed to evaluate the effects of a novel dual-acting heart failure therapeutic (Sacubitril/Valsartan) on RV remodeling in PH. Additionally, we analyzed the effects of aging on RV structure and biomechanics. Moreover, an ultrasound image processing

framework, coupled with computational models, was utilized to study the effects of different loading scenarios on the reorientation patterns of RV myofibers.

Our results showed that Sacubitril/Valsartan has the potential to prevent maladaptive RV remodeling in a pressure overload model via amelioration of RV pressure rise, hypertrophy, collagen and myofiber re-orientation as well as RV stiffening both at the tissue and myofiber-level. Additionally, our findings demonstrated the potential of healthy aging to modulate RV remodeling via increased peak pressures, cardiomyocyte loss, fiber reorientation, and altered collagen/myofiber stiffness. The developed ultrasound imaging framework effectively characterized the transmural orientation of RV myofibers. Computational models demonstrated that chronic pressure overload, but not solely an acute rise in pressures, results in kinematic shift of RV fibers towards the longitudinal direction.

Table of Contents

1.0 Introduction 1

1.1 Motivation 1

1.2 Objectives 2

1.3 Organization of Dissertation 3

2.0 Background 4

2.1 The Right Ventricle (RV) 4

2.1.1 Organ-Level RV Biomechanics 5

2.1.2 Tissue-Level RV Biomechanics 9

2.1.3 Fiber-Level RV Biomechanics 11

2.2 Pulmonary Hypertension (PH) 12

2.2.1 Organ-Level RV Remodeling in PH 16

2.2.2 Tissue-Level RV Remodeling in PH 20

2.2.3 Fiber-Level RV Remodeling in PH 23

2.3 Effects of Potential Therapeutics on RV Biomechanics in PH 24

3.0 Analyzing the Effects of Angiotensin Receptor-Neprilysin Inhibition on Right Ventricular Biomechanics in Pulmonary Hypertension 26

3.1 Introduction 26

3.2 Methods 28

3.2.1 Pulmonary Artery Banding Procedures and Drug Administration 30

3.2.2 Hemodynamic Measurements 31

3.2.3 Histological Analysis 31

3.2.4 Biaxial Mechanical Testing 34

3.2.5 Constitutive Modelling 39

3.2.6 Statistical Analysis 41

3.3 Results 42

3.3.1 Hemodynamics and Remodeling 42

3.3.2 Fiber Angle 45

3.3.3 Biomechanics 47

3.4 Discussion and Conclusions 51

4.0 Effects of Healthy Aging on Right Ventricular Biomechanics 57

4.1 Introduction 57

4.2 Methods 58

4.3 Results 64

4.3.1 RV Hemodynamics and Morphology 64

4.3.2 RVFW Biomechanical Properties 64

4.3.3 Quantitative Transmural Histology 68

4.4 Discussion and Conclusions 71

5.0 Assessment of Stretch-Induced Transmural Myocardial Fiber Kinematics in Right Ventricular Pressure Overload 74

5.1 Introduction 74

5.2 Methods 80

5.2.1 HFU Imaging to Quantify Transmural RV Fiber Kinematics 80

5.2.1.1 Development of an HFU Imaging Framework 80

5.2.1.2 Algorithm Validation with Histological Measurements 83

5.2.1.3 Feasibility Evaluation of the Developed Framework to Study the Transmural Kinematics of RV Myofibers Under Uniaxial Loading 84

5.2.2 Finite Element Modeling to Study RV Fiber Kinematics Under Biaxial Loading 86

5.2.2.1 Model Development 86

5.2.2.2 Loading Scenarios, Boundary Conditions and Fiber Realignment .. 89

5.2.3 Statistical Analysis 97

5.3 Results..... 98

5.3.1 HFU Imaging 98

5.3.2 FE Modeling 101

5.4 Discussion and Conclusions 106

6.0 Conclusions and Future Directions 112

Appendix A Supplemental Tables 116

Bibliography 118

List of Tables

Table 1 World health organization (WHO) clinical categorization of PH 13

Table 2 Most commonly used experimental animal models of PH 15

Table 3 Effects of healthy aging on RV hypertrophy (RVFW thickness) and Fulton index 66

Table 4 Constitutive model parameters representing the longitudinal (b_1), circumferential (b_2) and in-plane coupling (b_3) stiffness of RV myocardium for the control and aging groups..... 66

Table 5 RV material properties and volume fractions used for FE modeling 88

Table 6 RV hemodynamics and remodeling parameters used for FE simulations..... 92

Table 7 Circumferential and longitudinal wall stresses applied to the representative volume element (RVE) for different loading scenarios..... 92

Appendix Table S1 p values obtained for pairwise comparison of different hemodynamic outcomes..... 116

Appendix Table S2 p values obtained for pairwise comparison of morphological measurements..... 116

Appendix Table S3 p values obtained for pairwise comparison of histological measurements 116

Appendix Table S4 p values obtained for pairwise comparison of biaxial mechanical properties and constitutive modeling results..... 117

Appendix Table S5 p values obtained for pairwise comparison of different loading scenarios at end-diastole (Fig. 33a) 117

Appendix Table S6 p values obtained for pairwise comparison of different loading scenarios at early-systole (Fig. 33b) 117

List of Figures

Figure 1 Anatomy of the heart chambers and pulmonary arteries, demonstrating the right and left ventricles, atriums, the pulmonary trunk, and the right and left pulmonary arteries. Arrows show the direction of blood flow out of the RV towards the pulmonary circulation. TV, PV, MV, AV indicate the tricuspid valve, pulmonary valve, mitral valve, and aortic valve, respectively..... 4

Figure 2 Multi-scale structure of the RV, demonstrating organ-level anatomy, tissue-level organization (red/pink: myofiber content, blue: collagen content), fiber-level architecture of collagen and myofibers, myofibrils and mitochondrial content, and sarcomere-level actin-myosin interactions. 6

Figure 3 Measurement of RV end-systolic and end-diastolic pressure-volume relationships via preload reduction. Arrows show RV end-systolic elastance (red), PA elastance (green) and the nonlinear fit to end-diastolic pressure-volume relationship (blue). .. 7

Figure 4 Summary of the framework developed to study the effects of Sac/Val on RV remodeling in PH. Sprague-Dawley rats were assigned to one of the Control, PH-placebo treated or PH-Sac/Val treated cohorts, followed by terminal invasive hemodynamic measurements, morphological measurements, quantitative histological analysis, biaxial mechanical characterization, and constitutive modeling. 29

Figure 5 Threshold-based segmentation of collagen (blue) and myofibers (red) from the histological scans. 32

Figure 6 Displacement-controlled biaxial mechanical testing of RVFW specimens. (a) Loading direction, ratios, and maximum displacements applied to specimens from

each cohort. (b) Representative temporal force measurements during a pre-conditioning cycle, demonstrating the stabilization of longitudinal and circumferential forces. 36

Figure 7 (a) Representative demonstration of interpolation of the RVFW stress response under equibiaxial strain-controlled loading (blue) using the scattered multi-protocol stress-strain measurements (red; 1:1, 1:2, 2:1, 1:4, 4:1, 1:6, and 6:1 loading ratios). The demonstrated interpolation shows the stress estimations for only one component of the biaxial RVFW stress response. Similar interpolations were reiterated for stress estimations in the other direction. E11 and E22 represent the biaxial Green-Lagrange strain measurements, while 2nd PK stress shows the 2nd Piola-Kirchhoff stress. (b) Approximation of the effective fiber ensemble stress-strain response (shown in red) from equibiaxial tissue-level measurements. (c) Differentiation of the fiber ensemble response for estimation of fiber-level stiffness and identification of collagen recruitment strain. 38

Figure 8 Hemodynamic measurements of the effects of PH and Sac/Val treatment on (a) RV maximum pressure, (b) Stroke volume, (c) Heart rate, (d) $dpdt$max, (e) $dpdt$min, (f) PA elastance (E_a), (g) RV elastance (E_{es}) and (h) Ratio of RV to PA elastance ($EesEa$). Sac/Val treatment significantly lowered RV maximum pressure (P_{max}), decreased the load-dependent measure of contractility ($dpdt$max), increased the load-dependent measure of relaxation ($dpdt$min) and decreased PA elastance (E_a) in addition to preventing RV-PA uncoupling. Horizontal line (—) and cross (×) representing median and mean of distributions, respectively. * indicates p<0.05 compared to Control, † indicates p<0.05 compared to PH. 43

Figure 9 Effects of PH and Sac/Val treatment on (a) RV hypertrophy (RVFW thickness) and (b) RV to LV mass ratio. Sac/Val resulted in significantly lower RV wall thickness, while not demonstrating significant effects on RV to LV mass ratio. Horizontal line (—) and cross (×) representing median and mean of distributions, respectively. * indicates p<0.05 compared to Control, † indicates p<0.05 compared to PH..... 44

Figure 10 (a) Representative transmural histological sections of RV myocardium from each cohort (Red/Pink: Myofiber, Blue: Collagen). Coordinates used to measure fiber orientations indicated on the top. (b) Effects of Sac/Val treatment on transmural myofiber orientations, and (c) Collagen fiber orientations, (d) Dominant myofiber orientation in each cohort, (e) Effects of Sac/Val on RV collagen area fraction, (f) Effects of Sac/Val on RV collagen fiber coherency. Error bars representing standard deviations. * indicates p<0.05 compared to Control, † indicates p<0.05 compared to PH. 46

Figure 11 Effects of Sac/Val treatment on (a) Biaxial mechanical properties of RVFW, (b) Fiber-level mechanical properties of combined collagen and myofiber bundles, (c) Intrinsic myofiber stiffness, (d) Collagen recruitment strain. Sac/Val treatment resulted in improved tissue-level biomechanical properties. At the fiber-level, Sac/Val prevented an increase in myofiber stiffness in PH, but did not affect collagen recruitment strains. Horizontal line (—) and cross (×) representing median and mean of distributions, respectively. Error bars in parts (a) and (b) representing standard deviations. * indicates p<0.05 compared to Control, † indicates p<0.05 compared to PH. 49

Figure 12 (a) Longitudinal, circumferential and coupled stiffness of RV myocardium revealed by constitutive modeling, (b) Cohort-specific strain energy maps of RV myocardium, indicating increased stiffness in PH and improved biomechanical performance with Sac/Val treatment. Sac/Val improved RV stiffness in both circumferential and longitudinal directions with no significant effects on in-plane coupling. Dashed lines indicate the strain energy levels for the control cohort at 3 $\mu Jmm3$. Horizontal line (—) and cross (×) representing median and mean of distributions, respectively. * indicates p<0.05 compared to Control, † indicates p<0.05 compared to PH..... 50

Figure 13 The framework used to study RV remodeling with healthy aging. In-vivo terminal invasive hemodynamic measurements were performed on young controls and aging Sprague-Dawley rats, followed by harvesting the heart and morphological measurements, biaxial mechanical testing, constitutive modeling, and quantitative transmural histological analysis. 59

Figure 14 Hemodynamic measures of the effects of healthy aging on RV (a) Heart rate, (b) Peak pressure, (c) End-diastolic pressure, (d) $dpdt$max (positive side) and $dpdt$min (negative side), (e) Contractility index and (f) Preload-independent measure of relaxation (tau). Healthy aging significantly increased RV peak pressures and the load-dependent measures of RV contractility ($dpdt$max and contractility index), while not affecting the heart rate, end-diastolic pressures and relaxation function ($dpdt$min and tau). Error bars represent standard error of the mean (SEM). * indicates p<0.05. BPM: Beats per minute; EDP: End-diastolic pressure; n.s: Non-significant..... 65

Figure 15 Effects of healthy aging on (a) Biaxial mechanical properties of RV myocardium, (b) Effective fiber-ensemble mechanical properties of combined myofiber-collagen bundles, (c) Effective myofiber stiffness, and (d) Effective collagen fiber stiffness. Healthy aging modulates the biomechanical properties of RVFW in a bimodal manner by increasing the effective myofiber stiffness while decreasing collagen fiber stiffness. Error bars represent standard error of the mean (SEM).* indicates $p<0.05$. EFE 2nd P-K Stress: Effective fiber-ensemble 2nd Piola-Kirchhoff stress. 67

Figure 16 Strain energy maps of RVFW in (a) the low-strain region (circumferential-longitudinal strain space) and (b) the high-strain region. Strain energy maps demonstrate increased RVFW stiffness in the low-strain region with healthy aging (mostly dominated by myofibers), followed by decreased RVFW stiffness in the high-strain region post-collagen recruitment. 68

Figure 17 Histological analysis of the effects of healthy aging on RV structure. (a) Representative transmural histological sections of the RVFW (Red/Pink: Myofiber, Blue: Collagen) and effects of aging on (b) Cardiomyocyte hypertrophy (myocyte width), (c) Transmural myofiber orientations, (d) Transmural collagen fiber orientations, and (e) Dominant myofiber orientations. Healthy aging results in cardiomyocyte hypertrophy, in addition to reorientation of sub-endocardial collagen and myofibers. Error bars represent standard error of the mean (SEM). * indicates $p<0.05$. 69

Figure 18 Histological analysis of the effects of healthy aging on (a) Transmural myofiber content (area fraction), (b) Transmural collagen content (area fraction), and (c) Transmural collagen fiber coherency. Healthy aging leads to loss of cardiomyocytes,

RVFW fibrosis and decreased collagen fiber coherency at endocardium. Error bars represent standard error of the mean (SEM). * indicates p<0.05. Epi: Epicardium; Mid: Mid-ventricular region; Endo: Endocardium. 70

Figure 19 Stretch-induced deformations experienced by RV myocardium during diastolic filling and the isovolumic contraction (IVC) phase of early-systole. During diastole, ventricular filling results in passive stretch of the RVFW. IVC follows tricuspid valve closure at end-diastole, during which active myocardial contraction increases chamber pressures (while both tricuspid and pulmonary valves remain closed) and results in increased wall stress (afterload) and stretching of the RVFW. Both active contraction and stretching happen simultaneously during this phase, as reflected in increased ventricular pressures, in addition to ventricular wall thinning, and fiber stretch during early-systole. This is followed by pulmonary valve opening and systolic ejection, which results in negative RVFW contractile strains. The current study focuses on stretch-induced deformations of RV myocardium during the end-diastolic and early-systolic phases of a cardiac cycle, without considering the effects of cardiomyocyte contraction. 76

**Figure 20 Conceptual demonstration of the effects of biaxial loading conditions on the deformation state and fiber kinematics of RV myocardium. Hypothetical loading scenarios resulting in (a) equibiaxial strain with no fiber rotations, as well as scenarios with kinematic shift of fibers towards the (b) circumferential and (c) longitudinal directions. Material nonlinearity and anisotropy of RV myocardium results in different fiber kinematics at different stress levels. While some scenarios may result in equibiaxial strain conditions with no fiber kinematics, others may lead to $\varepsilon Circ$.>

$\varepsilon Long.$ **or** $\varepsilon Circ. < \varepsilon Long.$**, resulting in clockwise or counterclockwise fiber kinematics, respectively. 79**

Figure 21 The ultrasound image processing framework used to detect transmural RV myofiber orientations. Basal anterior zone RVFW specimens were scanned while the ultrasound probe was aligned with the apex-to-base direction, normal to the transmural axis. High noise in the acquired high-frequency B-mode images were reduced via multi-scale decomposition using NLADF, followed by establishing myofiber connectivity by CEDF. Skeleton extraction was performed on the resulting image, followed by fiber detection using the Hough transform and fitting a normal probability density function (PDF) to the fiber distributions. 81

Figure 22 (a) The 3D-printed custom loading gripper used to evaluate RV myofiber kinematics under uniaxial loading. (b) Simultaneous uniaxial loading and HFU imaging of RVFW specimens. 85

Figure 23 The representative volume element (RVE) FE model used to study biaxial RV fiber kinematics, demonstrating the transmural stack of fibers from epi to endocardium and distribution of myofibers, collagen, and ECM at each transmural section. Transmural fiber architectures (measured via HFU) and porcine RVFW material properties/volume fractions were used to generate the RVE..... 88

Figure 24 Loading and boundary condition calculations. In order to keep the computational burden tractable, simulations were performed on a representative volume element (RVE; shown in black in dotted box), and effects of the 3D RV geometry were modeled as loading and boundary conditions based on an extension of the law of

Laplace for ellipsoidal geometries. Measurements were performed on porcine hearts to acquire the geometrical parameters required for modeling. 90

Figure 25 The RVE in the circumferential-longitudinal and longitudinal-transmural planes. Transmural fiber architectures (measured via HFU) and porcine RVFW material properties/volume fractions were used to generate the RVE. The calculated boundary conditions ($\sigma Circumferential$ and $\sigma Longitudinal$) were then applied in the circumferential-longitudinal plane to analyze biaxial RV fiber kinematics. Following simulations, fiber orientations of the RVE in the deformed state were categorized into circumferential ($\theta < 25$) and oblique ($25 \leq \theta \leq 90$) fibers. 91

Figure 26 Simulation of increased RV collagen content (fibrosis) using the developed FE model. (a) Parametric increase in RV collagen content. Red: Myofibers, Blue: Collagen. (b) Effects of parametric increases in RV collagen content on the biaxial mechanical properties of RV myocardium. Experimental data (shown in red) obtained from the literature (Nemavhola, 2017). Material properties of the structurally-informed FE model shown with black lines. 94

Figure 27 Rationale for the threshold used for categorizing circumferential and oblique fibers. (a) Fiber angle threshold used for categorizing circumferential fibers ($\theta < 25$). (b) Graphical demonstration of circumferential and oblique fibers in a circular plane. Deformed RV fiber orientations were grouped into circumferential ($\theta < 25$) and oblique ($25 \leq \theta \leq 90$) categories, following finite element simulations. The threshold for circumferential fibers was chosen in a way to include the initial HFU-measured fiber angles and at least 1 standard deviation of the fiber spread at each transmural section. Fibers outside of this threshold were labeled as "oblique". An increase in the

proportion of oblique fibers indicates fiber reorientation away from the circumferential direction, towards the longitudinal direction (±90°). Error bars demonstrate the fiber spread at each transmural section (pooled standard deviation of the distribution of fiber orientations measured via HFU imaging on n=3 specimens). 95

Figure 28 The remodeling algorithm used for multi-cycle simulations to study the adaptation of RV fibers towards the longitudinal direction in chronic pressure overload (CPO). Deformed fiber orientations were analyzed at the end of each cycle. If loading altered the fiber proportions in a statistically significant manner, fiber orientations were updated using the described criteria and simulations were proceeded to the next cycle. In case of no loading-induced alteration in the proportion of fibers, simulations were aborted. 96

Figure 29 Algorithm verification by comparing HFU measurements with histological staining (H&E). Error bars demonstrate fiber spread (standard deviation of the distribution of fiber orientations; measure of fiber dispersion) at each transmural section. Fiber angles are normalized to 0° at the epicardial layer, to better demonstrate the transmural change in fiber angles and facilitate comparison with previous studies. Dotted lines between HFU measurements are for visualization purposes only. 98

Figure 30 Representative transmural HFU images of RVFW fiber orientations, before and after loading under a stretch ratio of $\lambda = 1.35$. 99

Figure 31 Uniaxial myofiber kinematics under a stretch ratio of $\lambda = 1.35$. (a) Quantification of fiber angles using the developed framework. Uniaxial loading results in fiber

reorientation towards the loading direction (0°). Experimental measurements demonstrate good agreement with theoretical approximations of affine fiber kinematics for an incompressible transversely isotropic solid (R^2=0.92). (b) Effects of loading on RVFW helix slope. Loading results in decreased RVFW helix slope, which does not show any statistically significant differences with theoretical affine approximations. Error bars show standard error of the mean (SEM). * indicates p<0.01. US Probe: Ultrasound probe; Exp: Experimental. 100

Figure 32 (a) Quality of fit of the structurally-informed FE model to previously reported biaxial material properties of porcine RV myocardium. (b) FE model predictions vs. experimentally measured uniaxial RV fiber kinematics. Error bars demonstrate the fiber spread at each transmural section. Exp: Experimental. 102

Figure 33 Effects of different loading scenarios on biaxial fiber kinematics of RV myocardium. (a) Effects of loading on end-diastolic fiber kinematics, indicating increased proportion of oblique fibers only for the CPO scenario without concentric hypertrophy (single-cycle simulations). (b) Effects of loading on early-systolic fiber kinematics, demonstrating elevated proportions of oblique fibers under both CPO scenarios with amplified proportions for CPO without concentric hypertrophy (single-cycle simulations). *, †, ‡ and ¥ indicate p<0.01 compared to UNL (unloaded), Norm (normotensive), APO (acute pressure overload) and CPO (chronic pressure overload), respectively. UNL: Unloaded; Norm: Normotensive; APO: Acute pressure overload; CPO: Chronic pressure overload; CPO w/o Conc. Hyp.: Chronic pressure overload without concentric hypertrophy. 103

Figure 34 Multi-cycle simulations of RV fiber reorientation towards the longitudinal direction (±90°) under (a) CPO and (b) CPO without concentric RV hypertrophy. Error bars demonstrate fiber spread (standard deviation of the distribution of fiber orientations) at each transmural section. CPO: Chronic pressure overload; CPO w/o Conc. Hyp.: Chronic pressure overload without concentric hypertrophy. 104

Figure 35 Representative fiber orientation distributions for multi-cycle remodeling simulations under CPO, demonstrating a shift towards oblique fibers for both scenarios. Shaded area under the curves demonstrate the oblique fibers. Both CPO scenarios result in remodeling towards the longitudinal direction (±90°) with increased proportion of oblique fibers. CPO: Chronic pressure overload, CPO w/o Conc. Hyp.: Chronic pressure overload without concentric RV hypertrophy, PDF: Probability density function. 104

Figure 36 Proportion of oblique fibers for the normotensive scenario compared to CPO with and without concentric hypertrophy. Fiber proportions for the CPO cases are plotted following 4 cycles of remodeling simulations, while normotensive loading quits the remodeling algorithm following the first cycle of loading. Both CPO scenarios result in significant increases in the proportion of oblique fibers compared to normotensive loading at all transmural sections (epi to endocardium). Increased wall thickness (CPO vs. CPO w/o Conc. Hyp.) decreases the rate of longitudinal realignment, indicating a potential protective role for concentric hypertrophy against RV fiber reorientation in CPO. † and ¥ indicate $p<0.01$ compared to Normotensive and CPO (chronic pressure overload), respectively. CPO: Chronic pressure overload; CPO w/o Conc. Hyp.: Chronic pressure overload without concentric hypertrophy. 105

Figure 37 Effects of fibrosis on biaxial RV fiber kinematics under chronic pressure overload with concentric and eccentric hypertrophy, under (a) End-diastolic and (b) Early-systolic pressures. RV fibrosis did not demonstrate any statistically significant alteration in fiber proportions at end-diastole or early-systole. 106

1.0 Introduction

The motivation behind the studies conducted in this dissertation, as well as the specific research objectives, will be summarized in this section. Additionally, an overview of the organization of the dissertation will be provided.

1.1 Motivation

The right ventricle (RV) plays a key role in the human body by pumping deoxygenated blood through the pulmonary circulation for gas exchange, facilitating the distribution of oxygenated blood via the left ventricle (LV). However, pathologies such as pulmonary hypertension (PH) may affect RV structure/function, eventually leading to RV failure. PH is a disease resulting from restrictions in the pulmonary vasculature that, in turn, lead to increased RV pressures and RV remodeling. Pressure overload in PH results in biomechanical remodeling of the RV at different scales, from organ-level hemodynamics to cell-level contractility. The exact prevalence of PH is unknown, but there are around 400,000-700,000 PH-related hospitalizations annually in the United States (George et al., 2014).

Despite the development of multiple therapeutics for management of PH, lung transplantation remains the only curative treatment. Moreover, age-related differences exist in the survival rates of PH patients (Hoeper et al., 2013) and although the current evidence suggests an association between PH and aging, limited data exist on age-associated differences in RV biomechanical properties.

A major biomechanical remodeling event experienced by the pressure overloaded RV is the re-orientation of myofibers forming the RV tissue (Hill et al., 2014; Sharifi Kia et al., 2020), which results in altered RV biomechanical properties and function. However, RV wall thickness in human patients and large animal models complicates the study of fiber reorientation throughout the RV thickness, mainly due to the limited imaging depth of current modalities such as confocal or multi-photon microscopy (Sommer et al., 2015).

1.2 Objectives

In this work, we aimed to evaluate the effects of a novel dual-acting heart failure therapeutic (Sacubitril/Valsartan; also known as Sac/Val or LCZ696) on RV remodeling in PH. Additionally, we analyzed the effects of aging on RV structure and biomechanics. Moreover, an ultrasound image processing framework, coupled with computational models, was utilized to study the effects of different loading scenarios on the reorientation patterns of RV myofibers. The specific objectives of this work are:

1) Investigating the effects of Sac/Val treatment on the hemodynamics and biomechanical behavior of failing RV myocardium in an experimental model of PH
2) Analyzing the effects of healthy aging on RV structure and function
3) Assessment of passive transmural RV myofiber kinematics using a high-frequency ultrasound imaging framework and computational modeling

1.3 Organization of Dissertation

Chapter 2 provides an overview on RV structure, function, and biomechanics under normal physiological conditions and in the setting of pressure overload due to PH. Associated remodeling events in PH will be further discussed at different scales from organ-level hemodynamics, to tissue-level properties, and fiber-level architecture.

Chapter 3 will focus on analysis of the effects of Sac/Val treatment on RV remodeling in PH, using an experimental animal model. The reader is provided with an overview on the mechanism of action of Sac/Val, followed by detailed description of the techniques used to evaluate multi-scale RV remodeling in health, disease, and treatment. Our findings will then be discussed, and compared with the available literature, when possible.

Effects of healthy aging on RV structure, function, and biomechanics will be addressed in chapter 4. Current state of the literature on aging-associated RV remodeling will be reviewed, accompanied by description of our measurement techniques and discussion of our findings.

Our efforts towards the development of an ultrasound imaging framework (coupled with computational models) for evaluation of RV fiber reorientation under loading will be discussed in chapter 5. Imaging techniques and computational modeling details will be discussed, in addition to evaluation of the potential of the developed framework for characterization of RV fiber orientations. This will be followed by an exploratory assessment of the effects of different remodeling events on RV fiber reorientation in pressure overloaded porcine myocardium.

2.0 Background

2.1 The Right Ventricle (RV)

As the most anterior of the heart's four chambers, the right ventricle (RV) is responsible for blood supply to the pulmonary circulation (Fig. 1). Deoxygenated blood enters the RV through the right atrium (RA) during diastolic filling and gets pumped to the pulmonary circulation, for gas exchange and oxygenation, via RV contraction in systole. Oxygenated blood then enters the left side of the heart to supply the systemic circulation and distribution to different organs.

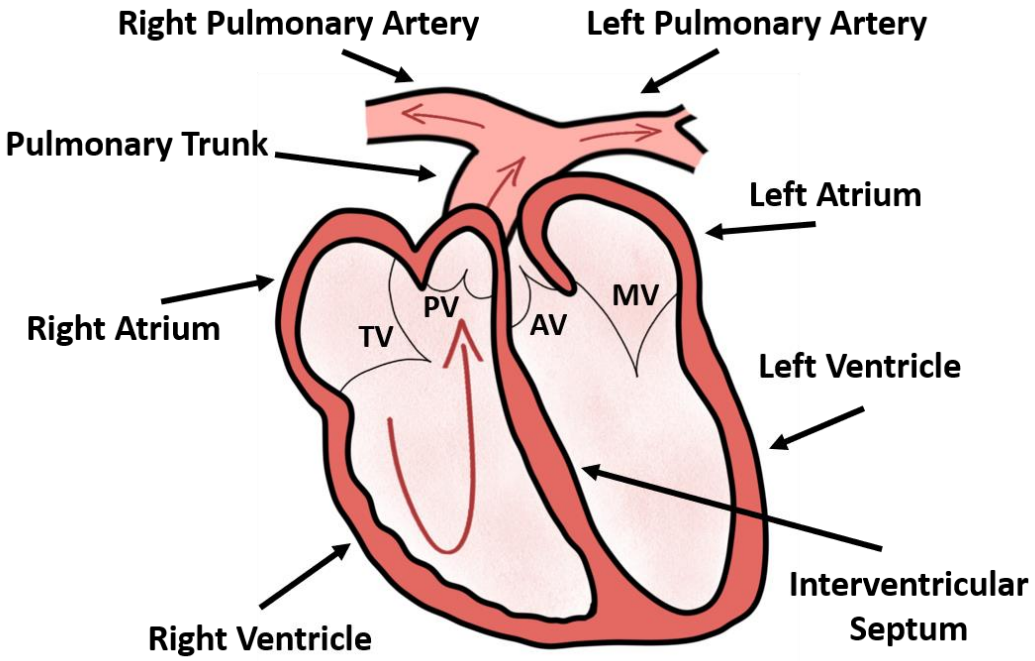

Figure 1 Anatomy of the heart chambers and pulmonary arteries, demonstrating the right and left ventricles, atriums, the pulmonary trunk, and the right and left pulmonary arteries. Arrows show the direction of blood flow out of the RV towards the pulmonary circulation. TV, PV, MV, AV indicate the tricuspid valve, pulmonary valve, mitral valve, and aortic valve, respectively.

The RV is wrapped around the anteroseptal side of the left ventricle (LV), while the interventricular septum separates the RV and LV cavities in the heart (Fig. 1). Due to the multi-scale structure of the RV, with specific features and function at different levels (Fig. 2), different measurement techniques and metrics are used to evaluate RV function across different scales. The following sections discuss RV biomechanics and function at the organ, tissue, and fiber level:

2.1.1 Organ-Level RV Biomechanics

At the organ level, RV biomechanics and function are often characterized by synchronous measurement of RV pressure and volume waveforms over a cardiac cycle, resulting in RV pressure-volume (P-V) loops. Additionally, multiple imaging modalities, including 2D and 3D echocardiography and cardiac magnetic resonance imaging (cMRI), are employed for measurement of RV structure. P-V loop analysis helps evaluating RV peak, end-systolic, and end-diastolic pressures, in addition to the heart rate, end-systolic and end-diastolic volumes, stroke volume (difference between systolic and diastolic volumes), and ejection fraction (ratio of stroke volume to end-diastolic volume). Moreover, analyzing the rate of change in pressure waveforms enables assessment of RV contractility and relaxation, respectively measured by the maximum and minimum time derivative of pressure ($\frac{dp}{dt}_{\max}$ and $\frac{dp}{dt}_{\min}$).

The dynamic supply-demand biomechanics of the RV and the pulmonary artery (PA) is another determinant of organ-level RV function. A commonly used metric for evaluation of RV-PA coupling efficiency is the ratio of the load-independent measure of RV contractility, end-systolic elastance (E_{es}), to PA elastance (E_a). In animal models of PH, E_{es} is characterized by preload reduction of the RV, via vena caval occlusion, which exposes the RV to a wide range of

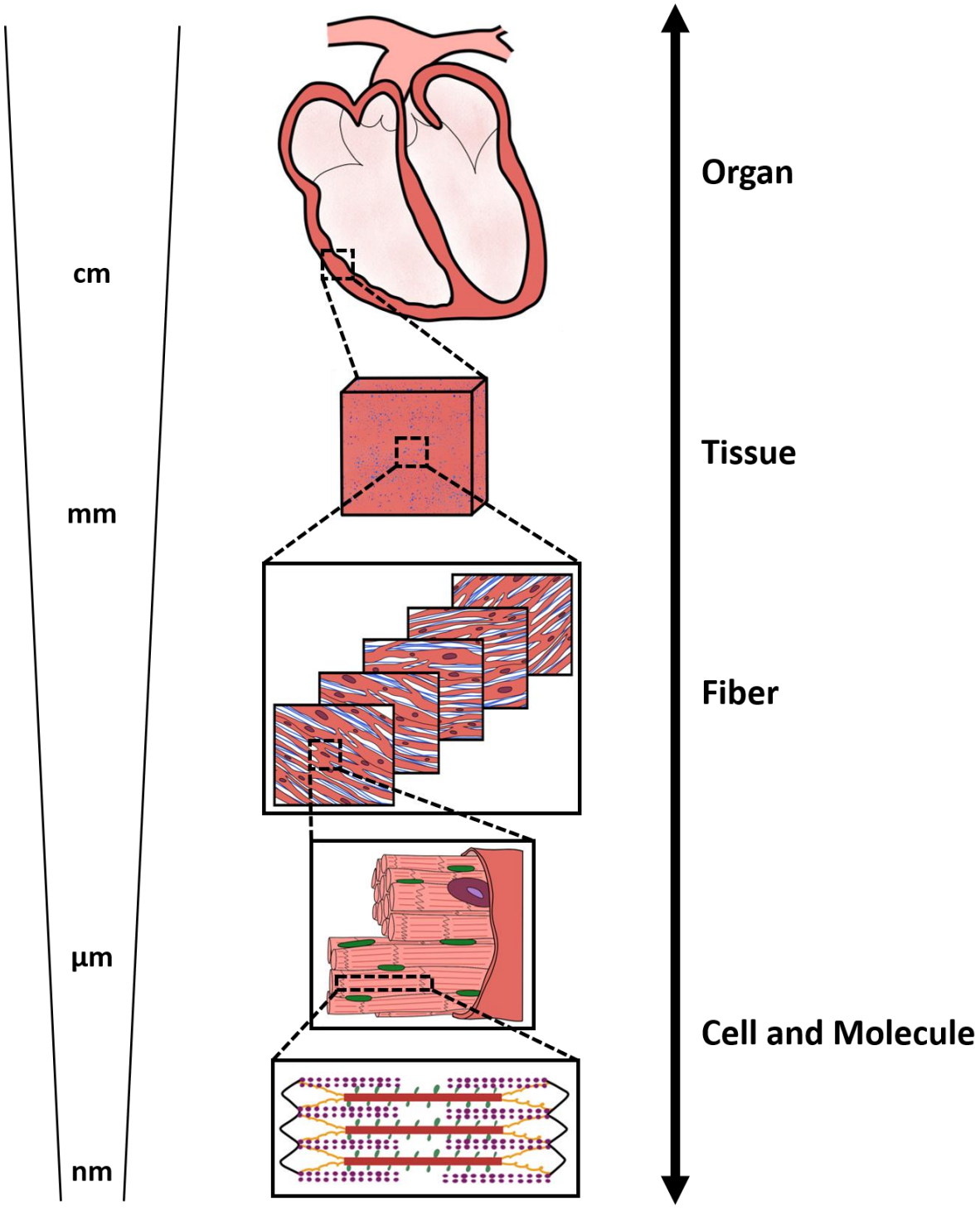

Figure 2 Multi-scale structure of the RV, demonstrating organ-level anatomy, tissue-level organization (red/pink: myofiber content, blue: collagen content), fiber-level architecture of collagen and myofibers, myofibrils and mitochondrial content, and sarcomere-level actin-myosin interactions.

operational pressures (Fig. 3) and forms multiple P-V loops. E_{es} is then calculated as the slope of a linear fit to the end-systolic pressure-volume relationship (ESPVR) (Hill et al., 2014; Sharifi Kia et al., 2020).

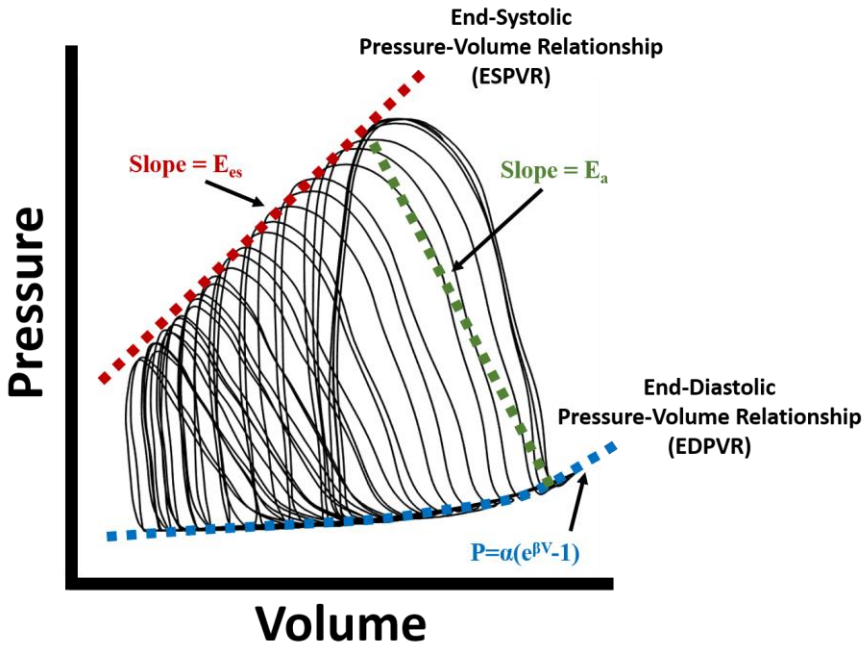

Figure 3 Measurement of RV end-systolic and end-diastolic pressure-volume relationships via preload reduction. Arrows show RV end-systolic elastance (red), PA elastance (green) and the nonlinear fit to end-diastolic pressure-volume relationship (blue).

This is, however, not feasible in a clinical setting, due to difficulties with simultaneous pressure and volume measurements and RV preload reduction in human subjects. However, it is possible to characterize RV function and systolic/diastolic elastance using single-beat P-V data from right heart catherization. Different methods have been proposed for estimation of E_{es} in the clinic, extrapolating RV-PA coupling efficiency from a single P-V loop (Vanderpool et al., 2020). E_a, on the other hand, is characterized similarly in the clinic and in animal models (Fig. 3), using the ratio of RV end-systolic pressure to stroke volume (Hill et al., 2014; Vanderpool et al., 2015).

Organ-level RV diastolic stiffness is characterized by the end-diastolic elastance (E_{ed}) and the end-diastolic pressure-volume relationship (EDPVR), also obtained by measurement of RV P-V patterns at different loads via preload reduction (Fig. 3). Due to the nonlinear nature of passive RV mechanical properties, an exponential function is then fitted to the diastolic portion of the generated P-V loops, to characterize organ-level diastolic stiffness (Fig. 3). Here, β represents the diastolic stiffness, α is a scaling factor and P and V are respectively, pressure and volume data from the diastolic portion of P-V loops. Due to feasibility issues with preload reduction in human patients, single-beat analysis methods have been proposed for regression of the exponential equation in Figure 3, using only three points: the origin, beginning diastolic point, and the end-diastolic point (Vanderpool et al., 2015). However, quality of fit and uniqueness of optimized parameters (due to a potential local minima) remain a major concern when characterizing an exponential function with limited number of points. Alternatively, other metrics such as the instantaneous diastolic elastance (E_{ed}) may be used for biomechanical analysis of RV diastolic function, by evaluating the slope of the line tangent to the end-diastolic point of RV P-V loops (Gaynor et al., 2005; Jang et al., 2017).

Organ-level LV wall stress is often calculated by approximating the ventricular geometry by a sphere (or cylinder, depending on the remodeling stage), followed by stress calculations using the law of Laplace. However, the complex geometry of the RV complicates simple theoretical approximations of wall stress. While some studies have used the classic Laplace formulation for a sphere to approximate RV wall stress (Jang et al., 2017), others have developed an extension of the law of Laplace, considering the ellipsoidal geometry of the RV (Avazmohammadi et al., 2017b).

2.1.2 Tissue-Level RV Biomechanics

At the tissue level, biaxial mechanical testing remains the gold standard for evaluation of RV free wall (RVFW) biomechanical properties. Specimen orientation plays a key role in the observed tissue-level biaxial response. Therefore, biaxial testing is often performed on square specimens harvested from the RVFW with one side aligned with the apex to outflow-tract/base direction (longitudinal direction), while the other side is aligned with the circumferential direction (Valdez-Jasso et al., 2012; Hill et al., 2014). Biaxial displacement or force-controlled loadings are then applied to the specimen, followed by post-processing of stress-strain measurements using a large deformation analysis framework. RVFW specimens are often submerged in modified Krebs solution with 2,3-butanedione monoxime (BDM) and oxygen (Valdez-Jasso et al., 2012; Hill et al., 2014; Sharifi Kia et al., 2020) to facilitate testing viable myocardial tissues. While ex-vivo biaxial testing has been previously employed for characterization of active biomechanical properties of LV myocardium (Lin and Yin, 1998), biaxial studies on the RV have been mostly focused on passive components of RVFW biomechanics. Most biaxial studies have used visual tracking markers on the RVFW for surface strain measurements; however, more recent work (Park et al., 2016) has employed 3D ultrasound speckle tracking techniques to quantify the 3D strain state of the RVFW under loading. 3D strain measurements also enable inverse calculation of transmural RV fiber orientations (Park et al., 2016).

RVFW specimens from small animal models, large animal models, and human donors have demonstrated a nonlinear anisotropic biaxial response (Sacks and Chuong, 1993; Valdez-Jasso et al., 2012; Sommer et al., 2015). RVFW was shown to be stiffer and more anisotropic than the LV (Sacks and Chuong, 1993). The nonlinearity of the RVFW stress-strain response has been attributed to gradual collagen recruitment, in addition to stiffening of myofibers (Avazmohammadi

et al., 2017a), while RVFW fiber architecture accounts for tissue anisotropy. Diastolic filling was found to operate under stresses that result in RVFW strains bellow ≈5% (Jang et al., 2017), indicating the initial portion of the biaxial stress-strain curves (dominated by myofibers) as the operational range of RV stress/strain under physiological diastolic loading.

The acquired biaxial response could be further analyzed via constitutive modeling, which provides additional information on the tissue-level mechanics of the RVFW and facilitates in-silico implementation of RV biomechanical properties. Different models have been employed to study the passive biomechanics of RVFW. Due to relatively low computational cost, phenomenological constitutive models have been used to analyze the alterations in tissue-level biomechanical properties and RVFW anisotropy, without considering the effects of fiber-level organization of RV collagen and myofibers (Hill et al., 2014; Javani et al., 2016). Others have used more sophisticated and structurally-detailed constitutive models, accounting for transmural RV fiber architectures and interactions between collagen and myofibers (Avazmohammadi et al., 2017a).

Quantitative histological analysis of collagen and myofiber area fractions is often used to measure RVFW content. The RVFW extracellular matrix (ECM) mainly consists of fibrillar collagen networks (type I and III), basement membrane type IV collagen, elastin, proteoglycans, fibronectin, and laminin (Stroud et al., 2002). Healthy RVFW consists of 4-9% collagen (by area), depending on the tissue source and animal model (Javani et al., 2016; Akazawa et al., 2020; Sharifi Kia et al., 2020). However, despite relatively low area/volume fractions, the ECM plays a key role in passive RV biomechanics. Biaxial testing of decellularized RVFW specimens revealed that the ECM contributes to 23-26% of biaxial RV stiffness under ≈10% strain (Vélez-Rendón et al., 2019). Mechanical contribution of the ECM grows with increased collagen recruitment, contributing to ≈71-78% of biaxial RV stiffness at 30% strain (Avazmohammadi et al., 2017a).

2.1.3 Fiber-Level RV Biomechanics

In addition to direct measurements at the fiber level, passive mechanical properties of RV collagen and myofibers can also be estimated from biaxial tissue-level measurements (Fata et al., 2014; Hill et al., 2014; Sharifi Kia et al., 2020). Since experimental measurements may fail to apply truly equibiaxial loads on the RVFW specimens, the strain-controlled equibiaxial response of specimens are first interpolated from the acquired biaxial measurements over a wide range of loading scenarios (Fata et al., 2014). As equibiaxial loading of soft tissues leads to a unique loading state with no fiber rotations (Sacks, 2003), the effective fiber-ensemble (EFE) stress-strain response can then be obtained by addition of the tissue-level biaxial response in the longitudinal and circumferential directions (EFE stress = longitudinal stress + circumferential stress). The EFE response represents the combined mechanical response of myofiber and collagen bundles, independent of fiber orientations. The RV demonstrates a nonlinear EFE stress-strain response (Hill et al., 2014; Avazmohammadi et al., 2017a). The initial portion of the EFE stress-strain curve (before collagen recruitment) is governed by myofibers, while collagen fiber response dominates the linear region of the curve, following collagen recruitment (Hill et al., 2014; Avazmohammadi et al., 2017a; Sharifi Kia et al., 2020).

Gradient-based image analysis techniques have been employed to analyze RV collagen and myofiber orientations from histological sections (Hill et al., 2014; Avazmohammadi et al., 2017a). RV fibers demonstrate counterclockwise rotations throughout the RVFW (Hill et al., 2014; Avazmohammadi et al., 2017a), which lead to unique biomechanical and functional properties. RV transmural myocardial fiber orientation range was found to decrease with body size, ranging from 110-120 degrees in small animal models (Nielsen et al., 2009; Avazmohammadi et al., 2017b) to 30-40 degrees in larger animals (Sacks and Chuong, 1993). An abrupt change in

epicardial fiber angles was noted in RVFW tissues obtained from large animals (Vetter et al., 2005; Agger et al., 2016), indicating a layer of entirely longitudinal myofibers. However, this was absent in smaller animals (Hill et al., 2014; Sharifi Kia et al., 2020).

Diffusion tensor MRI (DT-MRI) can be utilized to assess the 3D helical architecture of RV myofibers (Nielsen et al., 2009; Agger et al., 2016; Omann et al., 2019). Second-harmonic generation (SHG) microscopy is another technique that can be used to visualize the 3D architecture of collagen and myofibers in ventricular tissues (Sommer et al., 2015). While SHG microscopy provides high fidelity information on the microarchitecture of ventricular fibers, this technique has an imaging depth of <1.2mm (Sommer et al., 2015). This limits SHG's potential to study the full-thickness transmural fiber orientations of intact RV myocardium from large animal models and human donors, which are generally >2 mm in thickness (Javani et al., 2016; Nemavhola, 2017).

2.2 Pulmonary Hypertension (PH)

Clinically, pulmonary hypertension (PH) is defined as a condition with resting mean PA pressures ≥ 25 mmHg (Thiwanka Wijeratne et al., 2018). PH results in RV pressure overload and leads to multi-scale adaptations in RV structure/function to tackle the increased afterload. Although PH initiate from pulmonary vascular remodeling, progression to RV dysfunction and failure remains the main cause of mortality in PH patients (Voelke et al., 2011). The world health organization (WHO) classifies PH into 5 different groups (Table 1).

Table 1 World health organization (WHO) clinical categorization of PH

WHO Group	Underlying Mechanism
Group I	PH due to pulmonary arterial hypertension (PAH); Pre-capillary PH
Group II	PH due to left heart disease (PH-LHD)
Group III	PH due to underlying lung disease/hypoxia
Group IV	Chronic thromboembolic PH
Group V	PH with multifactorial underlying cause/unclear mechanism

Different studies have investigated the biomechanics of RV remodeling at different scales from organ-level structure/function and hemodynamics to tissue-level biomechanical properties, fiber architecture, and cellular contractility and function. Recent work has provided important insights into the time-course of multi-scale remodeling events in PH and has analyzed the potential of different therapeutic interventions to attenuate RV remodeling (Borgdorff et al., 2013; Andersen et al., 2014; Avazmohammadi et al., 2019a; Clements et al., 2019; Sharifi Kia et al., 2020). Analyzing the relative contribution of different remodeling events to RV dysfunction has facilitated identification of adaptive vs. maladaptive responses to pressure overload (Gomez et al., 2017; Avazmohammadi et al., 2019a).

Clinical work has been focused on studying RV mechanics using invasive hemodynamics, cMRI, and echocardiography. On the other hand, pre-clinical studies have employed animal models of PH for mechanistic investigation of the biomechanical remodeling events in PH and the role of mechanical stimuli in these processes (Table 2). Most commonly used animal models of PH include: 1) PH induced via VEGF receptor blocker Sugen-5416 followed by exposure to hypoxia (SuHx), 2) Monocrotaline (MCT)-induced PH and 3) PH induced via pulmonary artery banding (PAB) (Akazawa et al., 2020). The SuHX model results in similar angio-obliterative

lesions to those developed in PH patients, making this an ideal model to study pulmonary vascular mechanobiology in PH. The MCT model has been widely used due to reproducibility and simplicity; however, development of myocarditis (Akhavein et al., 2007) remains a major limitation of this model. The PAB model helps analyzing the effects of PH on RV remodeling, in the absence of confounding effects from pulmonary vascular remodeling or hypoxia (Bogaard et al., 2009; Borgdorff et al., 2013; Andersen et al., 2014; Hill et al., 2014; Sharifi Kia et al., 2020). A mild constriction via PAB results in adaptive RV remodeling with minor indications of RV fibrosis (Bogaard et al., 2009). However, recent studies have indicated that a sufficiently severe constriction induced by PAB can result in similar levels of elevation in RV pressures, dilation, hypertrophy, and fibrosis, compared to SuHx or MCT models (Andersen et al., 2014; Akazawa et al., 2020). Severe PAB may progress to RV-PA uncoupling and maladaptive RV failure (Andersen et al., 2014; Akazawa et al., 2020). This makes the PAB model ideal to study the isolated RV remodeling benefits of therapeutic interventions, in the absence of alterations in pulmonary vascular resistance (PVR) or VEGF inhibition (Borgdorff et al., 2013; Andersen et al., 2014).

In the following sections, we discuss the current understanding of multi-scale biomechanics of the RV in PH, highlighting the findings from in-vivo, ex-vivo, and in-vitro studies. Recent progress on the mechanisms of RV remodeling will be explored from a biomechanical perspective, in addition to a discussion on the effects of potential therapeutics on RV biomechanics in PH.

Table 2 Most commonly used experimental animal models of PH

Animal Model	Features
Sugen-Hypoxia (SuHx)	• Results in similar angio-obliterative lesions to those developed in PH patients • Ideal to study pulmonary vascular mechanobiology in PH • Significant RVFW fibrosis
Monocrotaline (MCT)	• Simple and reproducible procedure • May lead to development of myocarditis • May not result in significant RV wall thickening
Pulmonary Artery Banding (PAB)	• Results in isolated RV pressure overload • Helps analyzing the effects of PH on RV remodeling, in the absence of confounding conditions such as pulmonary vascular remodeling or hypoxia • Mild constriction via PAB results in adaptive RV remodeling with minor indications of RV fibrosis • Sufficiently severe constriction induced by PAB results in similar levels of elevation in RV pressures, dilation, hypertrophy, and fibrosis, compared to SuHx or MCT models. Severe PAB may progress to RV-PA uncoupling and maladaptive RV failure • Ideal for studying the isolated RV remodeling benefits of therapeutic interventions, in the absence of alterations in pulmonary vascular resistance (PVR) or VEGF inhibition

2.2.1 Organ-Level RV Remodeling in PH

PH results in altered organ-level RV hemodynamics. Several studies have investigated the effects of pressure overload on RV hemodynamics using invasive and noninvasive measures of RV structure and function. RV function is the most critical determinant of survival in PH (Bogaard et al., 2009). Recent work indicates that RV dysfunction in PH initiates at the organ-level, before progressing to tissue and cellular remodeling (Wang et al., 2018). In a SuHx model of PH, Wang et al. demonstrated preserved ejection fraction and RV-PA coupling with increased contractility (measured via $\frac{dp}{dt}_{\max}$ and RV end-systolic elastance E_{es}) following 14 days of hypoxia (Wang et al., 2013, 2018). RV hypertrophy reached a plateau at 14 days, while reduced ejection fraction and end-systolic elastance was observed at later time points (56 days of hypoxia), leading to RV-PA uncoupling and RV dysfunction (Wang et al., 2013, 2018). However, myofilament contractile forces were elevated similarly at all different stages of PH, with preserved Frank-Starling mechanism, suggesting RV dysfunction only at the organ-level.

PH results in increased RV systolic and diastolic pressures (Bogaard et al., 2009; Wang et al., 2013; Hill et al., 2014; Akazawa et al., 2020; Sharifi Kia et al., 2020), as well as elevated total PVR (Wang et al., 2013) and reduced cardiac output (Andersen et al., 2014). From a structural perspective, pressure overload in PH results in increased RV wall thickness and dilation at the organ level, commonly referred to as concentric and eccentric hypertrophy, respectively (Andersen et al., 2014; Hill et al., 2014; Avazmohammadi et al., 2019a). Increased wall thickness in the early stages of PH helps reducing RV wall stress and increases contractility; however, progression of PH and chamber dilation at later stages results in depressed organ-level contractility and RV dysfunction (Fan et al., 1997; Avazmohammadi et al., 2019a). In a rat PAB model of PH, Cheng

et al. observed increased RV contractility, via RV hypertrophy (increased wall thickness), in response to increased RV systolic pressures, reduced ejection fraction and decreased cardiac output; however, this was insufficient to maintain RV-PA coupling (Cheng et al., 2018).

Under normal hemodynamics, RV wall stress was found to be higher in the circumferential direction compared to the longitudinal (apex to base/outflow-tract) direction (Avazmohammadi et al., 2017b). PH results in overall increased organ-level RV wall stress with a more significant elevation in the longitudinal direction (40% and 150% increase in the circumferential and longitudinal directions, respectively (Avazmohammadi et al., 2017b)). Higher organ-level stress elevations in the longitudinal direction may explain the observed patterns of remodeling at the tissue and fiber level in PH (longitudinal stiffening and fiber reorientation). Wall stress analysis using combined pressure catheterization and cMRI in PH patients (Richter et al., 2020) demonstrated a positive correlation between RV end-systolic wall stress and both diastolic elastance (E_{ed}) and RV afterload measured by PA elastance (E_a). Since the original Laplace formulation was proposed for thin-walled structures and RV hypertrophy and increased wall thickness in PH may violate those assumptions, recent studies have employed a modified formulation of the law of Laplace to calculate RV wall stress in PH (Attard et al., 2019). In a clinical study, Attard et al. demonstrated that RV wall stress could be an independent predictor of all-cause mortality in PH patients (Attard et al., 2019).

RV-PA coupling efficiency is a major determinant of outcomes in PH (Tabima et al., 2017; Richter et al., 2020). Increased afterload in PH is followed by an initial increase in organ-level RV contractility to compensate for the increased demand, before RV dilation, increased wall stress and progression to reduced contractility, RV-PA uncoupling, and maladaptive RV failure (Tabima et al., 2017; Attard et al., 2019). Tello et al. employed cMRI and right heart catherization to study

the RV-PA coupling reserve in PH patients (Tello et al., 2019). Reduction in RV-PA coupling (measured via single-beat analysis, as discussed in pages 7-8) was associated with increased end-diastolic volume index, PA stiffening, and reduced ejection fraction. Normal RV-PA coupling efficiency ranges from 1.5-2, while PH patients with early signs of maladaptive remodeling demonstrated coupling efficiencies ranging from 0.89-1.09 (Tello et al., 2019). Patients with severe progressive RV maladaptation showed coupling efficiencies around 0.56-0.61. A cutoff of 0.805 was defined for the onset of RV dilation and failure (ejection fraction<35%), demonstrating a significant reserve for RV-PA coupling before progression to RV failure (Tello et al., 2019). Another clinical study demonstrated that RV-PA coupling is negatively correlated with mean PA pressures and is an independent predictor of survival in PH at different stages (Vanderpool et al., 2015).

In addition to RV contractility and systolic function, PH also affect RV diastolic function. Single-beat analysis of P-V loops in PH patients revealed a significant increase in diastolic stiffness (β), which was correlated with metrics of disease severity such as RV stroke volume, 6-minute walking distance and RA pressures (Rain et al., 2013). A significant increase in RV end-diastolic elastance (E_{ed}) was observed in response to increased systolic and diastolic pressures via PAB, in a rat model of PH (Jang et al., 2017). Moreover, E_{ed} was found to be positively correlated with β (Jang et al., 2017). In a large animal PAB model of chronic PH, Gaynor et al. observed a significant increase in RV pressures and load-dependent measure of RV contractility ($\frac{dp}{dt}_{\max}$), accompanied by increased RV elastance (Gaynor et al., 2005). While no differences in cardiac output were observed in response to PAB (indicating adaptive RV remodeling, potentially due to severity of the PAB procedure), there was a ≈2-fold increase in diastolic stiffness, which the authors attributed to impaired diastolic function (Gaynor et al., 2005). It is worth noting that organ-

level diastolic stiffness derived from RV hemodynamic measures is load-dependent and does not compare to tissue-level stiffness measures based on stress-strain mechanical testing data. The EDPVR has a nonlinear form and, therefore, organ-level RV diastolic stiffness may increase in response to increased filling pressures, independent of RV remodeling (Levine, 1972). Consequently, an increase in organ-level diastolic stiffness does not necessarily exhibit structural RV remodeling. A structurally normal RV may demonstrate increased organ-level diastolic stiffness in response to sufficiently elevated filling pressures (Levine, 1972). Multi-scale studies at the tissue and fiber level facilitate evaluation of intrinsic load-independent RVFW biomechanical properties (Hill et al., 2014; Sharifi Kia et al., 2020).

PH primarily affects RV structure and function; however, RV and LV function are interdependent on one other and LV contraction assists with 20-40% of the systolic RV pressure rise (Santamore and Dell'Italia, 1998). Alterations in RV structure/function such as RV dilation, fiber reorientation and impaired contractile function directly affect the organ-level biomechanics of the LV by reducing LV torsion and resulting in delayed peak torsion (Kaiser et al., 2020; Kheyfets et al., 2020). Isolated RV pressure overload in a PAB model resulted in reduced LV ejection fraction and stroke work, as well as LV atrophy (reduced wall thickness) (Kheyfets et al., 2020). PH induced in rats via MCT resulted in decreased LV and systemic pressures, reduced LV $\frac{dp}{dt}_{\max}$, and increased LV $\frac{dp}{dt}_{\min}$, measured in-vivo (Han et al., 2018). However, ex vivo testing of isolated LVs with Langendorff perfusion demonstrated the LV being capable of developing normal pressures at different afterloads (Han et al., 2018). These findings suggest that altered LV function in PH is predominantly a result of the biomechanical interactions between the ventricles, rather than intrinsic LV remodeling.

While PH is more prevalent among females than males (Badesch et al., 2010), sex differences exist in the survival rates of PH patients, with females demonstrating better outcomes (Jacobs et al., 2014; Lahm et al., 2014; Shen et al., 2020). The protective effects of the female sex hormone 17β-estradiol (Estrogen; also known as E_2) has been investigated in animal models of PH (Liu et al., 2014, 2017b; Lahm et al., 2016). In response to similar levels of pressure overload induced via SuHx, female rats demonstrated better cardiac index, stroke volume and RV compliance. These effects were not present in ovariectomized female rats, while exogenous E_2 repletion lead to improved cardiac index and ejection fraction (Liu et al., 2014), and prevented RV-PA uncoupling (Liu et al., 2017b). Moreover, E_2 has been shown to prevent reduced PA compliance in PH (Liu et al., 2014) and result in decreased PA systolic pressures (Liu et al., 2017a). Multi-scale studies suggest a direct effect from estrogen on RV remodeling via increasing RV contractility, in addition to indirect benefits from reduced PVR, reduced PA systolic pressures, and prevention of PA stiffening, resulting in reduced RV afterload (Liu et al., 2014). Prospective analysis of RV function in PAH patients demonstrated better systolic adaptation (measured via E_{es}) and RV-PA coupling efficiency in female patients (Tello et al., 2020), potentially contributing to the sex differences in survival rates of PH patients. Despite similar levels of RV afterload (measured by E_a), median RV-PA coupling efficiency was higher than the 0.805 threshold (Tello et al., 2019) in female patients, but not in males (Tello et al., 2020).

2.2.2 Tissue-Level RV Remodeling in PH

PH results in increased biaxial RVFW stiffness, with ≈2-fold increase in tissue anisotropy (Hill et al., 2014; Park et al., 2016; Avazmohammadi et al., 2017b). RV pressure overload in PH leads to higher tissue-level stiffening in the longitudinal vs. circumferential direction, due to RV

fiber reorientation, in addition to alterations in intrinsic mechanical properties (Hill et al., 2014; Park et al., 2016; Avazmohammadi et al., 2017b; Sharifi Kia et al., 2020). Increased RVFW stiffness in the longitudinal direction was found to be correlated with increased organ-level diastolic elastance (E_{ed}) in a PAB model of PH (Jang et al., 2017). Moreover, contribution of RV collagen-myofiber interactions to tissue-level biomechanics was found to significantly increase in response to pressure overload (Avazmohammadi et al., 2017b).

In addition to elastic stiffness, PH also affects the dynamic viscoelastic properties of RV myocardium. In a large animal PAB model of PH, RVFW elastic stiffness and viscous damping constants were elevated in response to pressure overload (Stroud et al., 2002). Ex-vivo treatment of RVFW with plasmin resulted in increased MMP-2 and MMP-9 activity, collagen degradation, and reduced elastic and viscous damping constants, compared to baseline measurements (Stroud et al., 2002).

Alterations in RVFW contractile strains manifest early in the progression of PH (Voeller et al., 2011). In-vivo tissue-level contractile deformations of RV myocardium can be characterized by placement of radiopaque markers on the RVFW combined with biplane fluoroscopy (Chuong et al., 1991). Marker displacements can then be post-processed to measure RVFW fractional area reduction (measure of tissue-level contractility), as well as maximal (principal) RVFW shortening in the fiber and cross-fiber directions. In an in-vivo study on canine myocardium, Chuong et al. demonstrated that the outflow region of the RVFW undergoes higher fractional area reductions compared to the inflow and mid-ventricular regions (Chuong et al., 1991). Acute PA occlusion resulted in a significant increase in RV peak pressures and organ-level contractility, but lead to decreased tissue-level fractional area reduction at the outflow region (Chuong et al., 1991). The observed effects were attributed to differences in the embryological origin of the outflow region,

compared to the inflow and mid-ventricular regions (March et al., 1962; Chuong et al., 1991). Echocardiography is another technique for in-vivo RVFW tissue evaluation, routinely used for clinical diagnosis of RV function. 2D ventricular torsion and RVFW strain measurements have been employed for clinical assessment of regional and global RV function (Bossone et al., 2013). PH was shown to result in reduced longitudinal RVFW peak systolic strains and strain rate, exhibiting associations with 1,2,3, and 4-year mortality in PAH patients (Sachdev et al., 2011). PH patients with RVFW longitudinal peak systolic strains <19% demonstrate lower survival rates than those with longitudinal strains >19% (Haeck et al., 2012). Reduced longitudinal systolic strains were also noted in experimental PAB, SuHx, and MCT models of PH (Akazawa et al., 2020). Despite cost-effectiveness and wide availability of echocardiography, RV anatomy and positioning within the chest leads to reproducibility issues with ultrasound-based strain assessments (Bossone et al., 2013). Additionally, unlike the LV, circumferential and radial ultrasound-based strains are challenging to measure for the RVFW (Tadic et al., 2018). cMRI is a more accurate technique for in-vivo RVFW strain measurements. In a large animal PAB model of early-stage PH, Voeller et al. combined cMRI and inverse finite element (FE) models to study the effects of PH on RVFW systolic strains (Voeller et al., 2011). Severe pressure overload (250% increase in RV pressures) was found to result in decreased RVFW minimum principal strains (measure of segmental shortening) at the basal level, indicating reduced tissue-level contractility (Voeller et al., 2011). Moderate pressure overload (34% increase in RV pressures), however, did not demonstrate any significant effects on RVFW strains (Voeller et al., 2011).

PH results in disrupted matrix turnover (Golob et al., 2016), altered matrix metalloproteinase (MMP) activity, and increased RVFW collagen content (Bogaard et al., 2009; Borgdorff et al., 2013; Rain et al., 2013; Andersen et al., 2014; Akazawa et al., 2020; Sharifi Kia

et al., 2020), potentially due to capillary rarefaction (Borgdorff et al., 2013; Andersen et al., 2014; Akazawa et al., 2020) and increased oxidative stress (Bogaard et al., 2009), leading to a mismatch between RVFW oxygen supply and demand. Increased RVFW collagen content has been found to be correlated with organ-level diastolic dysfunction and reduced RV compliance (Cheng et al., 2018).

2.2.3 Fiber-Level RV Remodeling in PH

Pressure overload has been shown to result in increased myofiber stiffness in experimental models of PH (Hill et al., 2014; Avazmohammadi et al., 2017b; Sharifi Kia et al., 2020), potentially due to reduced titin phosphorylation. Reduced titin phosphorylation and sarcomeric stiffening was also observed in RVFW tissues obtained from PH patients (Rain et al., 2013). Moreover, PH results in reduced RVFW collagen fiber crimp, leading to increased collagen recruitment rate and earlier engagement of collagen fibers under loading (Avazmohammadi et al., 2017b; Sharifi Kia et al., 2020). PH has also been shown to result in a denser and thicker network of collagen fibers in the RVFW (Stroud et al., 2002; Vélez-Rendón et al., 2019).

In addition to increased fiber-level stiffness, PH results in reorganization of the RVFW's transmural fiber architecture. Pressure overload has been shown to result in longitudinal realignment of RV collagen and myofibers, resulting in increased tissue-level anisotropy (Hill et al., 2014; Park et al., 2016; Avazmohammadi et al., 2017b; Sharifi Kia et al., 2020). Following an increase in RV pressures via PAB in a swine model of PH, Tezuka et al. observed RV fiber reorientation, while releasing the RV from the increased afterload (debanding) resulted in a shift in fiber architectures towards control levels within 7-17 days (Tezuka et al., 1990). In a mild, adaptive PAB model of PH, no differences were observed in transmural RVFW fiber orientations

(Nielsen et al., 2009). However, more severe PAB lead to longitudinal reorientation of RV collagen and myofibers (Hill et al., 2014; Avazmohammadi et al., 2017b; Sharifi Kia et al., 2020), indicating fiber reorientation as an end-stage remodeling event in PH. Reorientation of RV collagen and myofibers and alterations in the transmural fiber architecture of RV myocardium have the potential to affect organ-level contractility and result in RV-PA uncoupling with preserved cell-level myocyte contractility (Avazmohammadi et al., 2019a). However, the underlying mechanisms of RV fiber reorientation in PH have remained largely unexplored.

2.3 Effects of Potential Therapeutics on RV Biomechanics in PH

Despite recent developments of therapeutics for management of PH, so far, lung transplantation remains the only curative treatment. The renin-angiotensin-aldosterone system (RAAS) plays a major role in regulating RV remodeling in response to pressure overload (Menendez, 2016). Previous work has evaluated the effects of angiotensin II receptor blockers on RV remodeling in PH, by targeting the RAAS system and inhibiting the effects of AT1 receptor stimulation (which prohibits the increase of vascular tone and vasoconstriction). While angiotensin II receptor blockers have shown improvements in the setting of LV pressure overload, they did not show any effects on either compensated or decompensated RV failure, measured by RV pressures, cardiac output, dilation, contractility, and survival (Borgdorff et al., 2013; Andersen et al., 2014; Clements et al., 2019).

Moreover, integrin-linked kinase (ILK) is upregulated in PA vascular smooth muscle cells in PH, resulting in PA remodeling and proliferation. ILK inhibition was shown to result in reduced PA and RV hypertrophy, RV systolic and end-diastolic pressures, and improved contractility in

male, but not female rats in a SuHx model of PH (Shen et al., 2020). This was attributed to estrogen-mediated effects in females, as co-culture of human PA vascular smooth muscle cells with estrogen and ILK inhibitor, hindered the anti-proliferative effects of ILK inhibition (Shen et al., 2020).

Placement of mesenchymal stem cell (MSC)-seeded bioscaffolds on rat RVs in a SuHx model resulted in improved stroke volume, cardiac output, and diastolic function (measured by EDPVR), despite showing no effects on RV systolic pressures, $\frac{dp}{dt}_{\text{max and min}}$, and RV-PA coupling efficiency (Schmuck et al., 2019). Reduced RV fibrosis and myocyte hypertrophy, in addition to increased coronary perfusion were among the potential mechanisms of action for the observed effects.

Nitric oxide–dependent vasoactivity of the pulmonary vasculature affects RV afterload and function in PH (Simon et al., 2016). Clinical analysis of the acute effects of an inhaled formulation of sodium nitrite in patients with PH due to heart failure with preserved ejection fraction (PH-HFpEF) demonstrated reduced mean PA pressures and increased PA compliance, with no significant effects on PVR (Simon et al., 2016).

3.0 Analyzing the Effects of Angiotensin Receptor-Neprilysin Inhibition on Right Ventricular Biomechanics in Pulmonary Hypertension

Our findings on the effects of combined angiotensin receptor-neprilysin inhibition on right ventricular (RV) remodeling in pulmonary hypertension (PH) will be discussed in this chapter. The following results have been published in the Journal of the American Heart Association (Sharifi Kia et al., 2020).

3.1 Introduction

PH is a disease resulting in increased RV afterload, myocardial hypertrophy and ventricular remodeling. RV failure remains the main cause of mortality for nearly 70% of PH patients (Voelke et al., 2011) with 33-38% mortality rates 3 years post-diagnosis (Benza et al., 2007; Humbert et al., 2010). Pressure overload due to PH results in increased end-systolic and end-diastolic volumes as well as increased RV contractility (Hill et al., 2014), which if left unchecked leads to decreased RV contractility and eventual RV failure. Despite the development of multiple therapeutics for management of PH, lung transplantation remains the only curative treatment.

RV biomechanics has been closely linked to physiological function (Jang et al., 2017). From a biomechanical point of view, pressure overloaded RV myocardium experiences increased wall thickness, fiber remodeling and increased stiffness to restore cardiac output. RV remodeling and fiber re-orientation results in a pathological increase in stiffness and non-physiologic anisotropy in certain directions which affects the filling and ejection mechanics of the RV

(Avazmohammadi et al., 2019a), torsional motion of the heart, and transmural wall stress (Carruth et al., 2016). Biomechanical studies have provided important insights into RV remodeling in response to PH (Hill et al., 2014; Avazmohammadi et al., 2017a, 2017b, 2019a; Jang et al., 2017); however, limited information exists on the effects of therapeutic interventions on these mechanisms (Clements et al., 2019).

Sacubitril/Valsartan (Sac/Val; also known as LCZ696) is an angiotensin receptor-neprilysin inhibitor (ARNi) drug consisting of a 1:1 mixture of the neprilysin inhibitor sacubitril and the angiotensin receptor blocker valsartan which, based on evidence including a large placebo-controlled trial (McMurray et al., 2014), is FDA approved to reduce the risk of cardiovascular death and heart failure hospitalization for chronic systolic left ventricular (LV) heart failure (Menendez, 2016). While previous heart failure and hypertension therapeutics include angiotensin receptor blockers and target the renin-angiotensin-aldosterone system (RAAS), Sac/Val has a mode of action that targets both the RAAS and natriuretic peptides (NP) system. Valsartan inhibits the effects of AT1 receptor stimulation which prohibits the increase of vascular tone and vasoconstriction. Sacubitril, on the other hand, increases the NP levels via neprilysin inhibition which results in decreased blood pressure and prevents hypertrophy (Menendez, 2016).

Several preclinical studies have investigated the effects of Sac/Val treatment on LV pressure overload (Burke et al., 2019), myocardial infraction (Pfau et al., 2019) and left heart failure (Maslov et al., 2019a). In addition to preclinical studies, large clinical trials have analyzed the effects of Sac/Val treatment on left heart failure with preserved (Solomon et al., 2019) or reduced (McMurray et al., 2014) ejection fraction. Despite promising outcomes as a treatment for chronic systolic LV heart failure (McMurray et al., 2014) and demonstrating anti-fibrotic and anti-

inflammatory effects (Pu et al., 2008; Gu et al., 2010; Von Lueder et al., 2013; Burke et al., 2019), to date, there is limited data on the effects of Sac/Val treatment on RV remodeling events in PH.

In the current study, we aimed to understand the response of RV myocardium in PH to treatment with Sac/Val. We hypothesized that preventive treatment of PH with Sac/Val attenuates the development of RV hypertrophy and results in improved RV biomechanics. Terminal invasive hemodynamic measurements, quantitative histological analysis, biaxial mechanical testing, and constitutive modelling were employed to conduct a multi-scale analysis on the effects of Sac/Val on RV remodeling.

3.2 Methods

A rat pulmonary artery banding (PAB) model of PH (total of 58 male Sprague-Dawley rats) was used to evaluate the effects of Sac/Val treatment on the biomechanical properties of failing RV myocardium. Hemodynamic measurements were performed at the end of the treatment window, followed by biaxial mechanical testing of the right ventricular free wall (RVFW). An additional group of animals were used for quantitative histological analysis of RV collagen and myofiber architectures. Figure 4 summarizes the cohorts, experimental protocols, and different analysis techniques used in this work. All animal procedures were approved by the University of Pittsburgh's IACUC (protocol # 13021226) and were carried out in such a way as to minimize discomfort, distress, pain, and injury to animals. All surgical procedures were performed under isoflurane anesthesia followed by bupivacaine (2-3 mg/kg), buprenorphine (0.05-0.1 mg/kg) and ketoprofen (1mg/kg) administered as pain medications during and post-surgery. The animals were euthanized by harvesting the heart following hemodynamic data collection.

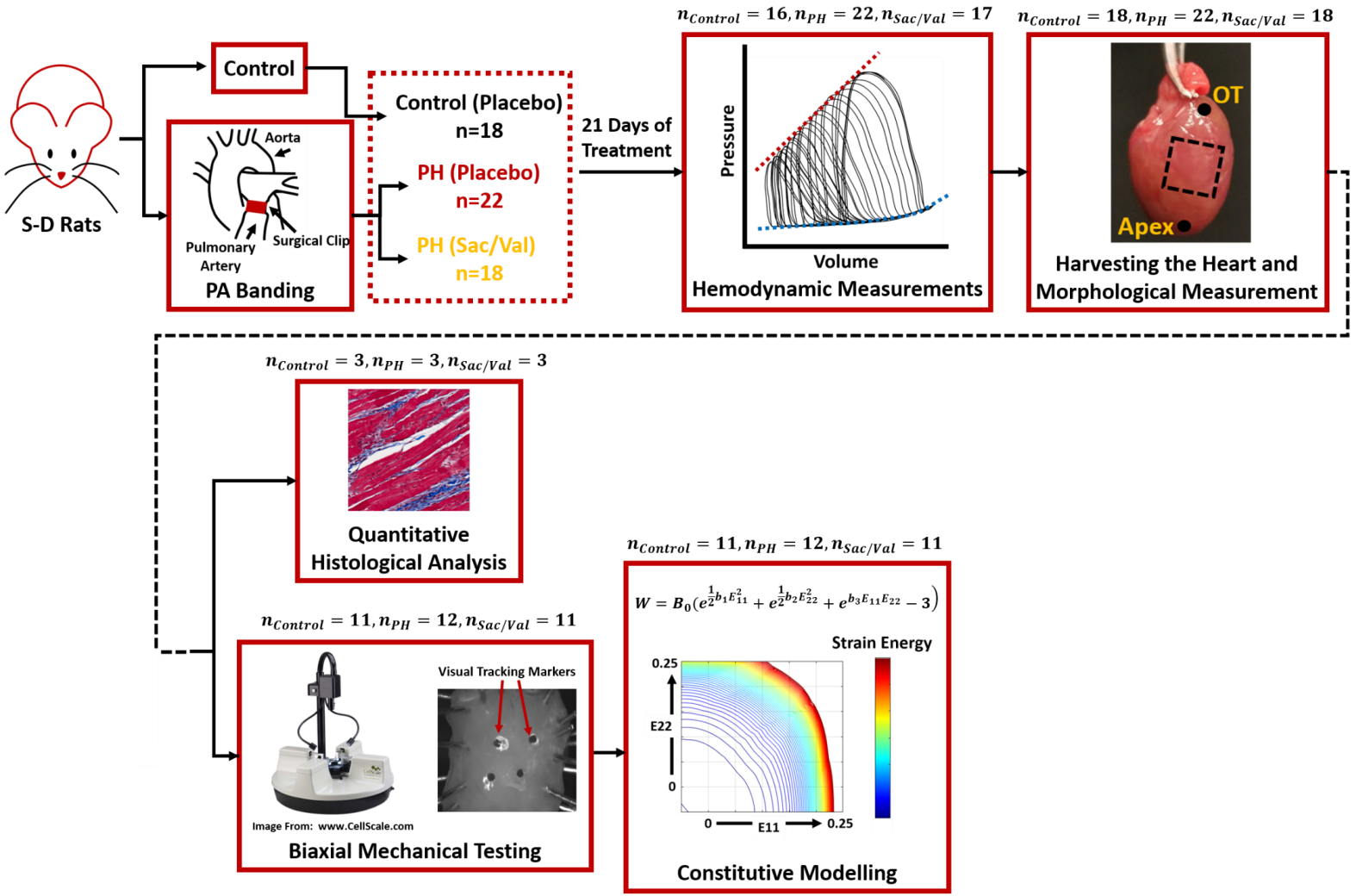

Figure 4 Summary of the framework developed to study the effects of Sac/Val on RV remodeling in PH. Sprague-Dawley rats were assigned to one of the Control, PH-placebo treated or PH-Sac/Val treated cohorts, followed by terminal invasive hemodynamic measurements, morphological measurements, quantitative histological analysis, biaxial mechanical characterization, and constitutive modeling.

3.2.1 Pulmonary Artery Banding Procedures and Drug Administration

RV pressure overload was induced via banding the main pulmonary artery (PA) of male Sprague-Dawley rats using an adjustable surgical clip (n=40, approximately 8 weeks old, weighing 200-250 g at the start of the experiments, sourced from Envigo, Indianapolis, IN).

As discussed in previous work (Valdez-Jasso et al., 2012; Hill et al., 2014), several factors were considered for our choice of this animal model. Briefly, this model causes RV pressure overload in the absence of confounding conditions, such as hypoxia, sufficient to study RV remodeling; a rat model was selected to provide a large enough sample of RVFW tissue for biaxial mechanical testing, while being thin enough to facilitate biaxial testing of intact full-thickness myocardium without the need for transmural sectioning, as well as maintaining tissue viability ex-vivo via passive diffusion.

Once anesthetized, rats were placed on a heated table to maintain a core temperature of 37°C and were monitored with a rectal probe. After endotracheal intubation, animals were placed on a volume ventilator (70 breaths/min, 6-8 mL/kg/min). The chest was then entered by a limited lateral incision to expose the mid-thoracic aorta. The PA was identified, and a surgical clip was placed around it with a radius such that a uniform RV systolic pressure of 40–50 mmHg was generated acutely (confirmed via hemodynamic measurements in pilot studies). The chest was then closed, and animals were extubated. Following the PAB procedure, rats were randomized into two cohorts: placebo-treated-PH and Sac/Val-treated-PH (Fig. 4). Additionally, a control group (n=18) consisted of unbanded age-matched placebo-treated animals. Daily doses of Sac/Val (68 mg/kg/day) or placebo (same volume of water) were administered via oral gavage for 21 days (Pu et al., 2008; Von Lueder et al., 2013).

3.2.2 Hemodynamic Measurements

Following the treatment window, terminal invasive hemodynamic measurements were performed to confirm RV pressure overload via standard catheterization techniques (Faber et al., 2006; Bogaard et al., 2009; Hill et al., 2014). RV pressure-volume (P-V) loops were acquired for each animal ($n_{Control} = 16, n_{PH} = 22, n_{Sac/Val} = 17$), using a Millar^{TM} conductance catheter (Millar Inc., Houston, TX). Hemodynamic data were processed using LabChart (ADInstruments, Sydney, Australia) and analyzed for measures of cardiac function, including maximum pressure, stroke volume, heart rate, maximum and minimum $\frac{dp}{dt}$, RV elastance (E_{es}), PA elastance (E_a) and RV-PA coupling (E_{es}/E_a). RV maximum pressure was measured as the difference between maximum and minimum pressures of a beat. RV elastance was measured via occlusion of the vena cava (Hill et al., 2014). Due to volume measurements performed in relative volume units (RVU), only relative volumetric data (such as stroke volume and E_{es}) are reported and used for data analysis. The heart was then harvested and placed in cardioplegic solution.

3.2.3 Histological Analysis

A sub-group of rats from each cohort were used for histological analysis. Based on our previous studies using this model of PH (Hill et al., 2014), a sample size of n=3/cohort was chosen for this aim with the primary goal of studying transmural RV fiber orientations. Specimen fixation was performed using 10% neutral buffered formalin. Histology was carried out using Masson's trichrome which distinctly stains myofibers in red and collagen in blue. A total of 17-25 transmural sections were taken from each RVFW specimen at 50 μm increments from epi- to endocardium.

Collagen (stained in blue) and myofibers (stained in red/pink) were segmented from the histological scans by manual thresholding of images based on the appropriate RGB range (Fig. 5).

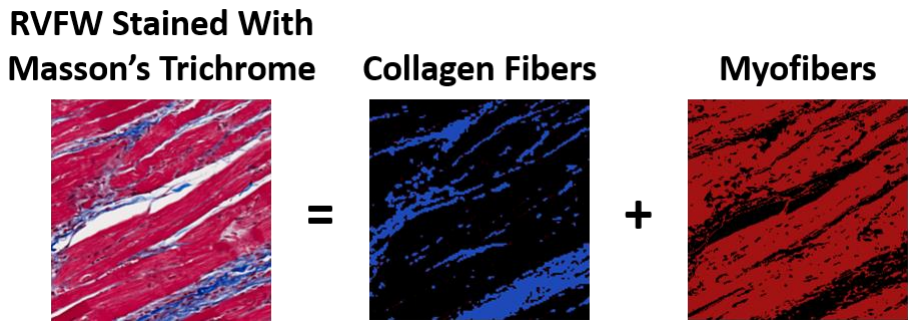

Figure 5 Threshold-based segmentation of collagen (blue) and myofibers (red) from the histological scans.

Area fraction of collagen fibers (measure of fibrosis) was evaluated by calculating the ratio of area occupied by the respective pixels (blue) over the total area in each cross-section. Average of all transmural measurements are reported as the collagen area fraction for each RVFW specimen. Transmural fiber orientation of collagen and myofibers were quantitatively analyzed using a gradient-based image analysis framework. Similar to our previous studies (Hill et al., 2014), the orientation angle and magnitude of the gradient were calculated at each pixel, followed by formation of the structure tensor of the gradient map for each histological section:

$$H = \begin{bmatrix} \sum_{i,j=1}^{i=n;\, j=m} G_{i,j}^2 \mathrm{Cos}^2\Phi_{i,j} & \sum_{i,j=1}^{i=n;\, j=m} G_{i,j}^2 \mathrm{Cos}\Phi_{i,j}\mathrm{Sin}\Phi_{i,j} \\ \sum_{i,j=1}^{i=n;\, j=m} G_{i,j}^2 \mathrm{Cos}\Phi_{i,j}\mathrm{Sin}\Phi_{i,j} & \sum_{i,j=1}^{i=n;\, j=m} G_{i,j}^2 \mathrm{Sin}^2\Phi_{i,j} \end{bmatrix} \quad (3\text{-}1)$$

Here, $G_{i,j}$ and $\Phi_{i,j}$ are the magnitude of the gradient and the orientation angle at each point, respectively. Dominant fiber orientations at each section were obtained by evaluating the dominant orientation (first eigenvector) of the resulting structure tensor from each histological image (Rezakhaniha et al., 2012; Püspöki et al., 2016). Transmural fiber angles are reported against normalized RVFW thickness at 11 different cross-sections (0-100% thickness). Linear interpolations were performed to report the final data for all cohorts on an evenly spaced grid. Based on our previous studies on this model of PH (Hill et al., 2014), linear interpolations adequately approximate the transmural change in fiber angles. We assigned 0° to the longitudinal (apex to outflow-tract/base) and 90° to the circumferential (free wall to septum) direction, when looking at the RVFW from the epicardium.

In addition to fiber orientations, coherency of collagen fiber distributions was calculated to analyze the structural arrangement of collagen fibers in each layer:

$$C = \frac{\lambda_{max} - \lambda_{min}}{\lambda_{max} + \lambda_{min}} \times 100 \qquad (3\text{-}2)$$

Here, λ_{max} and λ_{min} are the first and second eigen values of the structure tensor in equation 3-1, respectively (Rezakhaniha et al., 2012). Coherency evaluates the local alignment of collagen fibers with C=0% indicating an isotropic distribution and C=100% indicating a highly aligned pattern. This helps evaluating the level of collagen crimp in each cohort (higher C indicating less crimp), as an important contributor to tissue architecture and biomechanical properties. Average of all transmural measurements are reported as %collagen coherency for each specimen. Furthermore, RVFW area was obtained for each specimen based on histological sections followed by calculation

of RVFW wet tissue density by dividing RVFW mass by volume (area × wall thickness). Image processing and fiber orientation analysis was performed using the OrientationJ toolbox (Rezakhaniha et al., 2012; Püspöki et al., 2016) in ImageJ (imagej.nih.gov).

3.2.4 Biaxial Mechanical Testing

Another group of rats from each cohort ($n_{Control} = 11, n_{PH} = 12, n_{Sac/Val} = 11$) underwent biaxial mechanical testing to investigate the effects of Sac/Val treatment on the biomechanical properties of viable RV myocardium in PH. Square specimens were dissected from the RVFW (Fig. 4) and mounted on a biaxial testing device (BioTester, CellScale,Waterloo, ON, Canada) using sutures and metal hooks to minimize shear loading (Sacks, 1999). The RVFW was submerged in modified Krebs solution with 2,3-butanedione monoxime (BDM) and oxygen (Valdez-Jasso et al., 2012) during testing. Our previous studies have shown the effectiveness of this technique in maintaining tissue viability via passive diffusion, up to 1.5 hours post-harvesting (Hill et al., 2014). Multi-protocol biaxial testing (Fig. 6a) was performed on each specimen to investigate the tissue response in a wide range of possible loading scenarios (displacement-controlled 1:1, 1:2, 2:1, 1:4, 4:1, 1:6, and 6:1 loading ratios). Each specimen underwent 15 cycles of preconditioning under 1:1 displacement-controlled loading, before the start of data acquisition (Fig. 6b).

A set of four visual tracking markers were placed on the epicardium. Marker displacements were recorded using a CCD camera and further analyzed for strain estimations. The deformation gradient tensor was then reconstructed from marker displacements as (Zhang et al., 2015):

$$F = \frac{dx}{dX} \tag{3-3}$$

where F is the deformation gradient tensor, X is the reference coordinate and x is the deformed coordinate system. Using F, the Green–Lagrange strain tensor (E) was calculated as:

$$E = \frac{1}{2}(F^T F - I) \tag{3-4}$$

Load measurements from the biaxial device and initial specimen dimensions were used to reconstruct the first Piola–Kirchhoff stress tensor (P) via standard methods (Valdez-Jasso et al., 2012; Hill et al., 2014). The second Piola–Kirchhoff (2nd P-K) stress tensor (S) was then calculated as:

$$S = PF^{-T} \tag{3-5}$$

A plane stress approximation was used to calculate the biomechanical behavior of RVFW. Stress-strain response of each specimen was calculated using a finite deformation framework developed in Mathcad (PTC, Needham, MA).

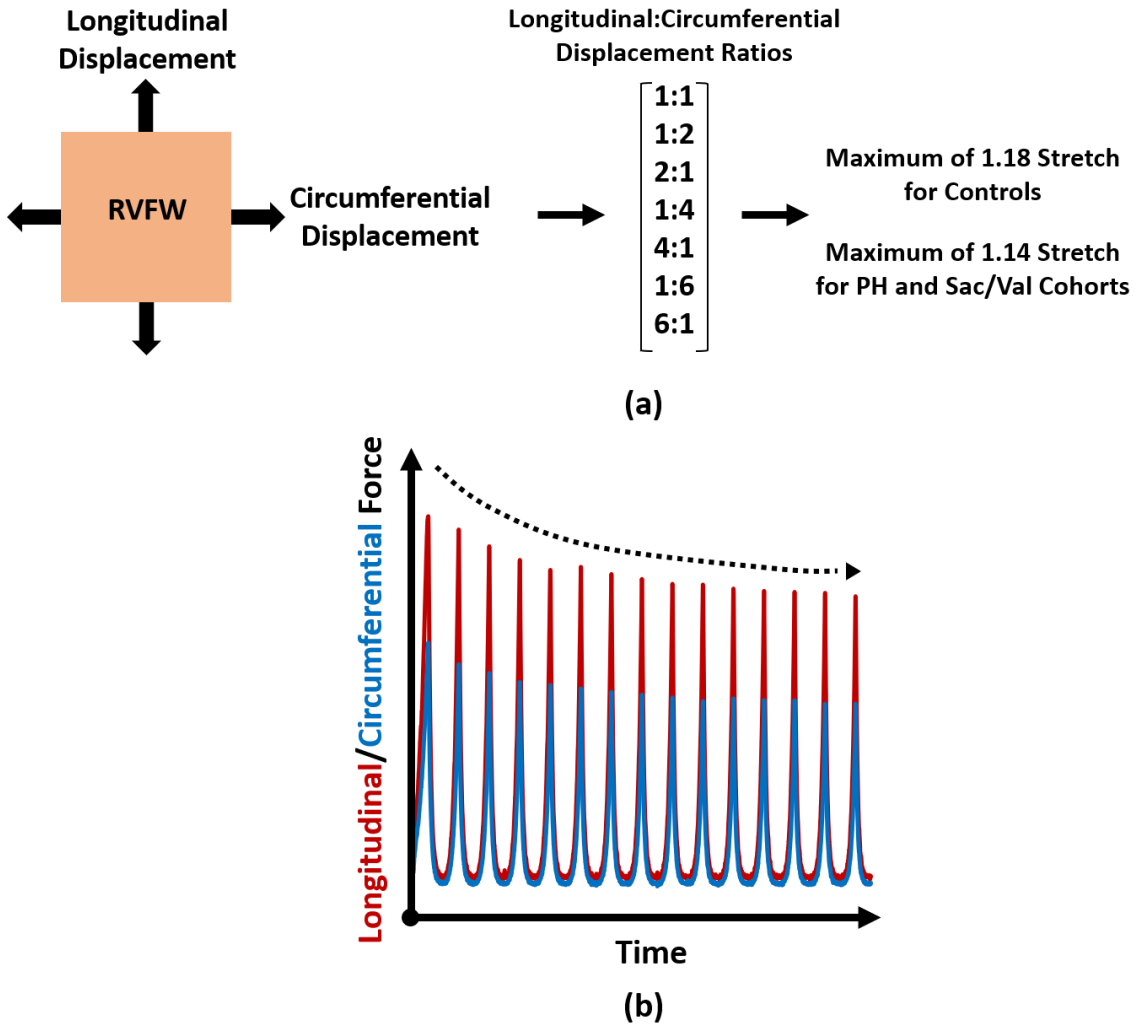

Figure 6 Displacement-controlled biaxial mechanical testing of RVFW specimens. (a) Loading direction, ratios, and maximum displacements applied to specimens from each cohort. (b) Representative temporal force measurements during a pre-conditioning cycle, demonstrating the stabilization of longitudinal and circumferential forces.

Equibiaxial strain-controlled loading results in unique tissue kinematics with no fiber rotations (Sacks, 2003) and, therefore, could be used to estimate fiber-level mechanical properties from tissue-level measurements (Hill et al., 2014; Avazmohammadi et al., 2017a). Since experimental equibiaxial displacement-controlled loading may not always translate to equibiaxial

strains, equibiaxial strain-controlled response of the RVFW tissues were interpolated from the multi-protocol experimental data, using previously established techniques (Fata et al., 2014; Hill et al., 2014). As seen in Figure 7a, the equibiaxial response (shown in blue) was interpolated from the multi-protocol experimental data (shown in red) by fitting a mesh grid to the biaxial stress-strain scattered data points. Equibiaxial responses were approximated using biharmonic spline interpolations in MATLAB (Mathworks, Natick, MA). Similar to prior studies (Fata et al., 2014; Hill et al., 2014), effective fiber ensemble (EFE) stresses were then obtained from the equibiaxial data as:

$$S_{EFE} = S_{11} + S_{22} \tag{3-6}$$

Here, S_{EFE} represents the effective fiber ensemble stress and S_{11} and S_{22} are the interpolated biaxial tissue-level stresses in the longitudinal and circumferential directions, under equibiaxial strain-controlled loading. The stress-strain plot demonstrating S_{EFE} vs. equibiaxial strain (Fig. 7b) represents the fiber-level response of combined RVFW collagen and myofiber bundles, independent of fiber orientation. Estimating fiber-level properties using the described technique mitigates any possible sample mounting/misalignment errors during experimental testing and facilitates direct comparison of fiber-level properties between specimens from different cohorts.

Fiber-level properties were used for estimation of the intrinsic myofiber stiffness for specimens in each cohort. Myofibers were assumed to be mainly responsible for the initial portion of the stress-strain curve (Fig. 7b), followed by collagen recruitment (un-crimping) and a stiffer high-stress response. The fiber-level stress response for each specimen was differentiated with

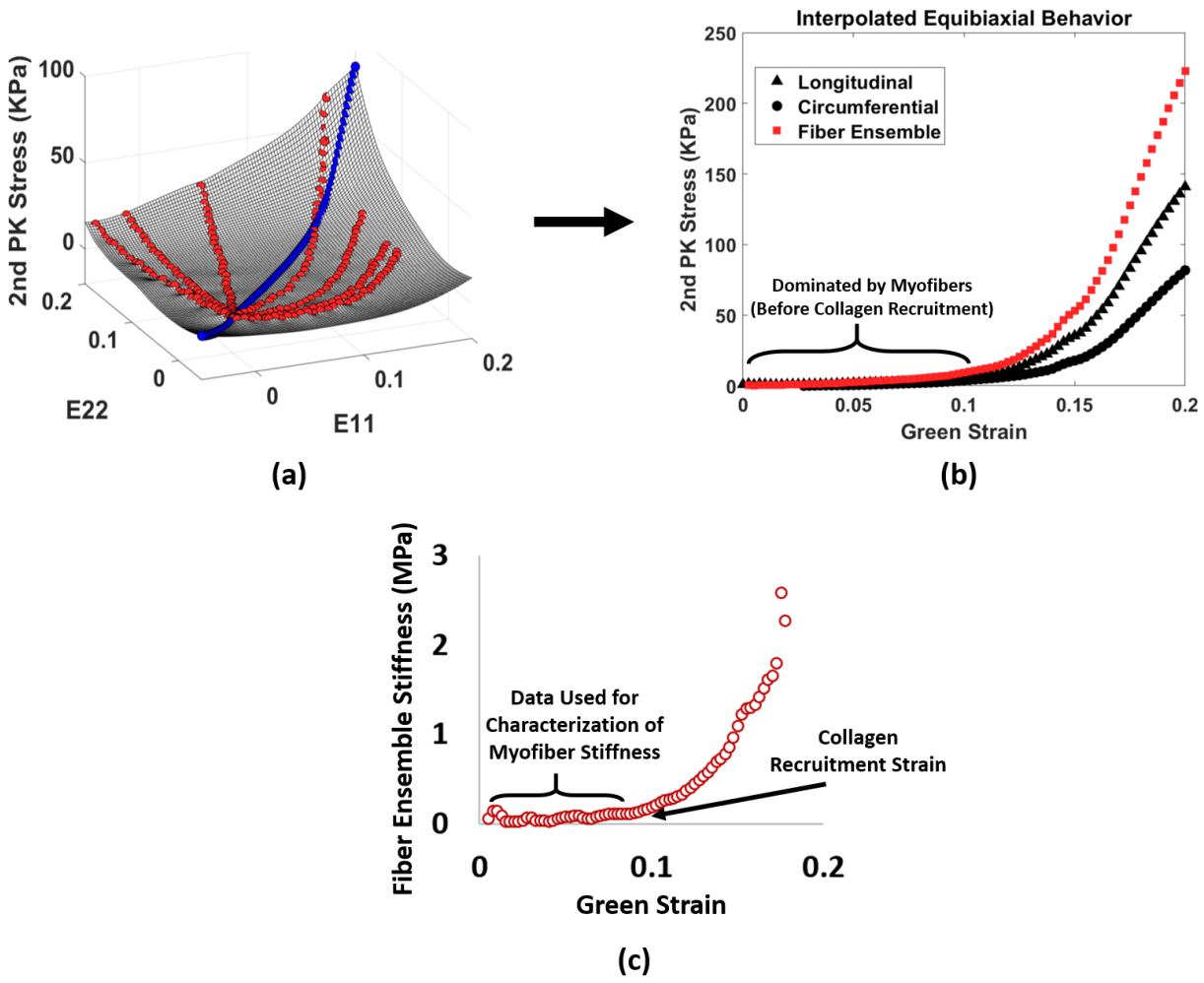

Figure 7 (a) Representative demonstration of interpolation of the RVFW stress response under equibiaxial strain-controlled loading (blue) using the scattered multi-protocol stress-strain measurements (red; 1:1, 1:2, 2:1, 1:4, 4:1, 1:6, and 6:1 loading ratios). The demonstrated interpolation shows the stress estimations for only one component of the biaxial RVFW stress response. Similar interpolations were reiterated for stress estimations in the other direction. E11 and E22 represent the biaxial Green-Lagrange strain measurements, while 2nd PK stress shows the 2nd Piola-Kirchhoff stress. (b) Approximation of the effective fiber ensemble stress-strain response (shown in red) from equibiaxial tissue-level measurements. (c) Differentiation of the fiber ensemble response for estimation of fiber-level stiffness and identification of collagen recruitment strain.

respect to strain in order to evaluate fiber stiffness changes over the range of measured strain (Fig. 7c). The general behavior observed for specimens included a relatively constant-stiffness region (myofibers) followed by an increased stiffness region (collagen recruitment). The fiber-level stress-strain data before the start of collagen recruitment was used for estimating myofiber properties for each specimen using a rule of mixtures approach (Humphrey and Rajagopal, 2002):

$$E_{\text{Myofiber}} = \frac{TM_{\text{Before Collagen Recruitment}}}{\Phi_{\text{Myofiber}}} \tag{3-7}$$

Here, E_{Myofiber} is the intrinsic myofiber stiffness, $TM_{\text{Before Collagen Recruitment}}$ is the slope of the line fitted to the fiber-level stress-strain data before collagen recruitment strain (via linear regression) and Φ_{Myofiber} is the area fraction of myofibers in each cohort obtained from histological analysis.

3.2.5 Constitutive Modelling

The experimentally obtained stress-strain data was used to model the response of specimens using a nonlinear anisotropic constitutive model (Choi and Vito, 1990):

$$W = B_0(e^{\frac{1}{2}b_1E_{11}^2} + e^{\frac{1}{2}b_2E_{22}^2} + e^{b_3E_{11}E_{22}} - 3) \tag{3-8}$$

Here, W is the strain energy, B_0 is a scaling factor, b_1 is a metric for stiffness in the longitudinal direction (apex to outflow-tract/base direction), b_2 is a metric for stiffness in the circumferential

direction, b_3 represents the degree of longitudinal-circumferential coupling and E_{11} and E_{22} are the longitudinal and circumferential Green-Lagrange strains, respectively. By differentiating the strain energy function (W) with respect to strain, stress components were obtained as:

$$S_{11} = \frac{\partial W}{\partial E_{11}} = B_0(b_1 E_{11} e^{\frac{1}{2}b_1 E_{11}^2} + b_3 E_{22} e^{b_3 E_{11} E_{22}})$$
$$S_{22} = \frac{\partial W}{\partial E_{22}} = B_0(b_2 E_{22} e^{\frac{1}{2}b_2 E_{22}^2} + b_3 E_{11} e^{b_3 E_{11} E_{22}}) \quad (3\text{-}9)$$

Here, S_{11} and S_{22} are the 2nd P-K stress components in the longitudinal and circumferential directions, respectively. Experimental stress-strain data was used to estimate model parameters for each specimen based on equation 3-9. Parameter estimation was performed using a custom nonlinear least-squares optimization algorithm (trust-region-reflective) in MATLAB. Goodness of fit was evaluated using a R^2 measure. Model parameters were compared to analyze the effects of PH and Sac/Val treatment on RVFW anisotropy and stiffness in different directions (B_0*b_1, B_0*b_2 and B_0*b_3 reported as "Longitudinal Stiffness", "Circumferential Stiffness" and "Coupled Stiffness", respectively (Kural et al., 2012)). Biomechanical responses were compared by investigating the model-derived strain energy space for specimens in each cohort. Cohort-specific strain energy maps (in the longitudinal-circumferential strain space) were generated using the median of all strain energy distributions for specimens in each cohort.

3.2.6 Statistical Analysis

Transmural distribution of collagen and myofiber angles, collagen area fraction and coherency, biaxial mechanical properties, and fiber-level stress-strain data are reported as mean ± standard deviation. All other data are presented with median, mean, standard deviation and interquartile range.

Sample normality and homoscedasticity were assessed using the Shapiro–Wilk test and Bartlett's test, respectively, in order to identify the appropriate parametric/non-parametric test for our analysis. For the transmural fiber orientation measurements, circular statistics were used to calculate the circular mean and standard deviation, followed by statistical testing using the Watson–Williams test (equivalent of one-way ANOVA for circular data). Comparisons were performed using the CircStat toolbox (Berens, 2009) in MATLAB. All other histological data (n=3) were analyzed by one-way ANOVA followed by post-hoc t-tests with Bonferroni correction. For all other data, statistical analysis was performed using the Kruskal-Wallis test. In case of statistical significance, pairwise Wilcoxon rank sum tests were performed for post-hoc testing with Bonferroni correction. Statistical comparisons were performed using the R software package (R Foundation for Statistical Computing, Vienna, Austria, www.R-project.org). For all purposes, $p<0.05$ was considered statistically significant.

3.3 Results

3.3.1 Hemodynamics and Remodeling

Effects of pressure overload and Sac/Val treatment on RV hemodynamics are demonstrated in Figure 8 ($n_{Control} = 16, n_{PH} = 22, n_{Sac/Val} = 17$). PA banding resulted in significant increase in the maximal RV pressure (Fig. 8a; 67.5±16.2 mmHg for PH vs. 23.8±2.8 mmHg for Control). Sac/Val treatment demonstrated lower pressures compared to the PH group, while still being higher than control levels (47.9±13.9 mmHg). RV stroke volume significantly decreased in response to PH, with Sac/Val treatment showing no significant effects compared to both control and PH cohorts (Fig. 8b; 4.7±1.1, 3.3±1.2 and 3.7±1.6 RVU for Control, PH and Sac/Val, respectively). Heart rate was not different among different cohorts (Fig. 8c; 294.0±39.0, 291.4±59.7 and 284.9±37.2 BPM for Control, PH and Sac/Val, respectively).

Maximal and minimal $\frac{dp}{dt}$ (load-dependent measures of RV contractility and relaxation) increased and decreased, respectively, in response to PH (Fig. 8d-e; $\frac{dp}{dt}_{\max}$: 2440.9±812.9 mmHg/Sec for PH vs. 1112.2±242.9 mmHg/Sec for Control; $\frac{dp}{dt}_{\min}$: -2290.1±844.7 mmHg/Sec for PH vs. -873.0±263.2 mmHg/Sec for Control). Sac/Val treatment significantly decreased $\frac{dp}{dt}_{\max}$ (1719.1±590.9 mmHg/Sec) and increased $\frac{dp}{dt}_{\min}$ (-1635.2±684.1 mmHg/Sec) compared to PH levels. E_a (measure of vascular load) increased in PH, while Sac/Val resulted in significant improvements (Fig. 8f; 5.9±2.6, 25.0±9.1 and 16.2±8.2 for Control, PH and Sac/Val, respectively). E_{es} (load-independent measure of RV contractility) was obtained only for a sub-group of animals in each cohort ($n_{Control} = 10, n_{PH} = 15, n_{Sac/Val} = 11$) due to difficulties associated with vena

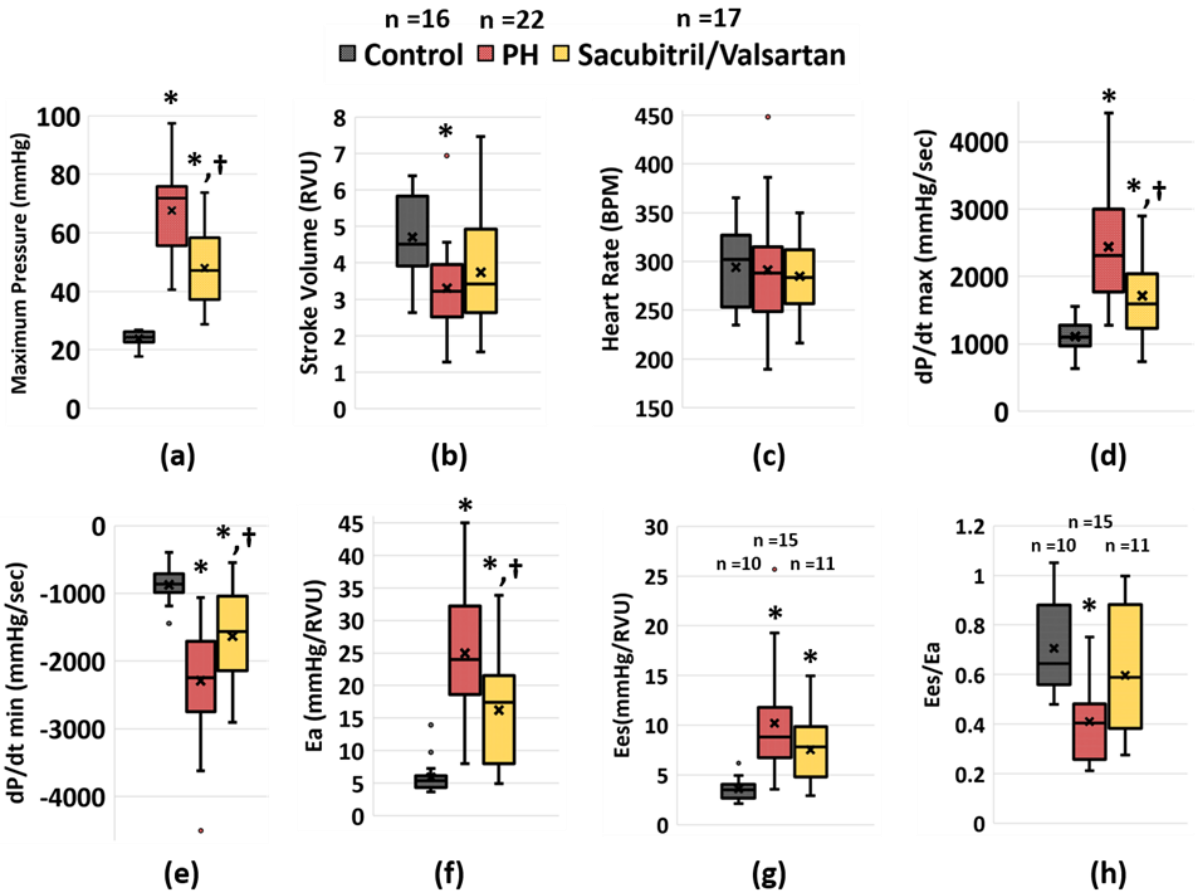

Figure 8 Hemodynamic measurements of the effects of PH and Sac/Val treatment on (a) RV maximum pressure, (b) Stroke volume, (c) Heart rate, (d) $\frac{dp}{dt}$max, (e) $\frac{dp}{dt}$min, (f) PA elastance (E_a), (g) RV elastance (E_{es}) and (h) Ratio of RV to PA elastance ($\frac{Ees}{Ea}$). Sac/Val treatment significantly lowered RV maximum pressure (P_{max}), decreased the load-dependent measure of contractility ($\frac{dp}{dt}$max), increased the load-dependent measure of relaxation ($\frac{dp}{dt}$min) and decreased PA elastance (E_a) in addition to preventing RV-PA uncoupling. Horizontal line (—) and cross (✕) representing median and mean of distributions, respectively. * indicates p<0.05 compared to Control, † indicates p<0.05 compared to PH.

cava occlusions. E_{es} significantly increased in PH and was not affected by Sac/Val treatment (Fig. 8g; 3.6±1.2, 10.2±5.8 and 7.5±3.4 mmHg/RVU for Control, PH, and Sac/Val, respectively). Ratio of E_{es} to E_a significantly decreased in PH, indicating decompensated RV-PA coupling. Sac/Val

treatment prevented a significant drop from control levels (Fig. 8h; 0.71±0.18, 0.41±0.15 and 0.60±0.24 for Control, PH and Sac/Val, respectively). Full statistical results of the hemodynamics are presented in Appendix Table S1.

As shown in Figure 9 and Appendix Table S2, PH resulted in RVFW hypertrophy (increased wall thickness) and increased RV/LV mass ratio (RVFW Thickness: 1.34±0.23 mm for PH vs. 0.66±0.09 mm for Control; RV/LV Mass Ratio: 0.57±0.08 for PH vs. 0.28±0.02 for Control). Sac/Val treatment resulted in significant improvements in RVFW hypertrophy (1.13±0.17 mm), while showing no statistical significance on RV/LV mass ratio (0.51±0.13).

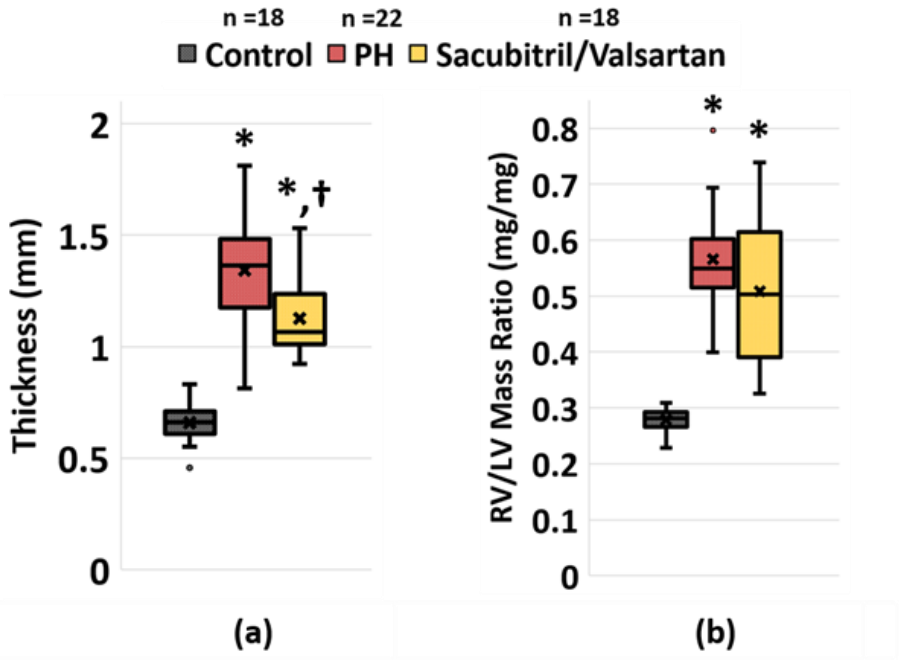

Figure 9 Effects of PH and Sac/Val treatment on (a) RV hypertrophy (RVFW thickness) and (b) RV to LV mass ratio. Sac/Val resulted in significantly lower RV wall thickness, while not demonstrating significant effects on RV to LV mass ratio. Horizontal line (—) and cross (×) representing median and mean of distributions, respectively. * indicates p<0.05 compared to Control, † indicates p<0.05 compared to PH.

3.3.2 Fiber Angle

Histological analysis ($n_{Control} = 3, n_{PH} = 3, n_{Sac/Val} = 3$) showed transmural re-orientation of collagen and myofibers towards the longitudinal direction (apex to outflow-tract/base) in PH, in addition to increased collagen content and fibrosis (Fig. 10a-e, Appendix Table S3). Collagen fiber orientations were similar to myofiber orientations in each cohort (Fig. 10b-c). Sac/Val treatment prevented transmural re-orientation of both collagen and myofibers except for the sub-endocardial region where fiber re-orientation was observed (Myofiber Angle Range from Epi- to Endocardium: -52.4°→+7.4°, -56.9°→+39.5°, -57.8°→+25.2° for Control, PH and Sac/Val, respectively; Collagen Fiber Angle Range from Epi- to Endocardium: -49.9°→+2.6°, -59.6°→+39.0°, -66.0°→+24.0° for Control, PH and Sac/Val, respectively). Dominant transmural orientation of collagen and myofibers for specimens in each cohort was obtained by calculating the circular mean of the transmural distribution of fiber angles (dotted lines in Fig. 10b and c). As shown in Figure 10d, PH resulted in rotation of the dominant orientation of myofibers towards the longitudinal direction by ~15.5°, while Sac/Val prevented this remodeling (Dominant Myofiber Orientation: -21.1±0.1°, -5.8±3.2° and -19.8±3.0° for Control, PH and Sac/Val, respectively). Collagen area fraction (measure of fibrosis) increased in response to PH while Sac/Val treatment did not result in significant improvements (Fig. 10e; Collagen Area Fraction: 5.5±1.1%, 12.4±2.7% and 10.8±0.8% for Control, PH and Sac/Val, respectively). Collagen fiber coherency (Fig. 10f) did not show any statistically significant differences for either PH or Sac/Val cohorts (16.5±1.5%, 21.1±2.5% and 21.1±2.1% for Control, PH and Sac/Val, respectively).

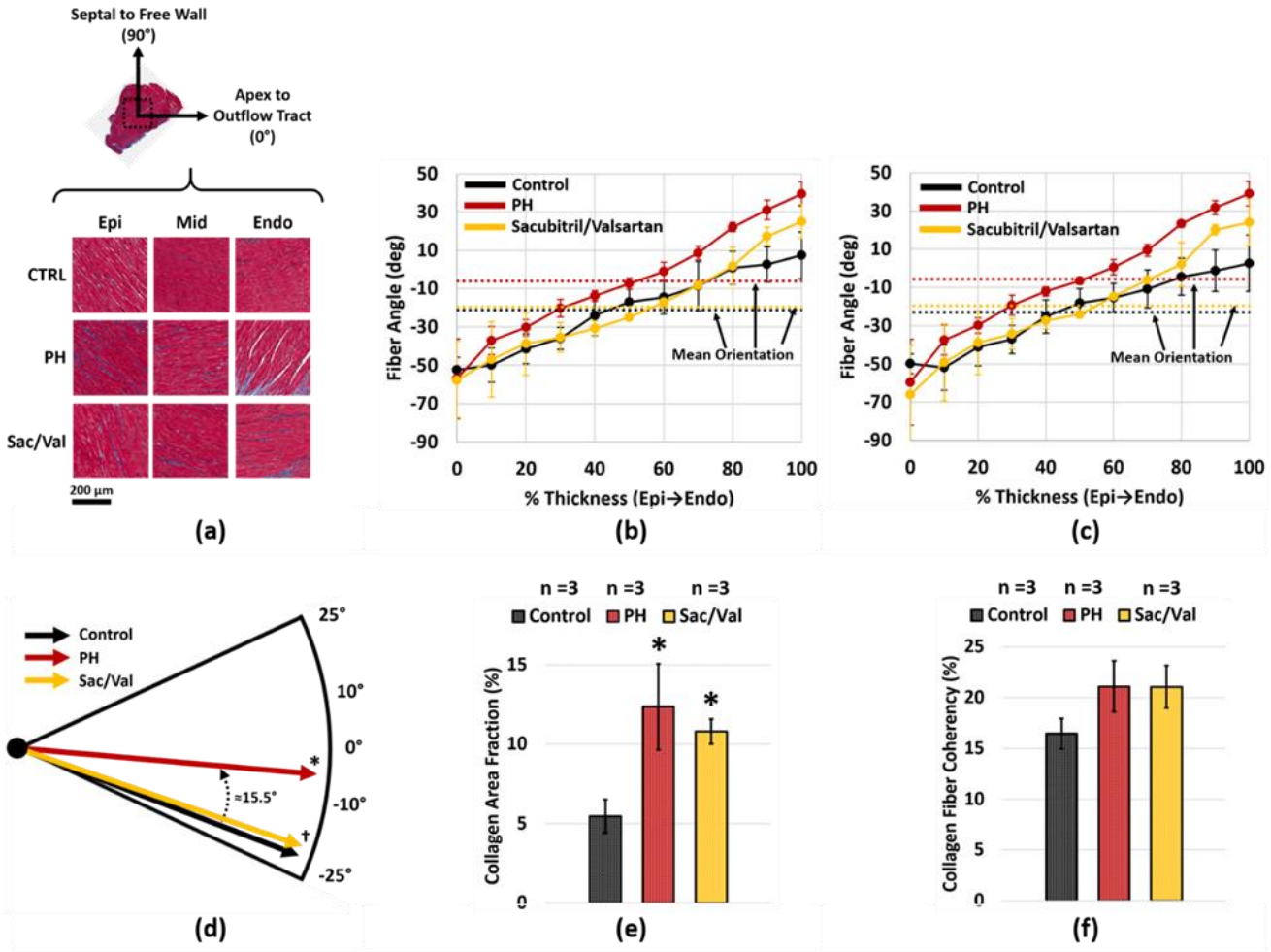

Figure 10 (a) Representative transmural histological sections of RV myocardium from each cohort (Red/Pink: Myofiber, Blue: Collagen). Coordinates used to measure fiber orientations indicated on the top. (b) Effects of Sac/Val treatment on transmural myofiber orientations, and (c) Collagen fiber orientations, (d) Dominant myofiber orientation in each cohort, (e) Effects of Sac/Val on RV collagen area fraction, (f) Effects of Sac/Val on RV collagen fiber coherency. Error bars representing standard deviations. * indicates p<0.05 compared to Control, † indicates p<0.05 compared to PH.

Furthermore, RVFW area showed no statistically significant differences in either cohort (67.2±2.0, 105.4±14.5 and 85.5±23.3 mm^2 for Control, PH and Sac/Val, respectively). Bulk RVFW wet tissue density significantly decreased in PH that was prevented by Sac/Val treatment (5.22±0.35, 2.66±0.47 and3.96±0.65 mg/mm^3 for Control, PH and Sac/Val, respectively).

3.3.3 Biomechanics

Biaxial testing ($n_{Control} = 11, n_{PH} = 12, n_{Sac/Val} = 11$) demonstrated significantly increased stiffness in both longitudinal and circumferential directions as a result of PH (Fig. 11a). Sac/Val treatment improved RVFW biaxial biomechanical properties in both directions. Fiber-level stiffness of the combined collagen and myofiber bundles increased in PH while Sac/Val treatment resulted in decreased stiffness compared to PH levels (Fig. 11b). Furthermore, the intrinsic myofiber stiffness of RV specimens increased in PH (Fig. 11c, Appendix Table S4; 168.4±101.0 kPa for PH vs. 81.0±29.6 kPa for Control). Sac/Val treatment resulted in significantly lower stiffness than the PH cohort (65.4±53.4 KPa) while showing no difference with controls. Collagen recruitment strain decreased significantly as a result of PH with Sac/Val demonstrating no significant effects (Fig. 11d; 10.0±2.2%, 3.9±0.9% and 4.4±1.2% for Control, PH and Sac/Val, respectively).

Constitutive modelling revealed increased stiffness in the longitudinal and circumferential directions as well as increased in-plane coupling due to PAB (Fig. 12a, Appendix Table S4; Longitudinal Stiffness: 68.2±26.6 KPa for PH vs. 16.4±5.4 KPa for Control, Circumferential Stiffness: 31.5±11.3 KPa for PH vs. 14.8±8.3 KPa for Control, Coupled Stiffness: 38.3±24.9 KPa for PH vs. 11.1±4.4 KPa for Control). Sac/Val treatment resulted in significantly lower stiffness in both longitudinal and circumferential directions, but no statistically significant effects were

observed for the coupled stiffness (Fig. 12a; Longitudinal Stiffness: 39.1±16.9 KPa, Circumferential Stiffness: 18.7±8.4 KPa, Coupled Stiffness: 21.7±10.6 KPa). Overall, the constitutive model used in this study showed an acceptable performance in fitting our experimental data (R^2: 0.95±0.02, 0.91± 0.05 and 0.93±0.03 for Control, PH and Sac/Val, respectively). Cohort-specific strain energy maps (median of strain energy distributions of samples in each cohort; Fig. 12b) demonstrate the combined effects of all model parameters on RV biomechanical properties and provide a convenient summary of the effect of PH and Sac/Val treatment on the biomechanics of RVFW tissue. With a certain amount of strain energy, the PH tissue deforms less than the control cohort in both circumferential and longitudinal directions (indicating increased stiffness), while the Sac/Val strain energy map shows similar deformation patterns to controls.

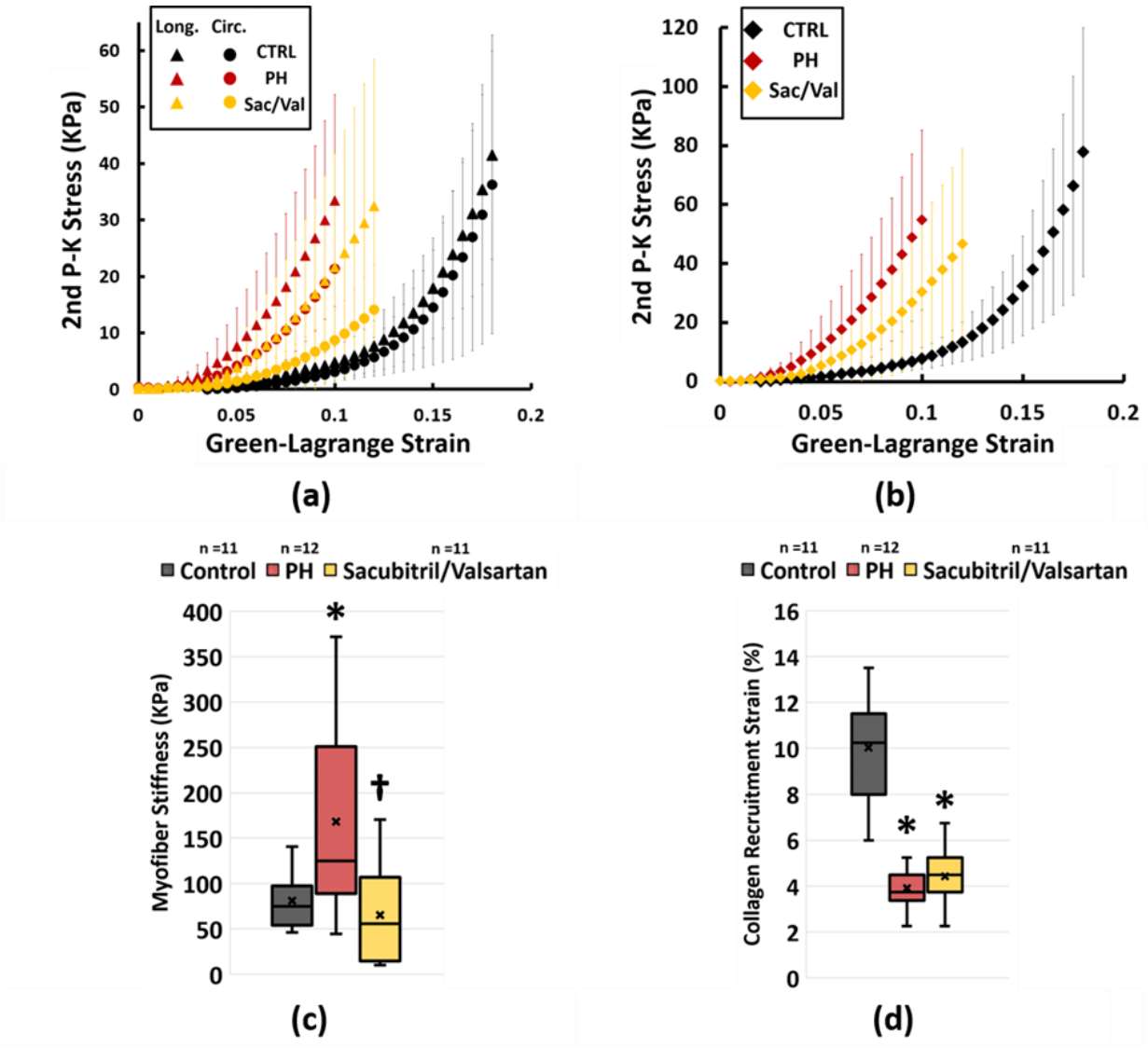

Figure 11 Effects of Sac/Val treatment on (a) Biaxial mechanical properties of RVFW, (b) Fiber-level mechanical properties of combined collagen and myofiber bundles, (c) Intrinsic myofiber stiffness, (d) Collagen recruitment strain. Sac/Val treatment resulted in improved tissue-level biomechanical properties. At the fiber-level, Sac/Val prevented an increase in myofiber stiffness in PH, but did not affect collagen recruitment strains. Horizontal line (—) and cross (X) representing median and mean of distributions, respectively. Error bars in parts (a) and (b) representing standard deviations. * indicates $p<0.05$ compared to Control, † indicates $p<0.05$ compared to PH.

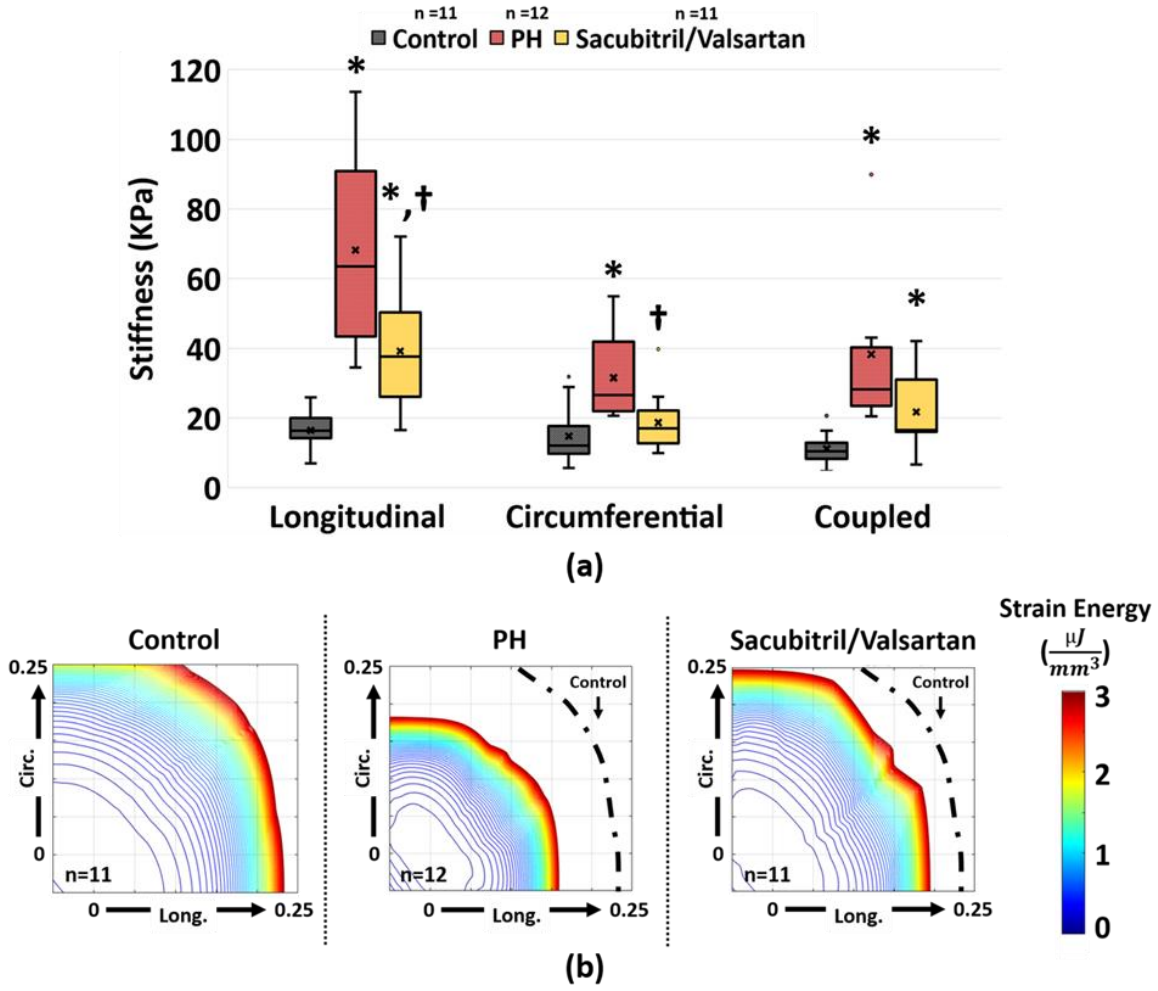

Figure 12 (a) Longitudinal, circumferential and coupled stiffness of RV myocardium revealed by constitutive modeling, (b) Cohort-specific strain energy maps of RV myocardium, indicating increased stiffness in PH and improved biomechanical performance with Sac/Val treatment. Sac/Val improved RV stiffness in both circumferential and longitudinal directions with no significant effects on in-plane coupling. Dashed lines indicate the strain energy levels for the control cohort at 3 $\frac{\mu J}{mm^3}$. Horizontal line (—) and cross (×) representing median and mean of distributions, respectively. * indicates p<0.05 compared to Control, † indicates p<0.05 compared to PH.

3.4 Discussion and Conclusions

In this work, we aimed to evaluate the effectiveness of Sac/Val treatment to prevent RV remodeling in PH. The primary findings of this study were: 1) Sac/Val treatment decreased RV maximum pressures, improved RV contractile and relaxation functions and prevented RV-PA uncoupling; 2) Sac/Val attenuated RV hypertrophy and prevented transmural re-orientation of RV collagen and myofibers; 3) Sac/Val resulted in improved RV biomechanical properties at the tissue level and prevented increased myofiber stiffness in PH.

Sac/Val decreased RV maximum pressures by 29% (Fig. 8a). This is consistent with reported effects of Sac/Val in other animal models of PH (Clements et al., 2019). Sac/Val treatment also prevented the alterations in load-dependent measures of contractility ($\frac{dp}{dt}_{\max}$) and relaxation ($\frac{dp}{dt}_{\min}$), caused by PA banding (Fig. 8d-e; 30% reduction and 29% increase, respectively). As suggested by previous investigations (Maslov et al., 2019b), effects of ARNi on load-dependent contractile and relaxation functions are likely a direct result of the synergy between sacubitril and valsartan. PA banding resulted in increased RV contractility (E_{es}) in response to increased afterload (E_a) (Fig. 8f-g), however the increased contractility was not sufficiently matched to the increased afterload, which resulted in uncoupling of RV-PA function (E_{es}/E_a) and decompensated RV failure (Fig. 8h). Sac/Val hampered an increase in RV afterload (35% improvement) and prevented RV-PA uncoupling, while showing no significant effects on E_{es} (Fig. 8f-h). Given our preventive treatment approach in this study, the observed effects on afterload more likely indicate the role of Sac/Val in arresting progressive RV remodeling post-banding. Similar improvements in RV function, reduced PA pressures and RV-PA recoupling were observed in recent clinical case reports on effects of Sac/Val treatment on 3 patients with PH due to left heart disease (PH-LHD)

(De Simone et al., 2019; Giammarresi et al., 2019). The observed effects in this study may suggest a direct ventricular remodeling (as opposed to pulmonary vascular remodeling) mechanism with Sac/Val treatment, due to the presence of a fixed arterial occlusion in our PAB model.

A significant increase in RV wall thickness and mass were observed in PH (Fig. 9). Clinically, hypertrophy has been identified as an initial adaptive response in PH in order to increase RV contractility and the resultant chamber pressure to pump against the increased afterload (Voelke et al., 2011). This was also observed in our previous studies using a similar animal model (Hill et al., 2014). Similar to previous studies (Clements et al., 2019), Sac/Val treatment resulted in significant improvements (16%) in RV hypertrophy, while not affecting RV mass, suggesting an overall increase in RVFW density with Sac/Val treatment compared to PH (decrease in volume with relatively similar RV mass), consistent with our histological observations of RVFW wet tissue density. In the context of improved RV function and pressures, increased tissue density may indicate a combination of decreased collagen content (fibrosis) and/or recovery of inherent collagen fiber density, although we were only able to detect a nonsignificant trend in RV fibrosis in our histological measurements.

Histological analysis revealed increased fibrosis and transmural re-orientation of collagen and myofibers in PH (Fig. 10a-c). Sac/Val prevented transmural re-orientation of both collagen and myofibers, showing only slight re-orientations at sub-endocardial levels (Fig. 10b-c). Dominant transmural orientation of myofibers (circular mean of transmural orientations) were rotated by ~15.5° towards the longitudinal direction (apex to outflow-tract/base) in PH (Fig. 10d). This was also observed in other studies in a rat model of PH (Hill et al., 2014; Avazmohammadi et al., 2017b, 2019b) and was recently hypothesized to be a mechanism underlying maladaptive RV remodeling (Avazmohammadi et al., 2019a). Although the exact mechanism of fiber re-

orientation in PH remains unknown, one potential mechanism as suggested by others (Avazmohammadi et al., 2019a) is alterations in the biomechanical stimuli in the myofiber niche resulting from increased RV pressures, in addition to RV fiber kinematics due to chamber dilation. A potential pathway to be investigated in future studies is the role of Sac/Val in preventing longitudinal fiber realignment via reduction in RV pressures which may lead to decreased wall stress. Prevention of myofiber reorientation may be an important mechanism of action for drugs targeting the RV.

Despite demonstrating a slight reduction in RV fibrosis (13%) with Sac/Val treatment, this did not reach statistical significance (Fig. 10e). This is interesting in light of the improved hemodynamics and RV tissue biomechanics, which may suggest that Sac/Val is primarily acting on RV myocytes and not collagen or fibroblasts in this model of PH. Previous studies have demonstrated anti-fibrotic effects for Sac/Val in other animal models of PH (Clements et al., 2019) as well as models of LV pressure overload (Burke et al., 2019), LV failure in the setting of aortic valve insufficiency (Maslov et al., 2019a) and LV myocardial infarction (Pfau et al., 2019). Despite a large body of evidence in the literature indicating the anti-fibrotic effects of Sac/Val for the LV, there still exists some controversy (Zannad and Ferreira, 2019; Zile et al., 2019). The observed effects of Sac/Val treatment on RV fibrosis in this study could potentially be due to differences in the pathophysiology (Frangogiannis, 2017) of the RV and LV pressure overload. Further studies looking at RV-specific fibrotic responses to Sac/Val treatment are warranted.

PH resulted in increased RVFW tissue stiffness in both circumferential and longitudinal directions (Fig. 11a), as well as increased fiber-level stiffness of combined collagen and myofiber bundles (Fig. 11b). Also, the intrinsic stiffness of myofibers increased in PH (Fig. 11c). This is consistent with clinical observations of reduced titin phosphorylation and increased RV

cardiomyocyte sarcomere stiffness in patients with pulmonary arterial hypertension (Rain et al., 2013). On the other hand, collagen recruitment strain decreased compared to controls, indicating a possible combination of increased collagen content (fibrosis) and/or alterations in the micro-architecture of collagen fibers (decrease in crimp) in PH (Fig. 11d). Sac/Val resulted in decreased stiffness in both longitudinal and circumferential directions as well as the fiber-level stiffness of combined myo-collagen fiber bundles (Fig. 11a-b). The 61% reduction in intrinsic myofiber stiffness with Sac/Val treatment (Fig. 11c) suggests a possible mechanism at the cardiomyocyte level; one such explanation to explore in future studies may be upregulation of cardiomyocyte titin phosphorylation.

Quantifying the tissue-level stiffness with constitutive modelling revealed increased stiffness in longitudinal and circumferential directions in PH (Fig. 12a), accompanied by collagen and myofiber reorientation towards the longitudinal direction (increased tissue-level longitudinal stiffness out of proportion to the elevation in intrinsic myofiber stiffness). Sac/Val treatment resulted in significantly lower stiffness in both directions (Fig. 12a) and prevented fiber re-orientation.

PH also resulted in increased in-plane coupling of longitudinal and circumferential directions with no significant benefits demonstrated by Sac/Val treatment (Fig. 12a). Previous studies have shown that increased in-plane coupling is an indication of a more anisotropic response resulting from a more clustered fiber alignment (Billiar and Sacks, 2000) or increased collagen-myofiber interactions (Avazmohammadi et al., 2017a). Histological studies of RVFW specimens (Fig. 10b-c) showed increased range of fiber angles from epi-to-endocardium for both PH and Sac/Val cohorts (fiber angle range from Epi→Endo: 60°, 96° and 83° for Control, PH and Sac/Val, respectively). This, together with the observed increase in collagen content, explains the increased

coupling stiffness in Figure 12a. The strain energy maps in Figure 12b demonstrate increased stiffness in PH (less deformations in both longitudinal and circumferential directions are obtained at the same strain energy levels compared to controls), while Sac/Val resulted in similar deformation patterns to controls.

Taken together, the actions of Sac/Val on the RV in PH seem to be a prevention of progressive and maladaptive remodeling that is linked to a prevention of myofiber reorientation, with a preferential effect on RV myocytes (as opposed to fibrosis), including prevention of myofiber stiffening. Thus, this study provides a potential insight into the RV remodeling process in PH, in which progressive pressure overload and increasing wall stress result in alterations of the myocyte contractile apparatus. This, in turn, may lead to progressive myofiber stiffening and fiber angle reorientation, all of which contributes to RV-PA uncoupling and RV failure. Drugs that can have a direct effect on this potential remodeling process of the myocyte contractile apparatus, as Sac/Val may (Iborra-Egea et al., 2017; Trivedi et al., 2018), should be further studied in PH and may provide a unique and highly beneficial therapeutic option.

There are limitations to the experimental and modeling techniques used in this study. The PA banding model of PH results in a myocyte hypertrophy-dominated response as opposed to ECM remodeling and fibrosis (Hill et al., 2014). This model helps us to focus on the RV myocardium in the absence of confounding conditions such as hypoxia or pulmonary circulation disease, as we aimed to study the effects of Sac/Val specifically on RV biomechanics. Other animal models of PH (Bogaard et al., 2009; Clements et al., 2019) might be better suited for studying the fibrotic response of the RV. Moreover, we employed a preventive treatment approach to analyze the effects of Sac/Val on PH in a 3-week period. However, this may not precisely mimic what is observed with regards to clinical presentation of PH in humans. Different treatment windows as

well as treatment scenarios after fully developing PH needs to be further investigated. An isolated angiotensin receptor blocking cohort (Valsartan-only treatment) was not included in the current work, mainly due to the evidence from previous studies (Borgdorff et al., 2013; Andersen et al., 2014; Clements et al., 2019) demonstrating no significant hemodynamic or RV hypertrophy benefits with isolated use of angiotensin II receptor antagonists in PH (which limits the translation of any potential biomechanical benefits from Valsartan-only treatment). Nevertheless, this limits our findings to the effects of combination therapy with Sac/Val (the synergistic effects of angiotensin receptor-neprilysin inhibition) without looking at independent benefits from Valsartan or Sacubitril alone. Paraffin fixation processes for histological analysis may cause artifacts in fiber coherency analysis due to tissue dehydration and shrinkage; however, this will affect all groups studied equally allowing for adequate comparison between groups. Also, here we used a phenomenological constitutive model to analyze the tissue-level biomechanics of RV myocardium. Future studies will employ a structurally-detailed constitutive model, such as in (Avazmohammadi et al., 2017a), to study the effects of transmural fiber architectures and interactions between collagen and myofibers in more detail.

In conclusion, our findings show that Sac/Val may prevent maladaptive RV remodeling in a pressure overload model via amelioration of RV pressure rise, hypertrophy, collagen and myofiber re-orientation as well as RVFW stiffening both at the tissue and myofiber level. Further study of the role of Sac/Val treatment in PH and RV remodeling is warranted.

4.0 Effects of Healthy Aging on Right Ventricular Biomechanics

In this chapter we present our findings on the effects of healthy aging on right ventricular (RV) structure, function, and biomechanical properties. Our study provides insights into how healthy aging modulates RV remodeling and lays the ground for future work to study the age-associated differences in RV response to pressure overload.

4.1 Introduction

Healthy aging is associated with alterations in RV structure and function in subjects with no underlying cardiopulmonary disease (Granath et al., 1964; Innelli et al., 2009; Fiechter et al., 2013; Nakou et al., 2016; D'Andrea et al., 2017). Aging results in pulmonary artery (PA) remodeling (Hosoda et al., 1984; Sicard et al., 2018), increased pulmonary vascular resistance (Granath et al., 1964; Ehrsam et al., 1983) and increased PA systolic pressures (Lam et al., 2009; Kane et al., 2016), leading to RV remodeling (Anversa et al., 1990; Chouabe et al., 2004), altered contraction dynamics (Effron et al., 1987), and decreased RV systolic strains (Chia et al., 2014). Moreover, aging results in diminished RV hypertrophy in response to pressure overload (Kuroha et al., 1991; Chouabe et al., 2004). Age-related differences exist in the 1, 2, and 3-year survival rates of pulmonary hypertension (PH) patients (Hoeper et al., 2013).

In recent years, biomechanical analysis techniques have been employed to better understand the underlying mechanisms of RV remodeling (Hill et al., 2014; Avazmohammadi et al., 2017a, 2019a; Sharifi Kia et al., 2020) and have closely linked RV biomechanics to function

(Jang et al., 2017). Despite the evidence suggesting an association between aging and alterations in RV structure/function and higher prevalence of PH in the elderly (Hoeper and Gibbs, 2014), limited data exist on age-associated differences in RV biomechanics. In this work, we evaluate the effects of healthy aging on RV biomechanical properties.

4.2 Methods

A total of 15 male Sprague-Dawley rats corresponding to young (controls, ≈11 weeks, $n_{Control} = 9$) and old (≈80 weeks, $n_{Aging} = 6$) age groups were studied using the multi-scale biomechanical analysis framework described in chapter 3. An approximately 70 weeks age difference between the control and aging groups was considered sufficient to study the effects of healthy aging on RV structure/function in the absence of pathological events arising with senescence in older animals. Historical data from the study described in chapter 3 was used for the control animals in this work. Figure 13 summarizes the experimental procedures and different analysis techniques used in this work. All animal procedures were approved by University of Pittsburgh's IACUC (protocol# 18113872 and 19126652).

Details of our experimentation/analysis techniques were extensively discussed in chapter 3 (section 3.2 Methods). Briefly, terminal invasive pressure catheterization was performed on both groups, using a Millar™ conductance catheter (Millar Inc., Houston, TX) for the young controls ($n_{Control} = 8$) and a Transonic™ conductance catheter (Transonic Systems Inc., Ithaca, NY) for the aging group ($n_{Aging} = 5$). Open-chest hemodynamic measurements were performed under anesthesia induced via inhalation of isoflurane, while the animals were placed on a heated table (37°C) and monitored using a rectal probe. Pressure data was then analyzed for common RV

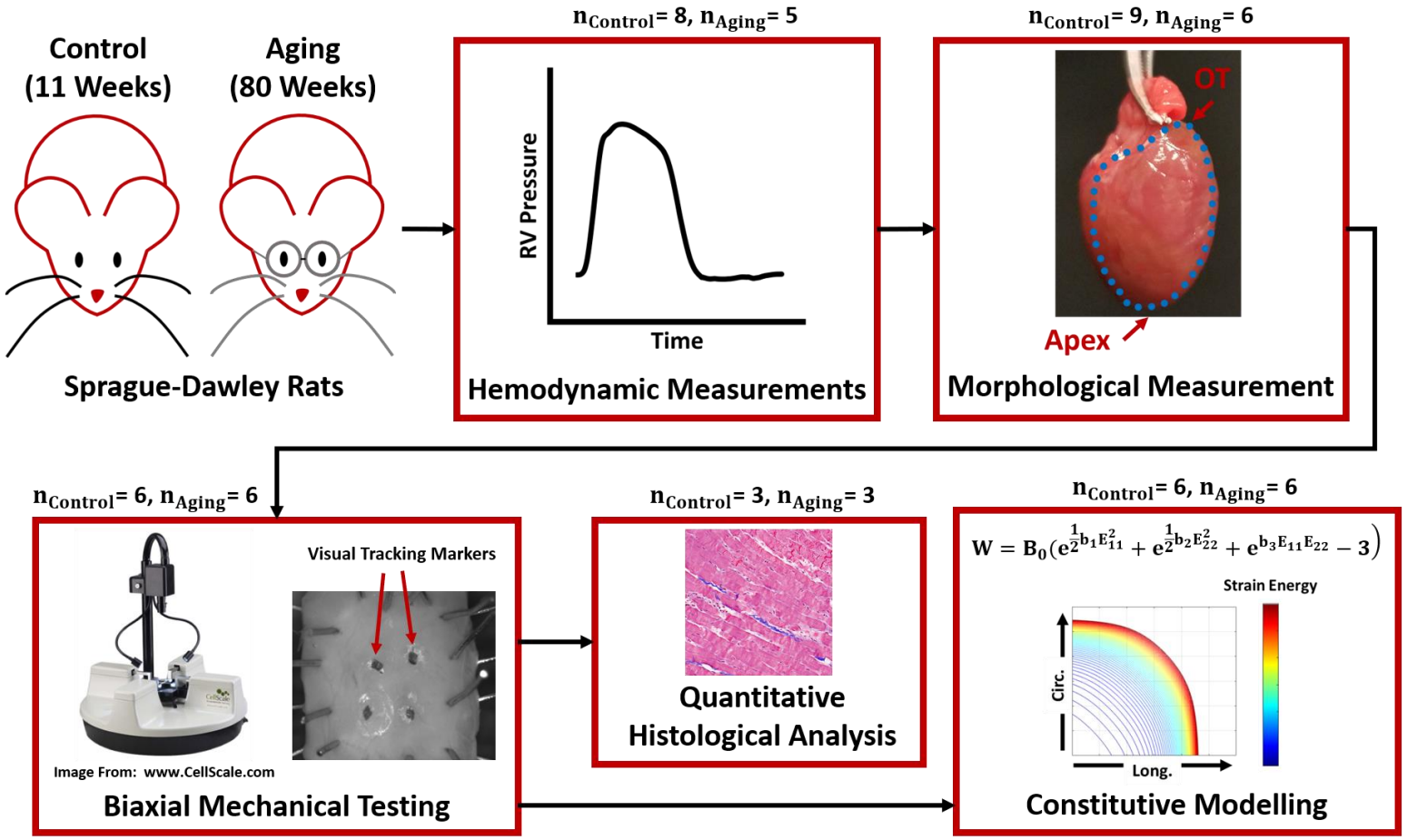

Figure 13 The framework used to study RV remodeling with healthy aging. In-vivo terminal invasive hemodynamic measurements were performed on young controls and aging Sprague-Dawley rats, followed by harvesting the heart and morphological measurements, biaxial mechanical testing, constitutive modeling, and quantitative transmural histological analysis.

hemodynamic metrics, including heart rate, peak pressures and measures of contractility and relaxation. Following hemodynamic measurements, the heart was harvested and measurements were acquired for the Fulton index (ratio of RV mass to mass of the left ventricle + intraventricular septum) and RV free wall (RVFW) thickness ($n_{Control} = 9, n_{Aging} = 6$).

In order to characterize the effects of aging on RV biomechanical properties, following morphological measurements, square specimens were harvested from the RVFW to undergo biaxial testing ($n_{Control} = 6, n_{Aging} = 6$). Specimens were mounted on a BioTester biaxial testing device (CellScale, Waterloo, ON, Canada) in trampoline fashion (using a suture and pulley mechanism) to ensure minimal shear loading (Sacks, 1999). Samples were submerged in modified Krebs solution with 2,3-Butanedione monoxime (BDM) and oxygen to ensure tissue viability (Valdez-Jasso et al., 2012) and underwent multi-protocol biaxial mechanical testing (1:1, 1:2, 2:1, 1:4, 4:1, 1:6, and 6:1 displacement ratios) to investigate the RVFW response in a wide range of possible loading scenarios. Visual tracking markers were placed on the epicardial surface of the RVFW specimens and marker displacements (recorded using a CCD camera) were analyzed to obtain the deformation gradient, Green–Lagrange strain and the 2nd Piola–Kirchhoff stress tensors, using a finite deformation analysis framework in Mathcad (PTC, Needham, MA). Equibiaxial responses of the specimens were interpolated from the multi-protocol test data, using the techniques described in chapter 3. Effective fiber-ensemble (EFE) biomechanical properties of combined collagen and myofiber bundles were then obtained for each specimen, using the equibiaxial response (Sacks, 2003; Hill et al., 2014; Avazmohammadi et al., 2017a; Sharifi Kia et al., 2020). This was then used to estimate the effective myofiber and collagen stiffness for each specimen, using a rule of mixtures approach (Hill et al., 2014; Avazmohammadi et al., 2017a; Sharifi Kia et al., 2020):

$$E_{Myofiber} = \frac{TM_{Before\ Collagen\ Recruitment}}{\Phi_{Myofiber}} \tag{4-1}$$

$$E_{Collagen} = \frac{TM_{After\ Collagen\ Recruitment} - (E_{Myofiber} \times \Phi_{Myofiber})}{\Phi_{Collagen}}$$

Here, $E_{Myofiber}$ and $E_{Collagen}$ are the effective myofiber and collagen stiffness, respectively, while $TM_{Before\ Collagen\ Recruitment}$ and $TM_{After\ Collagen\ Recruitment}$ are the slopes of the lines fitted via linear regression to the fiber-ensemble stress-strain data, before and after collagen recruitment. $\Phi_{Myofiber}$ and $\Phi_{Collagen}$ represent the myofiber and collagen area fractions, measured via histological analysis. As described in chapter 3, we assumed the initial portion of the fiber-ensemble stress-strain responses to be mostly dominated by myofibers, while collagen fibers dominate the high-strain response following collagen recruitment (Hill et al., 2014). Transition strains for categorizing the data before and after collagen recruitment were obtained by differentiating the fiber-ensemble stress-strain response with respect to strain to evaluate the changes in effective fiber-ensemble stiffness (Fata et al., 2014; Hill et al., 2014). The data before the beginning of collagen recruitment was used to evaluate $TM_{Before\ Collagen\ Recruitment}$, while $TM_{After\ Collagen\ Recruitment}$ was estimated using the slope of the line fitted to the linear region of the fiber-ensemble stress-strain data.

Additionally, the constitutive model described in equation 3-8 in chapter 3 (Choi and Vito, 1990) was used to model the response of each specimen. Specimen-specific model parameters were estimated based on the experimental stress-strain data, using a trust-region-reflective nonlinear least-squares optimization algorithm in MATLAB (Mathworks, Natick, MA). A R^2 measure was used to evaluate the goodness of fit. Age-specific strain energy maps were then generated by taking the average of all strain energy distributions, in the circumferential-longitudinal strain space, for RVFW specimens in each age group.

Transmural histological staining was performed on a sub-group of specimens from each group ($n_{Control} = 3, n_{Aging} = 3$) to quantify the effects of aging on RV fiber architecture. Based on our previous work showing minimal between-sample variabilities in RV structure (Hill et al., 2014; Sharifi Kia et al., 2020), a sample size of 3 was considered adequate for statistical analysis of our hypothesis. Specimen fixation was carried out using 10% neutral buffered formalin and RVFW specimens were stained using Masson's trichrome which stains collagen fibers in blue and myofibers in red/pink. A total of 11-17 sections at 50-75 μm increments were obtained for each specimen (from epi to endocardium). Transmural area fractions of collagen and myofibers were then quantified via manual thresholding of the histological images (blue/red) to analyze the effects of aging on RVFW composition. Area fractions were calculated as the ratio of the area occupied by respective blue/red pixels, divided by the total area within the region of interest (ROI). In addition, cardiomyocyte width was measured from the histological data to investigate the role of aging in RV hypertrophy (40 measurements performed on each specimen).

Furthermore, for each histological section, collagen and myofiber orientations were calculated using gradient-based techniques, as described in equation 3-1 in chapter 3. For all data presented in this work, 0° corresponds to the apex to base/outflow-tract (longitudinal) direction, while +90° points towards the circumferential direction, when looking at the RVFW from the epicardial side. Moreover, collagen fiber coherency was evaluated using the formulation described in equation 3-2 in chapter 3. 0% collagen fiber coherency corresponds to a sparse (non-coherent), randomly distributed fiber architecture, while 100% coherency indicates a highly-aligned, tightly packed, continuous (coherent) collagen fiber distribution (Clemons et al., 2018). A total of 66 histological sections were analyzed for the control and aging groups. Transmural data are reported against normalized tissue thickness. We performed linear interpolations to report the histological

data on an equally-spaced grid (0-100% thickness). In case of data categorization (Epi, Mid and Endo groups), the data between 0-20% thickness were used for the epicardium, while the data between 80-100% thickness correspond to the endocardium. Orientation analysis and image segmentation were performed using the OrientationJ toolbox (Rezakhaniha et al., 2012; Püspöki et al., 2016) in ImageJ (imagej.nih.gov).

Data are presented with mean ± standard error of the mean. Sample normality and homogeneity of variance were assessed using the Shapiro–Wilk test and Bartlett's test of homoscedasticity. Circular statistics was employed for analysis of fiber orientation data, using the Watson–Williams test in CircStat toolbox (Berens, 2009) in MATLAB (Mathworks, Natick, MA). For all other data, in case of normality and homoscedasticity, a two-sided unpaired student's t-test was used for statistical comparisons. Welch's t-test was used for non-homoscedastic data, while non-normal distributions were compared using Mann–Whitney U-tests. For all purposes, $p<0.05$ was considered statistically significant. Statistical analyses were performed in the R software package (R Foundation for Statistical Computing, Vienna, Austria).

4.3 Results

4.3.1 RV Hemodynamics and Morphology

Healthy aging did not show an effect on heart rate (Fig. 14a; 271.5±11.7 vs. 292.3±14.1 BPM for Aging-vs.-Control; p=0.326). Aging resulted in increased RV peak pressures (Fig. 14b; 26.8±0.9 vs. 23.0±0.9 mmHg for Aging-vs.-Control; p=0.017), while showing a modest non-significant effect on end-diastolic pressures (Fig. 14c; 1.9±0.4 vs. 1.3±0.1 mmHg for Aging-vs.-Control; p=0.085). Effects of aging on load-dependent measures of RV contractility and relaxation are shown in Figure 14d. Aging significantly increased $\frac{dp}{dt}$max (1611.7±90.5 vs. 1063.8±101.7 mmHg/s for Aging-vs.-Control; p=0.004), but did not demonstrate any effects on $\frac{dp}{dt}$min (-823.9±60.4 vs. -814.7±85.5 mmHg/s for Aging-vs.-Control; p=0.940). Increased contractility index was observed for the aging group (Fig. 14e; 60.1±2.2 vs. 45.8±3.5 1/s for Aging-vs.-Control; p=0.012), while the time constant of RV relaxation (tau) remained unchanged (Fig. 14f; 10.7±1.6 vs. 9.9±0.8 ms for Aging-vs.-Control; p=0.595).

As shown in Table 3, healthy aging significantly increased RV wall thickness (0.89±0.06 vs. 0.66±0.03 mm for Aging-vs.-Control; p=0.002), while not affecting the Fulton index (0.26±0.03 vs. 0.27±0.01 mg/mg for Aging-vs.-Control; p=0.140).

4.3.2 RVFW Biomechanical Properties

Aging demonstrated a bimodal effect on RVFW biaxial properties by resulting in increased circumferential and longitudinal stiffness under lower strains, while progressing to decreased

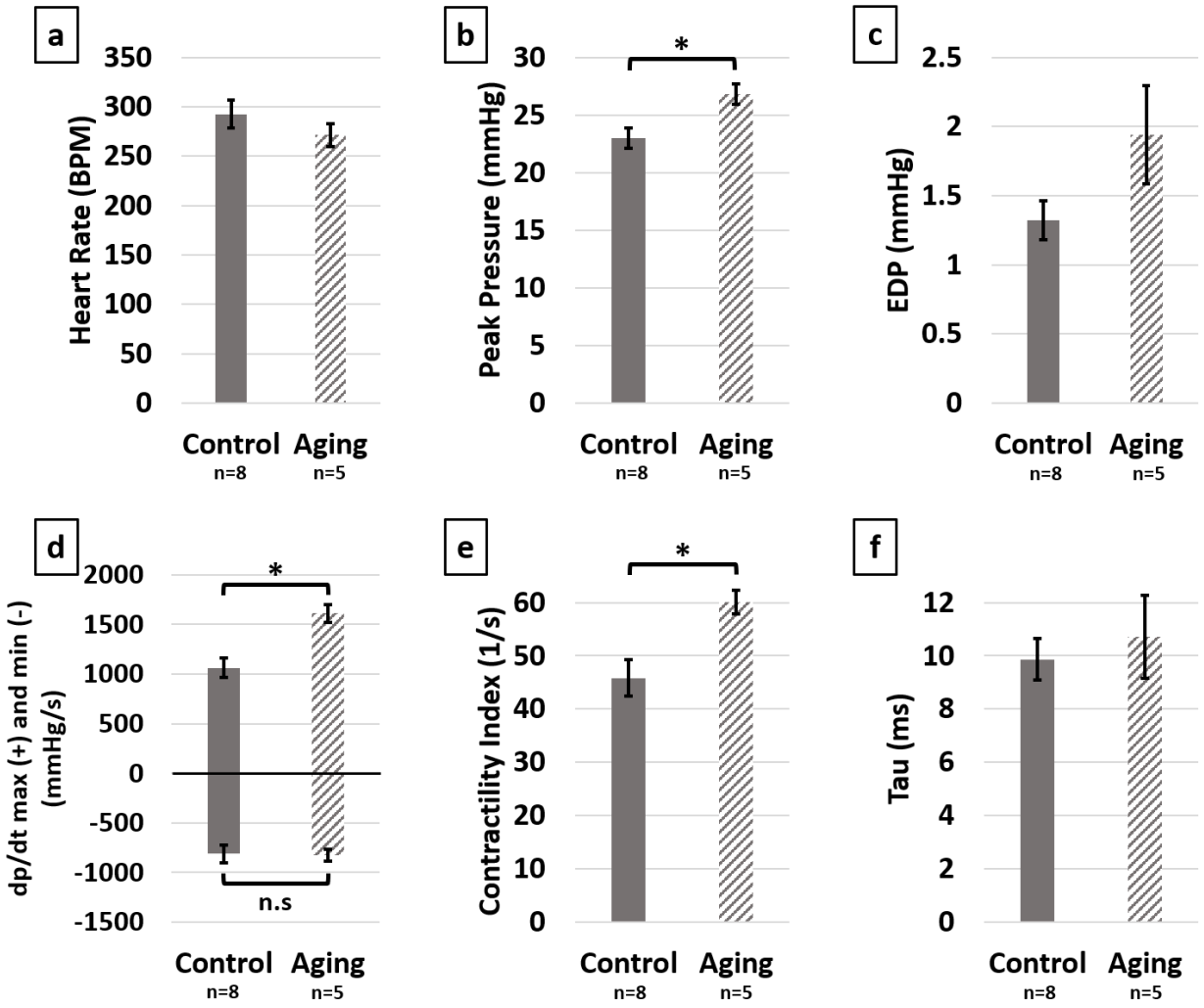

Figure 14 Hemodynamic measures of the effects of healthy aging on RV (a) Heart rate, (b) Peak pressure, (c) End-diastolic pressure, (d) $\frac{dp}{dt}$max (positive side) and $\frac{dp}{dt}$min (negative side), (e) Contractility index and (f) Preload-independent measure of relaxation (tau). Healthy aging significantly increased RV peak pressures and the load-dependent measures of RV contractility ($\frac{dp}{dt}$max and contractility index), while not affecting the heart rate, end-diastolic pressures and relaxation function ($\frac{dp}{dt}$min and tau). Error bars represent standard error of the mean (SEM). * indicates p<0.05. BPM: Beats per minute; EDP: End-diastolic pressure; n.s: Non-significant.

Table 3 Effects of healthy aging on RV hypertrophy (RVFW thickness) and Fulton index

	RVFW Thickness (mm)	Fulton Index (mg/mg)
Control (n=9)	0.66±0.03	0.27±0.01
Aging (n=6)	0.89±0.06	0.26±0.03
p Value	0.002	0.140

biaxial stiffness at higher strains (Fig. 15a). A similar effect was observed on the effective fiber-ensemble stress-strain properties of RVFW collagen and myofibers (Fig. 15b). Using a rule of mixtures approach, this translated into increased effective myofiber stiffness (Fig. 15c; 169.9±20.6 vs. 65.8±4.7 kPa for Aging-vs.-Control; p=0.0006) and decreased effective collagen fiber stiffness (Fig. 15d; 23.9±3.8 vs. 73.1±15.4 MPa for Aging-vs.-Control; p=0.031). Constitutive model parameters for each group are shown in Table 4. Overall, the employed model showed an acceptable fit quality to our experimental data (R^2=0.95±0.01 and 0.96±0.01 for Aging and Control, respectively). Age-specific strain energy maps, representing the combined effects of all model parameters, are demonstrated in Figure 16 for the low-strain and high-strain regions.

Table 4 Constitutive model parameters representing the longitudinal (b_1), circumferential (b_2) and in-plane coupling (b_3) stiffness of RV myocardium for the control and aging groups

	Model Parameters			
	B_0	**b_1 (kPa)**	**b_2 (kPa)**	**b_3 (kPa)**
Control (n=6)	0.173±0.023	98.23±14.52	76.33±7.53	66.72±6.64
Aging (n=6)	0.369±0.082	56.01±7.12	47.35±6.88	43.21±3.80
p Value	0.044	0.026	0.017	0.012

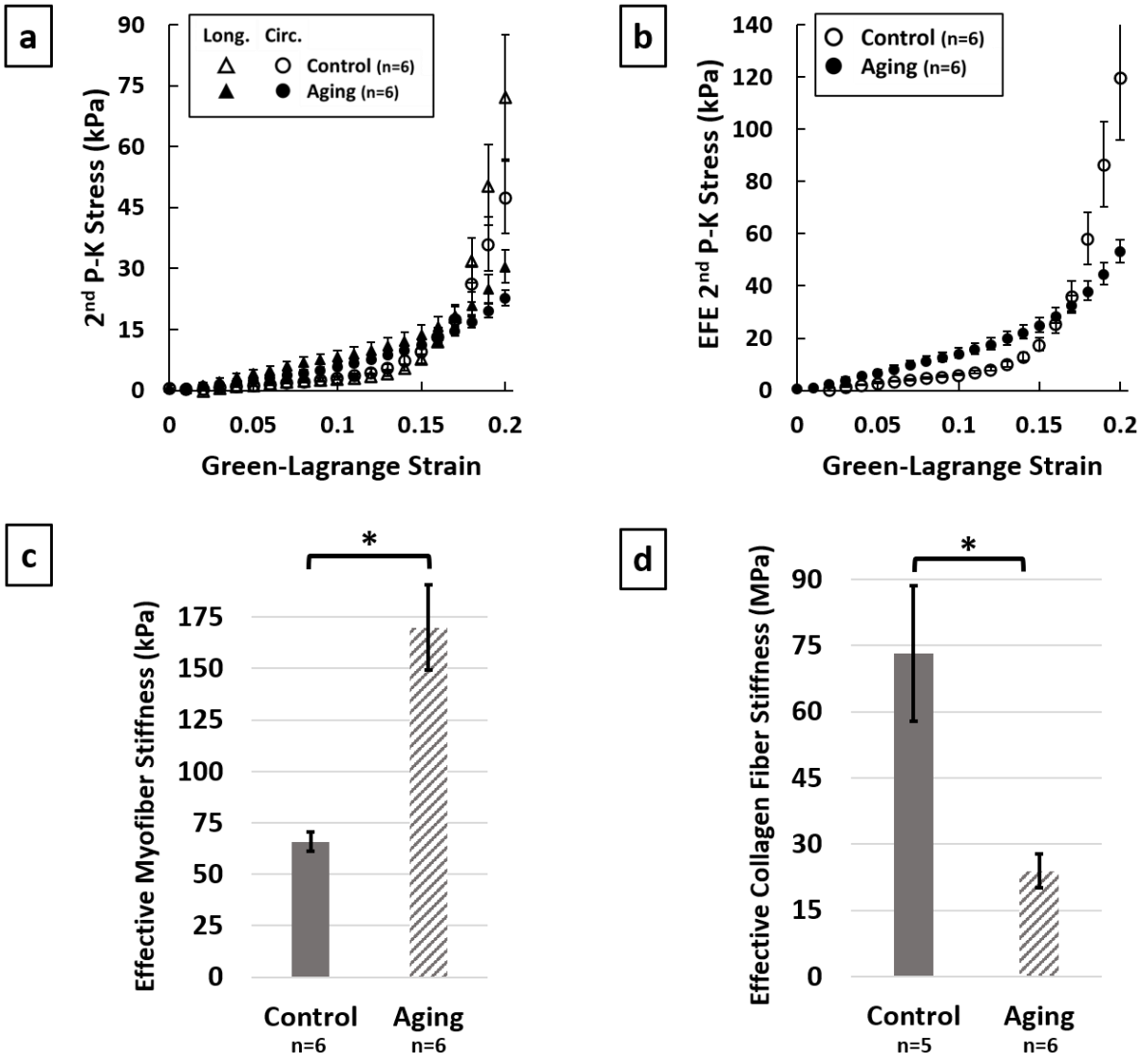

Figure 15 Effects of healthy aging on (a) Biaxial mechanical properties of RV myocardium, (b) Effective fiber-ensemble mechanical properties of combined myofiber-collagen bundles, (c) Effective myofiber stiffness, and (d) Effective collagen fiber stiffness. Healthy aging modulates the biomechanical properties of RVFW in a bimodal manner by increasing the effective myofiber stiffness while decreasing collagen fiber stiffness. Error bars represent standard error of the mean (SEM).* indicates $p<0.05$. EFE 2nd P-K Stress: Effective fiber-ensemble 2nd Piola-Kirchhoff stress.

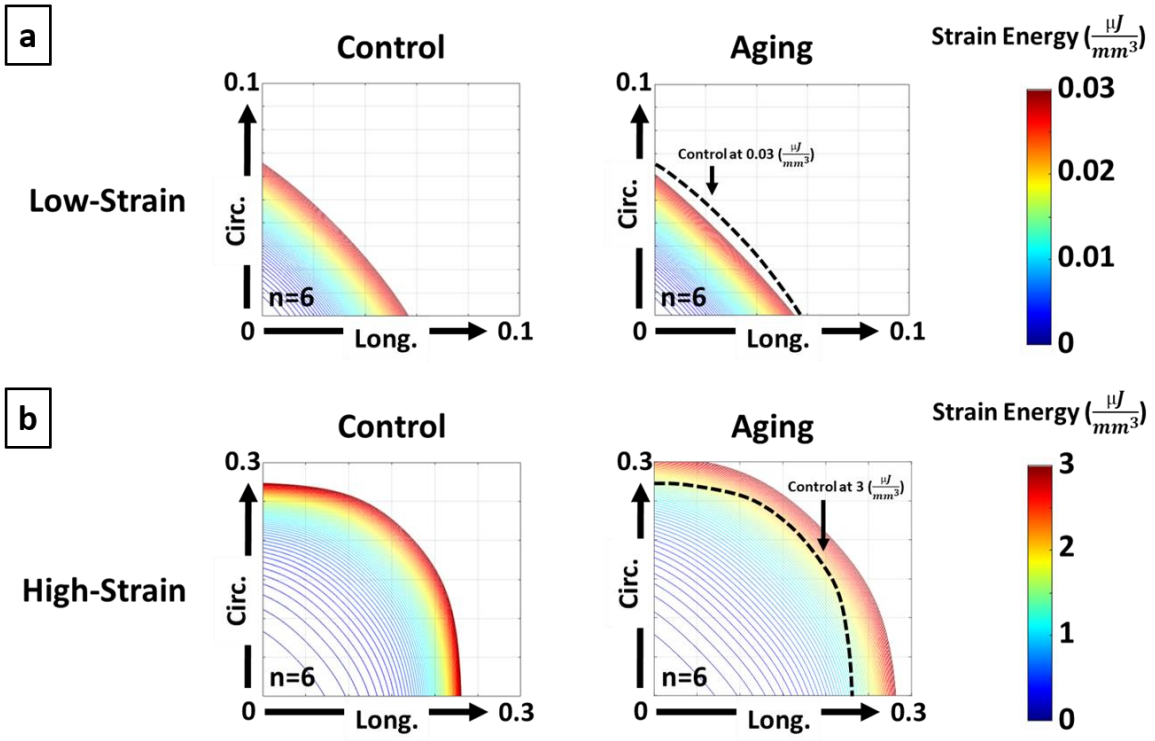

Figure 16 Strain energy maps of RVFW in (a) the low-strain region (circumferential-longitudinal strain space) and (b) the high-strain region. Strain energy maps demonstrate increased RVFW stiffness in the low-strain region with healthy aging (mostly dominated by myofibers), followed by decreased RVFW stiffness in the high-strain region post-collagen recruitment.

4.3.3 Quantitative Transmural Histology

Representative histological sections are demonstrated for each group in Figure 17a . Aging resulted in increased cardiomyocyte width (Fig. 17b; 25.42±0.34 vs. 14.94±0.64 μm for Aging-vs.-Control; p=0.0001). Quantifying the transmural orientation of RVFW fibers revealed myofiber (Fig. 17c) and collagen (Fig. 17d) reorientation at sub-endocardial levels. Overall, myofibers showed similar orientations to collagen fibers. Aging significantly shifted the overall orientation of myofibers (circular mean of transmural distributions, dotted lines in Fig. 17c) by 14.6° towards the longitudinal direction (Fig. 17e; p=0.017). Similarly, the dominant orientation of collagen

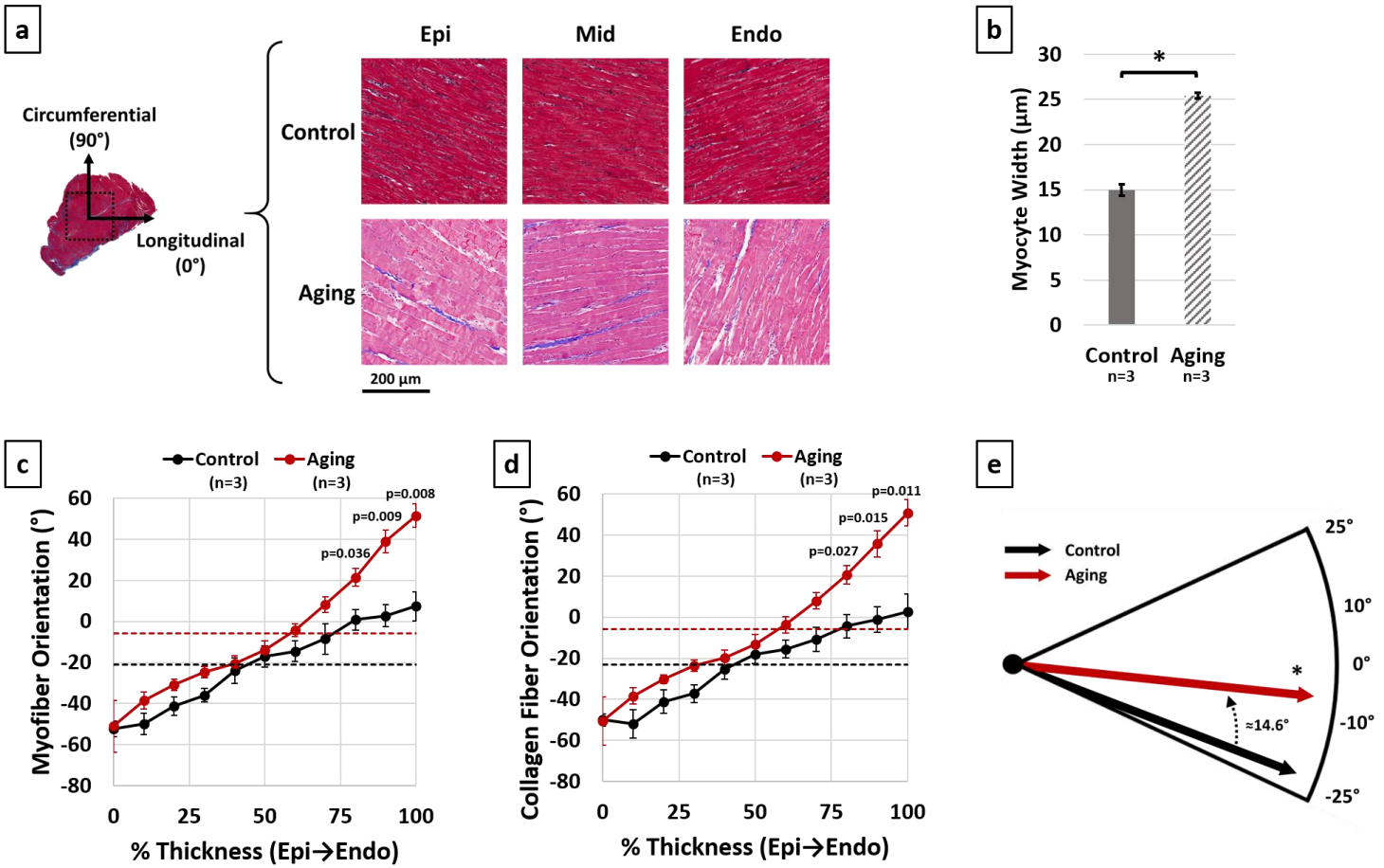

Figure 17 Histological analysis of the effects of healthy aging on RV structure. (a) Representative transmural histological sections of the RVFW (Red/Pink: Myofiber, Blue: Collagen) and effects of aging on (b) Cardiomyocyte hypertrophy (myocyte width), (c) Transmural myofiber orientations, (d) Transmural collagen fiber orientations, and (e) Dominant myofiber orientations. Healthy aging results in cardiomyocyte hypertrophy, in addition to reorientation of sub-endocardial collagen and myofibers. Error bars represent standard error of the mean (SEM). * indicates p<0.05.

fibers was shifted by 16.4° (p=0.013). Aging also resulted in cardiomyocyte loss and decreased myofiber area fractions at both epicardium (Fig. 18a; 90.8±0.3% vs. 95.3±0.7% for Aging-vs.-Control; p=0.004) and endocardium (Fig. 18a; 82.4±1.5% vs. 95.3±1.9% for Aging-vs.-Control; p=0.007), with a non-significant effect on the mid-ventricular region (Fig. 18a; 91.8±1.3% vs. 95.4±0.5% for Aging-vs.-Control; p=0.063). Furthermore, aging lead to RVFW fibrosis and increased collagen area fractions at epicardium (Fig. 18b; 5.3±0.4% vs. 3.4±0.3% for Aging-vs.-Control; p=0.015) and the mid-ventricular region (Fig. 18b; 5.0±0.4% vs. 3.4±0.3% for Aging-vs.-Control; p=0.037). Analyzing the coherency of collagen architectures revealed decreased coherency at the endocardium (Fig. 18c; 10.4±1.1% vs. 19.7±1.1% for Aging-vs.-Control; p=0.003), while not showing any effects on other transmural regions.

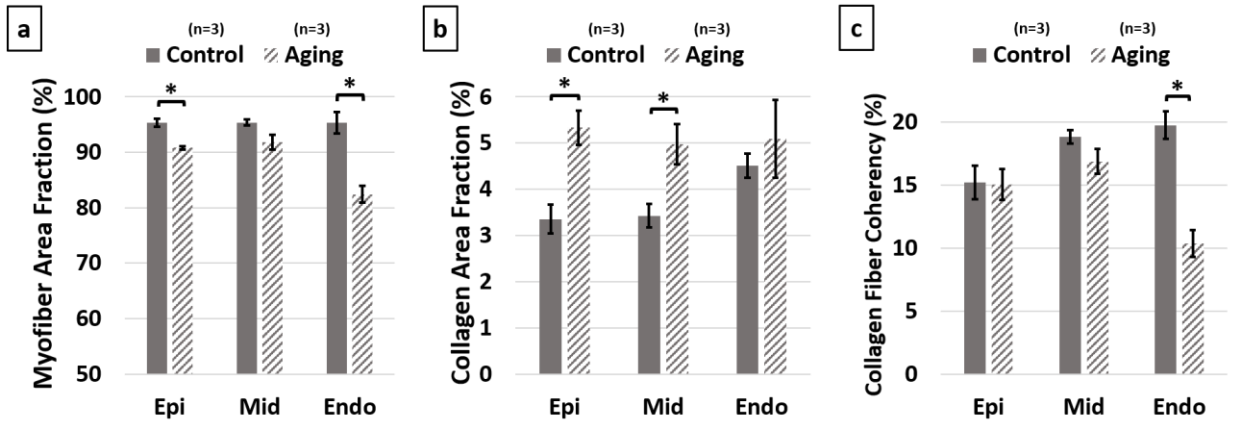

Figure 18 Histological analysis of the effects of healthy aging on (a) Transmural myofiber content (area fraction), (b) Transmural collagen content (area fraction), and (c) Transmural collagen fiber coherency. Healthy aging leads to loss of cardiomyocytes, RVFW fibrosis and decreased collagen fiber coherency at endocardium. Error bars represent standard error of the mean (SEM). * indicates p<0.05. Epi: Epicardium; Mid: Mid-ventricular region; Endo: Endocardium.

4.4 Discussion and Conclusions

We aimed to investigate the effects of healthy aging on RV remodeling. Aging resulted in 1) Increased peak pressures (≈↑17%) and RV contractility (≈↑52%); 2) Increased RVFW thickness (≈↑34%) with no effects on the Fulton index, indicating proportional right and left ventricular growth; 3) Longitudinal reorientation of collagen/myofibers, together with cardiomyocyte loss and RVFW fibrosis with decreased collagen fiber coherency; 4) Increased effective myofiber stiffness (≈↑158%) accompanied by decreased collagen fiber stiffness (≈↓67%).

The observed increase in RV peak pressures (Fig. 14b) is consistent with previous reports of increased PA systolic pressures and RV afterload with healthy aging (Lam et al., 2009; Kane et al., 2016). Furthermore, cardiomyocyte width (Fig. 17b) and RVFW thickness (Table 3) increased with aging, leading to increased organ-level contractility (Fig. 14d-e). This is similar to previous observations of RV hypertrophy in PH and increased contractility to overcome the elevated afterload (Hill et al., 2014; Sharifi Kia et al., 2020).

Histological analyses revealed reorientation of endocardial collagen and myofibers, resulting in a longitudinal shift in dominant transmural orientation of RVFW fibers (Fig. 17e). Similar patterns of fiber reorientation were noted in animal models of PH (Avazmohammadi et al., 2017b; Sharifi Kia et al., 2020). Consistent with prior work (Anversa et al., 1990; Walker et al., 2006), cardiomyocyte loss (Fig. 18a) and RVFW fibrosis (Fig. 18b) were noted due to aging. Cardiomyocyte loss in the RVFW increases the hemodynamic load on the remaining myocytes (Fajemiroye et al., 2018) and may explain the observed hypertrophy patterns (Fig. 17b). While requiring further experimentation, a potential explanation for RV myocyte loss and extracellular matrix (ECM) deposition may be local RVFW ischemia due to aging (Anversa et al., 1990).

Fiber reorientation (Fig. 17c-d) and increased transmural change in fiber angles, lead to a less anisotropic biaxial mechanical response for the aging group (Fig. 15a). Bimodal alterations in RVFW biaxial properties were observed with aging (Fig. 15a). Compared to controls, the aging group showed higher stiffness in the low-strain region, followed by lower biaxial stiffness at higher strains. Moreover, aging lead to increased effective myofiber stiffness (Fig. 15c). Increased myofiber stiffness and reduced tissue-level ventricular stiffness at high strains have been previously documented in separate studies on age-related left ventricular remodeling (Cappelli et al., 1984; Lieber et al., 2004). Potential underlying mechanisms of increased myofiber stiffness include myocyte remodeling due to cell loss, as well as reduced titin phosphorylation (Rain et al., 2013). Despite an increase in collagen area fractions (Fig. 18b), effective collagen fiber stiffness decreased with aging (Fig. 15d). In this study, collagen stiffness measures represent the effective response of collagen fibers, estimated from the tissue-level behavior. Therefore, while this could indicate a decrease in the intrinsic stiffness of collagen fibers, it does not eliminate the possibility of tissue-level structure/architecture affecting the observed behavior (Hill et al., 2014). For instance, reduced collagen fiber coherency was detected at the endocardial levels (Fig 18c), indicating a more sparse and isotropic distribution of collagen fibers in the aging group (Clemons et al., 2018). This has the potential to affect the load transfer mechanism of endocardial collagen fibers, contributing to reduced effective modulus at the tissue level. Further experimentation is warranted on the mechanisms of collagen fiber remodeling with aging. Candidate mechanisms for decreased effective collagen stiffness include 1) Lysyl oxidase-mediated alterations in collagen cross-linking, 2) Reduced effective collagen stiffness due to myocyte loss and altered biomechanics in the collagen/myofiber niche, hampering effective load transfer in the RVFW continuum, 3) Altered collagen microstructure/crimp, resulting in delayed collagen recruitment.

Age-specific strain energy maps were employed to investigate the effects of healthy aging on RV biomechanical properties. Model predictions demonstrate a similar bimodal strain energy response to experimentally measured data, indicating increased stiffness in the low-strain region, followed by decreased stiffness at higher strains (Fig. 16).

Despite low variability and strong statistics, the small sample size of our preliminary study remains a limitation. Moreover, lack of volumetric hemodynamic data prevents analyzing the effects of aging on in-vivo RV structure. Additionally, we employed a phenomenological constitutive model for analyzing our biomechanical data. Future work will focus on structurally-informed constitutive models of RV myocardium (Avazmohammadi et al., 2017a) to couple the histologically measured tissue architecture with biaxial properties. Different batches of staining solution used for each group, resulted in different shades of cardiomyocyte staining for control vs. aging (red vs. pink). However, this will have minimal effects on our findings since segmentation thresholds for myofibers and collagen were individually selected for each histological section.

In summary, our results demonstrate the potential of healthy aging to modulate RV remodeling via increased peak pressures, cardiomyocyte loss, fibrosis, fiber reorientation and altered collagen/myofiber stiffness. Similarities were observed between aging-induced remodeling patterns and RV remodeling in PH.

5.0 Assessment of Stretch-Induced Transmural Myocardial Fiber Kinematics in Right Ventricular Pressure Overload

In this chapter, we present our efforts towards the development of a high-frequency ultrasound imaging framework, in addition to structurally-informed finite element (FE) models of the right ventricular free wall (RVFW), in order to evaluate the stretch-induced kinematics of right ventricular (RV) fibers.

5.1 Introduction

Transmural myocardial fiber orientations in the RVFW lead to unique structural and biomechanical properties and play a key role in RV function. Pulmonary hypertension (PH) is a disease that results in RV pressure overload, ventricular remodeling, myocardial hypertrophy and fibrosis. RV failure remains the main cause of mortality in the setting of PH (Voelke et al., 2011) with 3-year mortality rates as high as 33-38% (Benza et al., 2007; Humbert et al., 2010).

Previous studies have closely linked RV biomechanics to ventricular function (Jang et al., 2017). From a biomechanical perspective, RV myocardium experiences increased wall thickness, tissue stiffening, fibrosis, chamber dilation and transmural fiber reorientation in PH (Hill et al., 2014; Sharifi Kia et al., 2020). RV remodeling and fiber reorientation towards the longitudinal (apex to base/outflow-tract) direction results in drastically different RV biomechanics, affecting the transmural distribution of wall stress (Carruth et al., 2016), ventricular twisting motions, and filling and ejection mechanics of the RV (Avazmohammadi et al., 2019a). Nevertheless,

mechanistically, RV fiber reorientation is poorly understood and there remains a debate around the adaptive (Gomez et al., 2017) vs. maladaptive (Avazmohammadi et al., 2019a) nature of fiber remodeling in PH. Characterizing the kinematics of myocardial fibers will help establishing a better understanding of the underlying mechanisms of fiber realignment in PH. However, full-thickness transmural RV fiber kinematics remains largely unexplored, mainly due to imaging difficulties caused by the RV wall thickness in large animal models and human patients, limiting our ability to study fiber kinematics transmurally. Despite high imaging resolutions, the 100-1200 μm depth limit of optical techniques such as multi-photon microscopy (Sommer et al., 2015), and long imaging time, exposure to ionizing radiation, availability and cost-effectiveness issues with diffusion tensor magnetic resonance imaging (DT-MRI) (Ferreira et al., 2014; Agger et al., 2017) limit their applicability for benchtop or clinical studies on RV fiber kinematics. On the other hand, ultrasound imaging is a widely available, non-ionizing, cost-effective technique capable of overcoming the depth limits of optical methods to assess cardiac structure and function.

RV myocardium undergoes different modes of deformation during a cardiac cycle (Fig. 19). In the current work we focus on the stretch-induced deformations of RVFW during diastolic filling and the isovolumic contraction (IVC) phase of early-systole (Fig. 19). IVC follows tricuspid valve closure at end-diastole, when active myocardial contraction increases chamber pressures (while both tricuspid and pulmonary valves remain closed) which results in increased wall stress (afterload) and stretching of the RVFW. Both active contraction and passive stretching happen simultaneously during early-systole, as reflected in increased ventricular pressures (Tsamis et al., 2011; Hill et al., 2014), demonstrating active contraction, in addition to fiber stretch (Tsamis et al., 2011) and ventricular wall thinning (Guntheroth, 1974; Tsamis et al., 2011), demonstrating stretch-induced deformations. This is followed by pulmonary valve opening and systolic ejection.

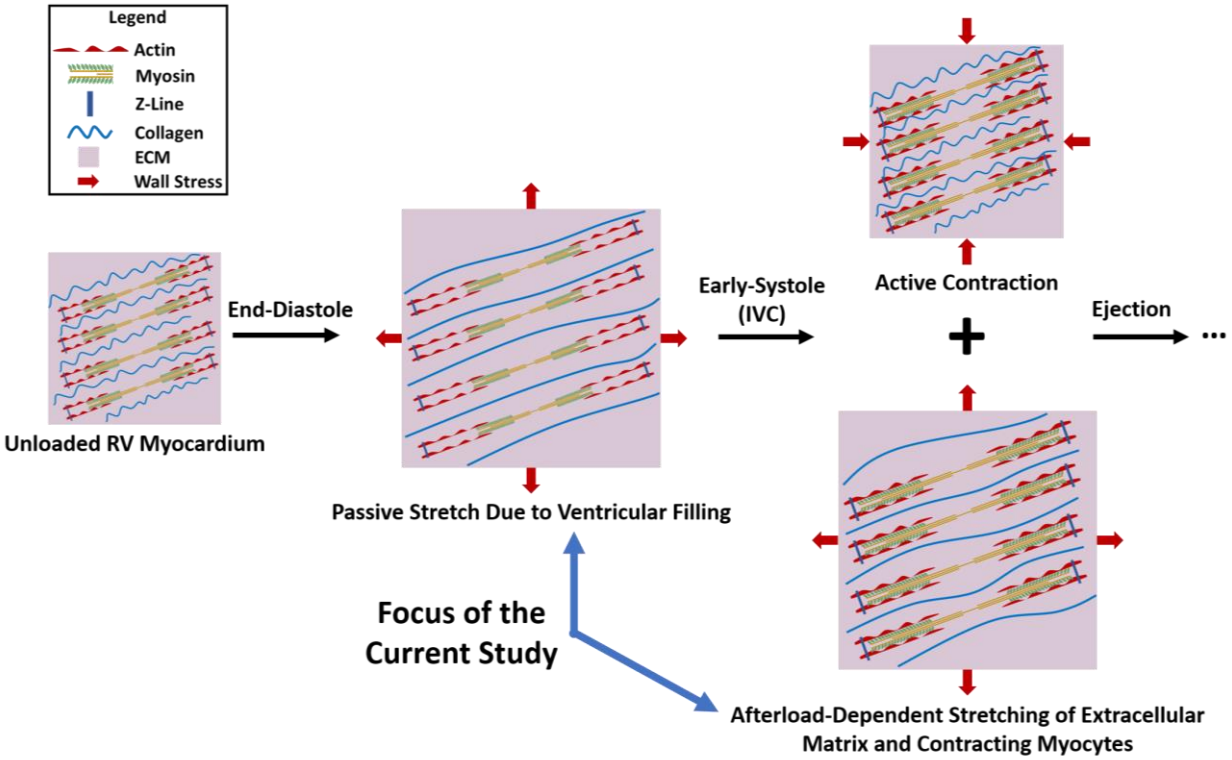

Figure 19 Stretch-induced deformations experienced by RV myocardium during diastolic filling and the isovolumic contraction (IVC) phase of early-systole. During diastole, ventricular filling results in passive stretch of the RVFW. IVC follows tricuspid valve closure at end-diastole, during which active myocardial contraction increases chamber pressures (while both tricuspid and pulmonary valves remain closed) and results in increased wall stress (afterload) and stretching of the RVFW. Both active contraction and stretching happen simultaneously during this phase, as reflected in increased ventricular pressures, in addition to ventricular wall thinning, and fiber stretch during early-systole. This is followed by pulmonary valve opening and systolic ejection, which results in negative RVFW contractile strains. The current study focuses on stretch-induced deformations of RV myocardium during the end-diastolic and early-systolic phases of a cardiac cycle, without considering the effects of cardiomyocyte contraction.

Myocardial contraction (fiber shortening) results in small reversible changes in fiber angles towards the longitudinal direction (Streeter and Hanna, 1973; Omann et al., 2019), as also reflected in the torsional motion of the heart (Ashikaga et al., 2009). However, longitudinal fiber remodeling in PH has been identified as an end-stage remodeling event (Hill et al., 2014; Avazmohammadi et al., 2019a; Sharifi Kia et al., 2020) accompanied by reduced RV ejection fraction (Avazmohammadi et al., 2019a) and diminished systolic myofiber shortening (Voeller et al., 2011). While the eventual outcome of fiber remodeling may affect ventricular contractile mechanics (Bovendeerd et al., 1999; Kroon et al., 2009), decreased myofiber shortening (minimum principle strains) at end-stage PH (Voeller et al., 2011) results in smaller active myofiber kinematic shifts towards the longitudinal direction compared to normotensive loading and makes myofiber contraction less likely to mechanistically stimulate transmural fiber reorientation in PH. Motivated by this, we hypothesized that stretch-induced deformations experienced by RV myocardium (Fig. 19) in the setting of PH may result in myofiber kinematic shifts towards the longitudinal direction. Stretch-induced deformations have been previously studied as a stimuli for fiber reorientation in other biological tissues (Wilson et al., 2006; Driessen et al., 2008).

Stretching of the myocardial niche in early-systole is of particular importance in the setting of pressure overload, mainly due to the increased afterload (wall stress). Previous studies have reported an increase in stretch-activated Ca^{2+} transient amplitudes in response to pressure overload, with no significant alterations in the diastolic sarcomere length (Rouhana et al., 2019). Additionally, expressions of stretch-induced c-fos proto-oncogenes (Komuro et al., 1990) and fetal isoforms of α-actin have been identified as an early growth-induction response in pressure overload (Izumo et al., 1988). Increased early-systolic stretch is also evident in echocardiographic assessments of patients with increased RV afterload (Schupp et al., 2007). Due to material

anisotropy and nonlinearity (Valdez-Jasso et al., 2012; Hill et al., 2014; Avazmohammadi et al., 2017a; Sharifi Kia et al., 2020), depending on the ratio of the applied mechanical stimuli (strain), stretching of RV myocardium may lead to fiber kinematics towards different directions under different loading scenarios (Fig. 20). Stretch-induced alterations in the biomechanical stimuli applied to the myofiber niche has the potential to activate different remodeling pathways leading to fiber realignment and structural remodeling (Yoshigi et al., 2003; Nguyen et al., 2009; De Jong et al., 2011; Hoffman et al., 2012).

In the first stage of this study, an enhanced framework was developed and validated against histological measurements to analyze high-frequency ultrasound (HFU) images for quantification of transmural RV myofiber orientations. Stretch-induced myofiber reorientation under uniaxial loading was studied to demonstrate the feasibility of the developed framework to study RV fiber kinematics. Furthermore, due to the complexity associated with coupled biaxial loading/HFU imaging, nonlinear structurally-informed fiber embedded FE models of the RV myocardium were developed to conduct an exploratory study on biaxial fiber kinematics. FE models were used to study the role of different remodeling events such as fibrosis (Hill et al., 2014; Sharifi Kia et al., 2020), concentric (Guerreiro et al., 1988; Hill et al., 2014; Sharifi Kia et al., 2020) and eccentric (Tezuka et al., 1990; Hill et al., 2014) hypertrophy in stretch-induced RV fiber kinematics in acute and chronic pressure overload. Our exploratory study improves the current understanding of the role of different remodeling events involved in transmural reorientation of RV fibers in PH. This will help with appropriate hypothesis generation for future experimental studies on RV fiber kinematics, while ongoing work focuses on development of improved imaging algorithms for coupled HFU imaging/biaxial loading.

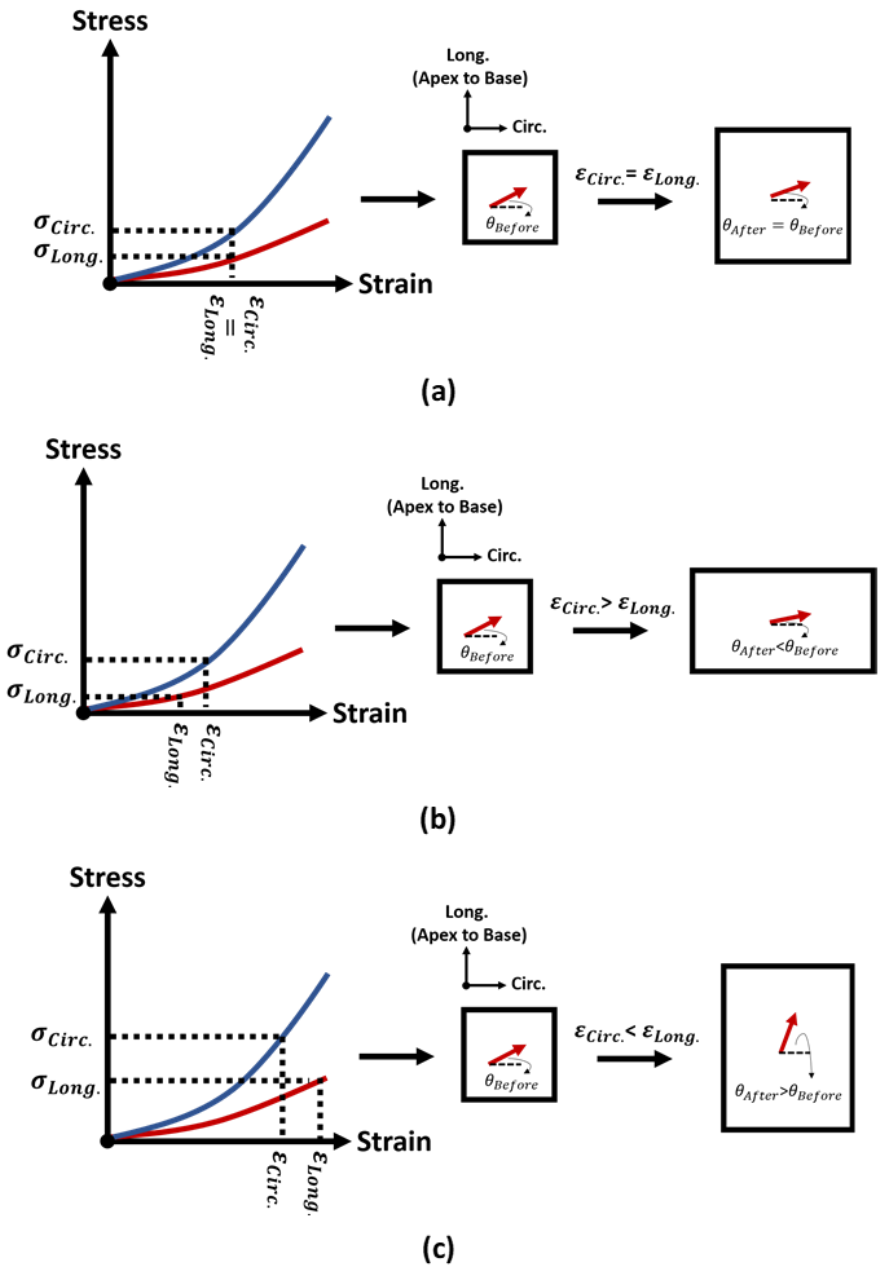

Figure 20 Conceptual demonstration of the effects of biaxial loading conditions on the deformation state and fiber kinematics of RV myocardium. Hypothetical loading scenarios resulting in (a) equibiaxial strain with no fiber rotations, as well as scenarios with kinematic shift of fibers towards the (b) circumferential and (c) longitudinal directions. Material nonlinearity and anisotropy of RV myocardium results in different fiber kinematics at different stress levels. While some scenarios may result in equibiaxial strain conditions with no fiber kinematics, others may lead to $\varepsilon_{Circ.} > \varepsilon_{Long.}$ or $\varepsilon_{Circ.} < \varepsilon_{Long.}$, resulting in clockwise or counterclockwise fiber kinematics, respectively.

5.2 Methods

5.2.1 HFU Imaging to Quantify Transmural RV Fiber Kinematics

Previous studies have demonstrated the potential of HFU imaging in characterizing muscle fibers with high spatial resolution, using a combination of multi-scale decomposition and diffusion filtering techniques (Qin et al., 2013; Qin and Fei, 2014). However, to the best of our knowledge, no efforts have been made to quantify the transmural kinematics of RV myofibers using HFU imaging. In the first stage of this work, an enhanced HFU imaging framework was developed to study the transmural kinematics of RVFW myofibers (Fig. 21).

5.2.1.1 Development of an HFU Imaging Framework

A square specimen was harvested from the basal anterior zone-also known as the r2 zone (Agger et al., 2017)-of porcine RVFW (procured from a local butchery) and scanned at 50 MHz using an HFU scanner (Vevo2100, FUJIFILM-VisualSonics, Toronto, Canada). HFU images were acquired at a precision of 524 pixels/cm while the imaging probe was positioned along the apex to base direction, normal to the transmural axis of the RVFW (from epicardium to endocardium). Using a servo stage, 3D scans were generated by stacks of 2D images acquired at 102 μm increments, chosen based on the transducer elevational beam width. Since HFU scans result in high noise in the acquired images, as shown in Figure 21, similar to previous studies (Qin and Fei, 2014), a nonlinear anisotropic diffusion filter (NLADF) was used to reduce the noise levels (Perona and Malik, 1990):

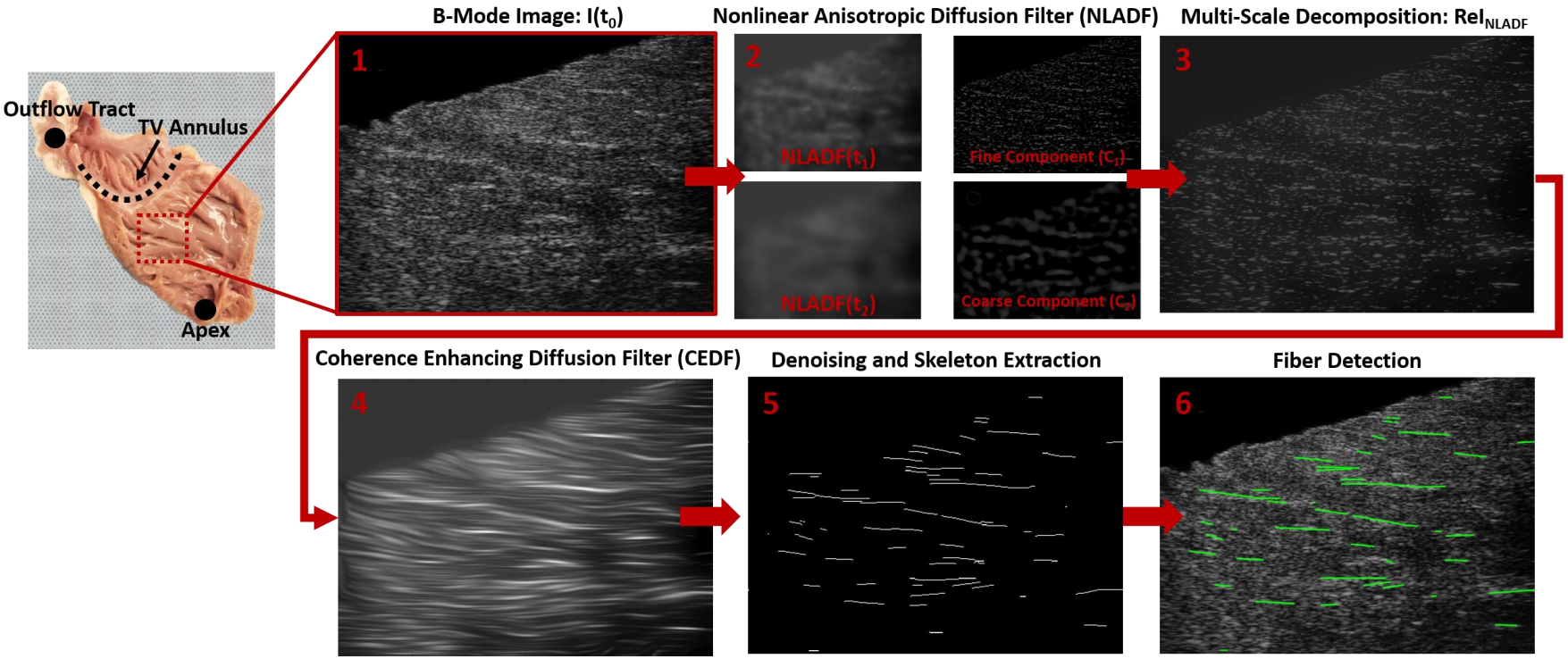

Figure 21 The ultrasound image processing framework used to detect transmural RV myofiber orientations. Basal anterior zone RVFW specimens were scanned while the ultrasound probe was aligned with the apex-to-base direction, normal to the transmural axis. High noise in the acquired high-frequency B-mode images were reduced via multi-scale decomposition using NLADF, followed by establishing myofiber connectivity by CEDF. Skeleton extraction was performed on the resulting image, followed by fiber detection using the Hough transform and fitting a normal probability density function (PDF) to the fiber distributions.

$$\frac{\partial I}{\partial t} = \nabla.(c(x,y,t)\nabla I) = c(x,y,t)\Delta I + \nabla c\,.\,\nabla I \tag{5-1}$$

Here, I is the image intensity in 2D space, t represents the iteration steps and c is the anisotropic diffusion tensor at point (x,y), as previously defined (Qin et al., 2013; Qin and Fei, 2014). The NLADF filtering framework is based on the diffusion equation, and helps reducing the noise levels via directional gaussian blurring (Perona and Malik, 1990), while keeping the main features of the image. The acquired B-mode images were filtered using equation 5-1 at two different iterations, NLADF(t_1) and NLADF(t_2), while $t_2 > t_1$. Appropriate iteration times (t_1 and t_2) were manually selected by observing noise reduction in the denoised images produced by NLADF (t_1 =100 and t_2=300 iterations for the purposes of this study). This was followed by multi-scale decomposition of fine and coarse components of the image (Fig. 21):

$$C_1 = I(t_0) - \text{NLADF}(t_1) \tag{5-2}$$

$$C_2 = \text{NLADF}(t_1) - \text{NLADF}(t_2) \tag{5-3}$$

$$\text{ReI}_{\text{NLADF}} = \alpha_1 C_1 + \alpha_2 C_2 + (1 - \alpha_1 - \alpha_2)\text{NLADF}(t_2) \tag{5-4}$$

Where $I(t_0)$ is the original B-mode image, C_1 is the fine component of the HFU image, C_2 is the coarse component, $\text{ReI}_{\text{NLADF}}$ is the reconstructed image following NLADF and multi-scale decomposition, and α_1 and α_2 are the scaling gains for image reconstruction (Fig. 21). $\text{ReI}_{\text{NLADF}}$ helps boosting the fine components in the HFU image, while keeping the main features. Similar to previous work (Qin and Fei, 2014), α_1 and α_2 were set at 0.6 and 0.2, respectively.

Despite considerably reduced noise levels after the NLADF, high noise in the original image leads to myofibers represented in interrupted segments (Fig. 21). Therefore, a coherence enhancing diffusion filter (CEDF) was used to establish connectivity between disconnected fiber segments (Weickert, 1999), while preserving the orientation of features in the original B-mode image (Fig. 21). CEDF functions similar to the NLADF algorithm (equation 5-1) while the diffusion tensor c(x,y,t) is replaced by an adaptive structure tensor constructed using localized image orientations (Weickert, 1999; Qin and Fei, 2014). This helps completing disconnected segments while keeping the orientation of features in the original image (Fig. 21). Following each filtering step, the resulting image was denoised via threshold-based techniques (Qin and Fei, 2014). Appropriate denoising thresholds were manually selected for each image. Finally, the resulting image was converted to a binary format and, subsequent to skeleton extraction, myofiber orientations were detected using the Hough transform (Fig. 21). A Gaussian probability density function (PDF) was then fitted to the fiber distributions at each section throughout the RV wall to quantify transmural fiber orientations. Distribution means were reported as the dominant orientation at each transmural section, while standard deviation of the distributions represents the fiber spread/dispersion (Thunes et al., 2016). Algorithm development was performed using MATLAB (Mathworks, Natick, MA).

5.2.1.2 Algorithm Validation with Histological Measurements

For technical validation purposes, HFU measurements were compared with transmural histological staining of the RVFW specimen using a hematoxylin and eosin (H&E) stain. Fiber orientations of histological sections were detected using local image gradients, as described in equation 3-1 in chapter 3. Image processing and fiber orientation analysis of histological sections were performed using the OrientationJ toolbox (Rezakhaniha et al., 2012; Püspöki et al., 2016) in

ImageJ (imagej.nih.gov). Similar to previous studies (Vetter et al., 2005), for algorithm validation and comparison purposes, fiber angles measured via histology and HFU imaging were normalized to 0° at the epicardial layer to better demonstrate the transmural change in fiber angles and eliminate any tissue alignment mismatch between HFU and histological measurements.

5.2.1.3 Feasibility Evaluation of the Developed Framework to Study the Transmural Kinematics of RV Myofibers Under Uniaxial Loading

Following algorithm verification, RVFW specimens (n=3) were harvested from the basal anterior zone of porcine myocardium and loaded using a custom displacement-controlled uniaxial loading gripper that allows real-time HFU imaging (Fig. 22). Fiber orientations were measured and analyzed in the RV circumferential-longitudinal coordinate system when apex-to-base denotes the longitudinal direction. Transmural fiber orientations were then analyzed under a stretch ratio (λ) of 1.35 in the circumferential direction. This was chosen based on a RV systolic pressure of ≈105 mmHg in PH (Tezuka et al., 1990) and approximation of RVFW stretch based on previously reported biomechanical properties for a porcine model (Nemavhola, 2017). Experimentally measured fiber kinematics were compared with theoretical predictions for an incompressible transversely isotropic solid with affine kinematics (Guerin and Elliott, 2006):

$$\Theta_{\text{Loaded}} = \arctan\left(\frac{\text{Sin}(\Theta_{\text{Unloaded}})*\sqrt{\lambda}}{\text{Cos}(\Theta_{\text{Unloaded}})*\lambda^2}\right) \quad (5\text{-}5)$$

Here, Θ_{Unloaded} represents the unloaded fiber orientation at each transmural section, Θ_{Loaded} is the fiber angle after loading-induced realignment and λ is the amount of uniaxial stretch. We

hypothesized that uniaxial loading results in transmural realignment of RV myofibers towards the loading direction. Additionally, the transmural variation of fiber angles was approximated via linear regression (fiber angles vs. %thickness). Slope of the linear fit to transmural fiber angles demonstrates the helix slope of the RVFW (change in fiber angle per unit thickness), which was hypothesized to decrease in response to uniaxial loading.

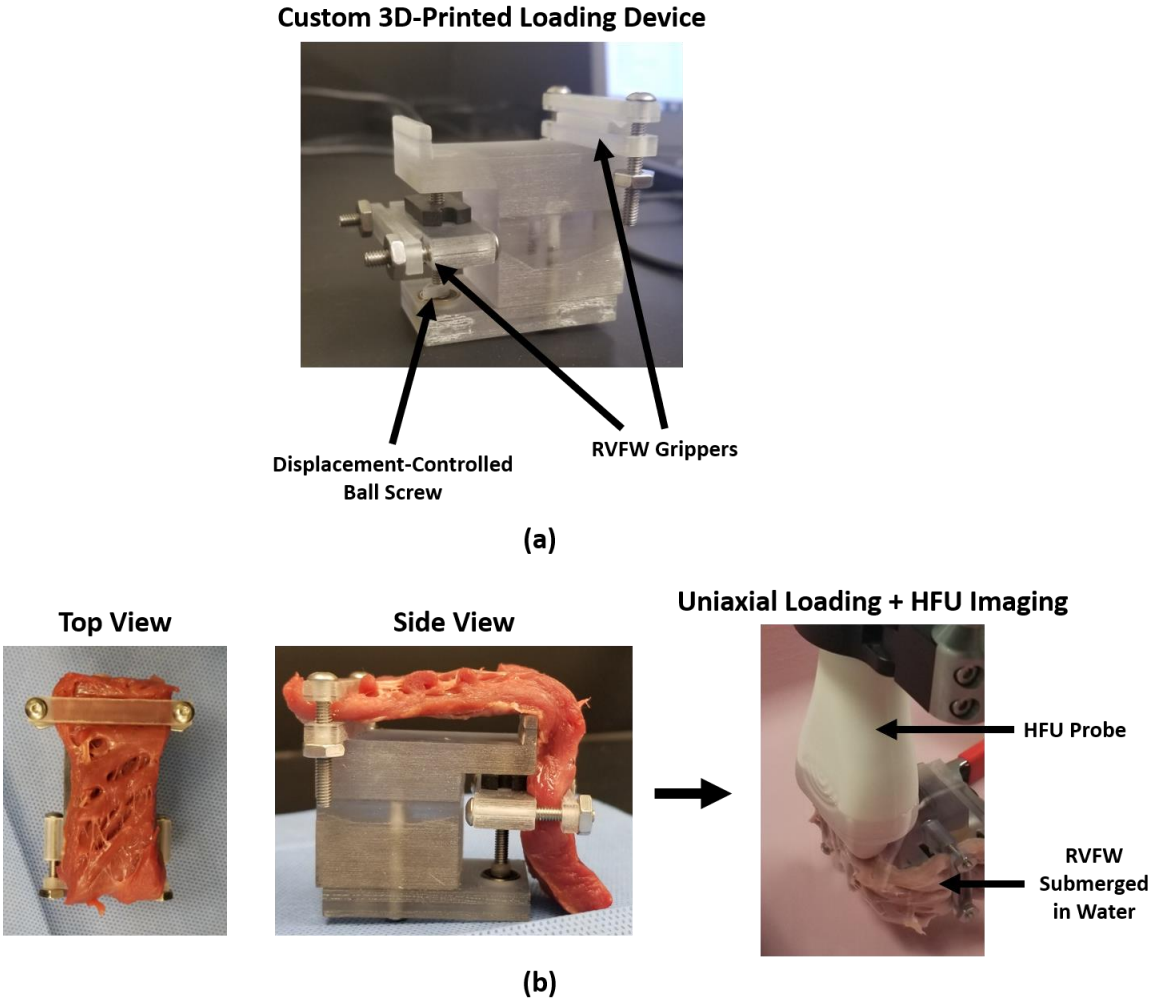

Figure 22 (a) The 3D-printed custom loading gripper used to evaluate RV myofiber kinematics under uniaxial loading. (b) Simultaneous uniaxial loading and HFU imaging of RVFW specimens.

5.2.2 Finite Element Modeling to Study RV Fiber Kinematics Under Biaxial Loading

While the developed HFU algorithm shows great potential for quantifying RV fiber kinematics, it requires imaging in the plane parallel to the RV wall (normal to the transmural axis). This demands at least one side of the planar RVFW specimen to be free for imaging, which complicates coupled biaxial loading and HFU imaging. Therefore, in the second stage of this study structurally-informed nonlinear-heterogenous-anisotropic FE models of the RVFW were created for an exploratory assessment of biaxial fiber kinematics under different loading scenarios. This will lay the groundwork for future experimental studies on biaxial RV fiber kinematics, while development of specialized loading grippers and improved imaging algorithms for coupled HFU imaging/biaxial loading is in progress.

5.2.2.1 Model Development

The modeling techniques used in this study have been described in detail in previous work (Thunes et al., 2016, 2018). A custom MATLAB subroutine was used to explicitly create planar fiber networks using the dominant orientation and fiber spreads (pooled standard deviation of orientation distributions from n=3 samples) measured via HFU imaging (Fig. 23). Myofibers, collagen, and the ECM were created with 93%, 4% and 3% volume fractions (Jane-Lise et al., 2000; Methe et al., 2014; Avazmohammadi et al., 2017a; Van Essen et al., 2018), respectively, to approximate the tissue-level biaxial properties (Nemavhola, 2017) of porcine RV myocardium (Table 5). The ECM was modeled using an incompressible isotropic hyperelastic constitutive model (Raghavan and Vorp, 2000):

$$W = \alpha(I_b - 3) + \beta(I_b - 3)^2 \tag{5-6}$$

Where α and β are constants representing the ECM mechanical properties, I_b is the first invariant of the left Cauchy-Green stretch tensor and W is the strain energy function when J=det(F)=1 ensures incompressibility (F represents the deformation gradient tensor). Collagen fibers were modeled with linear elastic properties, activated after a recruitment stretch (Thunes et al., 2016):

$$\sigma = \begin{cases} 0, & \lambda < \lambda_r \\ E_{col}(\lambda - \lambda_r), & \lambda \geq \lambda_r \end{cases} \tag{5-7}$$

Here, σ represents components of the Cauchy stress tensor, E_{col} is the stiffness of collagen fibers and λ_r is the stretch at which collagen recruitment begins (Table 5). Additionally, myofibers were modeled with a similar approach without a recruitment threshold (Table 5). To find the appropriate model parameters, simulated biaxial stress-stretch response of the generated fiber network (Fig. 23) was regressed against previously reported material properties of porcine RV myocardium (Nemavhola, 2017), while goodness of fit was determined using the coefficient of determination (R^2). For model verification, an unconfined uniaxial loading scenario (under λ=1.35) was simulated and compared with experimental HFU imaging measurements of RVFW fiber kinematics.

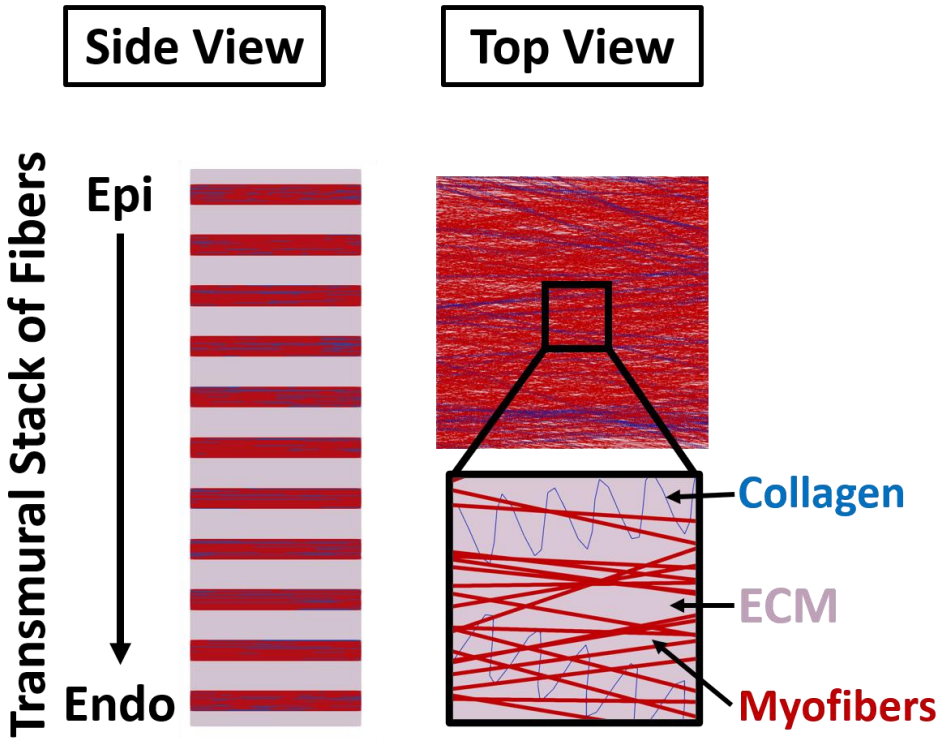

Figure 23 The representative volume element (RVE) FE model used to study biaxial RV fiber kinematics, demonstrating the transmural stack of fibers from epi to endocardium and distribution of myofibers, collagen, and ECM at each transmural section. Transmural fiber architectures (measured via HFU) and porcine RVFW material properties/volume fractions were used to generate the RVE.

Table 5 RV material properties and volume fractions used for FE modeling

	Volume Fraction	**Material Properties**	
ECM	3% (Jane-Lise et al., 2000; Avazmohammadi et al., 2017a)	α = 0.7 kPa	β = 1.5 kPa
Myofibers	93%	E_{myo} = 10 kPa	
Collagen Fibers	4% (Methe et al., 2014; Van Essen et al., 2018)	E_{col} = 1250 kPa	λ_r = 1.15±0.1

5.2.2.2 Loading Scenarios, Boundary Conditions and Fiber Realignment

Similar to previous work (Thunes et al., 2016, 2018; Chavoshnejad et al., 2020), we employed a two-level modeling approach to keep the computational burden tractable. While simulations were performed on a representative volume element (RVE; 1mm×1mm×RV thickness) of the RVFW incorporating tissue-level structural organization (Fig. 23), loading and boundary conditions were based on an extension of the law of Laplace, representing the entire RV approximated by an ellipsoidal geometry (Kovalova et al., 2005; Avazmohammadi et al., 2017b) (Fig. 24):

$$p = \frac{1}{2(b-w)^2}\left[\sigma_{Circ.}(a^2-(a-w)^2) + \sigma_{Long.}\left(\frac{b^4}{a^2} - \frac{(b-w)^4}{(a-w)^2}\right)\right] \tag{5-8}$$

$$pA_1 = \sigma_{Long.}A_2 \tag{5-9}$$

$$A_1 = \frac{\pi}{2}[(a-w)(b-w)-b^2] + \arctan\left(\frac{b-w}{a-w}\sqrt{\frac{(a-w)^2-b^2}{2bw-w^2}}\right)b^2 - \dots$$
$$\dots\ (a-w)(b-w)\arctan\left(\frac{(b-w)^2}{(a-w)^2}\sqrt{\frac{(a-w)^2-b^2}{2bw-w^2}}\right) \tag{5-10}$$

$$A_2 = \frac{\pi}{2}[ab-b^2] - A_1 \tag{5-11}$$

Here, p is the internal chamber pressure of the RV (diastolic or systolic pressure), $\sigma_{Circ.}$ and σ_{Long} are the RVFW wall stress (afterload) in the circumferential and longitudinal directions, w is the RV wall thickness, a and b are geometrical measures for biventricular modeling of the left and right ventricles using Laplace-type calculations (Fig. 24) and A_1 and A_2 respectively represent the

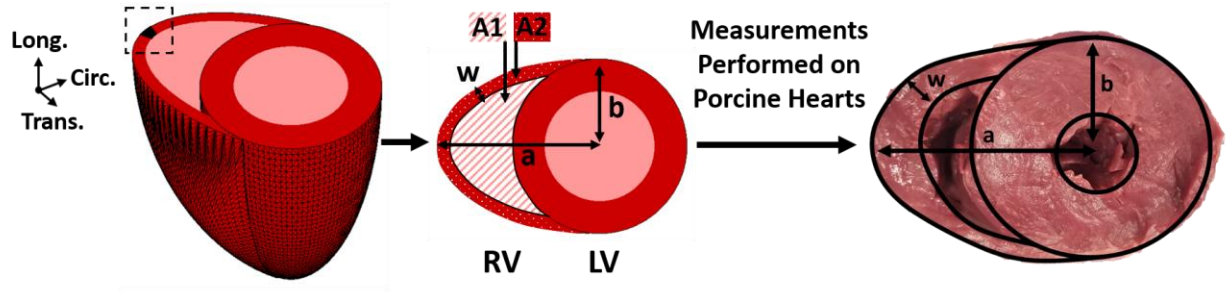

Figure 24 Loading and boundary condition calculations. In order to keep the computational burden tractable, simulations were performed on a representative volume element (RVE; shown in black in dotted box), and effects of the 3D RV geometry were modeled as loading and boundary conditions based on an extension of the law of Laplace for ellipsoidal geometries. Measurements were performed on porcine hearts to acquire the geometrical parameters required for modeling.

internal RV chamber area and the RVFW area, when looking at a basal short-axis cross-section of the ventricles (Fig. 24). Equations 5-8 to 5-11 approximate the RV geometry with an oblate spheroid (semi-axes: a,a,b) while the left ventricle (LV) is approximated with a prolate spheroid (semi-axes: b,b,L; when L represents the LV length). Detailed derivation of these equations have been described elsewhere (Avazmohammadi et al., 2017b) and were employed to estimate RV wall stress under pressure overload. Myofiber diameter (57.8±28.3 μm) and spacing (35.8±11.2 μm) were acquired form histological measurements to generate the appropriate number of fibers in the RVE (network of 79,263 fibers generated transmurally). Measurements were performed on 3 porcine hearts to obtain the required geometrical measures for modeling (Fig. 24; a = 64.7±5.8 mm, b = 34.7±2.5 mm, w = 9.8±1.6 mm, and L = 65.0±7.1 mm). Since systolic wall stress reaches peak values early in systole (Grossman et al., 1975) with minimal dimension change from end-diastole (Kuroha et al., 1991), same RV geometries were assumed for wall stress calculations at end-diastole and early-systole. Calculated wall stresses were then applied to the developed RVE to study the stretch-induced kinematics of RV fibers (Fig. 25).

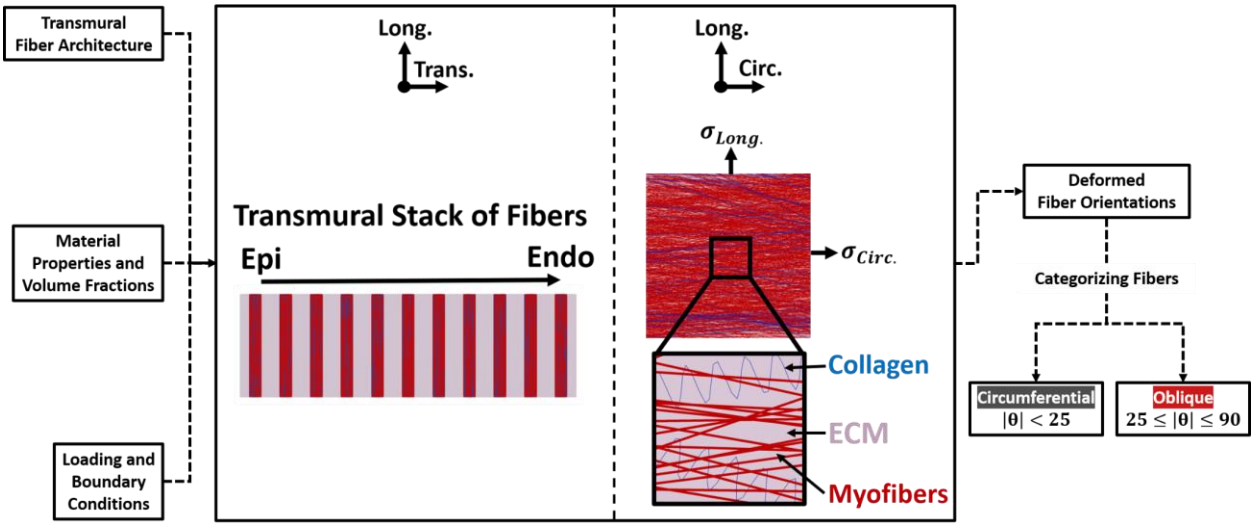

Figure 25 The RVE in the circumferential-longitudinal and longitudinal-transmural planes. Transmural fiber architectures (measured via HFU) and porcine RVFW material properties/volume fractions were used to generate the RVE. The calculated boundary conditions ($\sigma_{Circumferential}$ and $\sigma_{Longitudinal}$) were then applied in the circumferential-longitudinal plane to analyze biaxial RV fiber kinematics. Following simulations, fiber orientations of the RVE in the deformed state were categorized into circumferential ($|\theta| < 25$) and oblique ($25 \leq |\theta| \leq 90$) fibers.

First, we investigated biaxial kinematics under normotensive loading with healthy RV pressures and material properties and no major remodeling event present in the model (Tables 6-7). Additionally, an acute pressure overload (APO) scenario was studied to investigate the effects of acute pressure rise on biaxial fiber kinematics. Likewise, effects of chronic pressure overload (CPO) on fiber kinematics was studied under PH pressures (Tezuka et al., 1990) post-remodeling, while RVFW fibrosis (Hill et al., 2014), eccentric (Tezuka et al., 1990), and concentric (Guerreiro et al., 1988) hypertrophy (RV dilation and increased wall thickness, respectively) are present in the model (Tables 6-7). Since RV fiber realignment in PH is generally viewed as an end-stage remodeling event (Hill et al., 2014; Avazmohammadi et al., 2019a), this will help analyzing the alterations in fiber kinematics post RV remodeling in CPO. Furthermore, due to the previously

reported associations between aging and diminution of the extent of concentric RV hypertrophy in response to pressure overload (Kuroha et al., 1991), as well as lack of increased wall thickness in some animal models of PH (Avazmohammadi et al., 2019a, 2019b), another case of CPO loading without concentric hypertrophy was simulated to study the effects of increased wall thickness on fiber kinematics in PH (Tables 6-7).

Table 6 RV hemodynamics and remodeling parameters used for FE simulations

	RV Pressures (mmHg) (Tezuka et al., 1990)		**End-Diastolic Volume (mL)** (Tezuka et al., 1990)	**RVFW Thickness (mm)** (Guerreiro et al., 1988)	**Collagen Volume Fraction** (Methe et al., 2014; Van Essen et al., 2018)
	End-Diastole	**Early-Systole**			
Normotensive	4.9	31.3	27.7	9.8	4%
Acute Pressure Overload	14.3	105	27.7	9.8	4%
Chronic Pressure Overload	14.3	105	34.1	13.4	12%
Chronic Pressure Overload Without Concentric Hypertrophy	14.3	105	34.1	9.8	12%

Table 7 Circumferential and longitudinal wall stresses applied to the representative volume element (RVE) for different loading scenarios

	End-Diastole		**Early-Systole**	
	$\sigma_{Circ.}$ (kPa)	**$\sigma_{Long.}$ (kPa)**	**$\sigma_{Circ.}$ (kPa)**	**$\sigma_{Long.}$ (kPa)**
Normotensive	0.62	0.37	3.96	2.37
Acute Pressure Overload	1.81	1.08	13.30	7.94
Chronic Pressure Overload	0.87	0.66	6.37	4.81
Chronic Pressure Overload Without Concentric Hypertrophy	1.53	1.58	11.22	11.64

Moreover, a series of simulations were conducted to analyze the effects of RV fibrosis on PH-induced fiber kinematics by parametrically altering the collagen content in our model (1.5, 2 and 3-fold increase; Fig. 26). This, together with the abovementioned simulation scenarios for CPO without concentric hypertrophy, will help decoupling the observed effects from fibrosis, concentric, and eccentric RV hypertrophy under CPO.

Simulations were performed under diastolic and early-systolic pressures for a single cycle of loading, in order to analyze the direction and rate of fiber reorientation under different scenarios. Since a single cycle of loading may not result in statistically significant differences in the mean of fiber orientation distributions (Streeter et al., 1969), similar to previous studies (Streeter et al., 1969; Tezuka et al., 1990), post-deformation fiber orientations were categorized as circumferential ($|\theta| < 25$) and oblique ($25 \leq |\theta| \leq 90$), to facilitate statistical testing of changes in the proportion of fiber orientations (Fig. 25). Thresholds for categorizing circumferential/oblique fibers were chosen in a way to include the undeformed fiber orientations ± at least 1 standard deviation of fiber spreads (dispersion) within the circumferential range (Fig. 27). Therefore, an increase in the proportion of oblique fibers indicates fiber reorientation away from the circumferential direction, as seen in the setting of PH (Hill et al., 2014; Avazmohammadi et al., 2017b, 2019a).

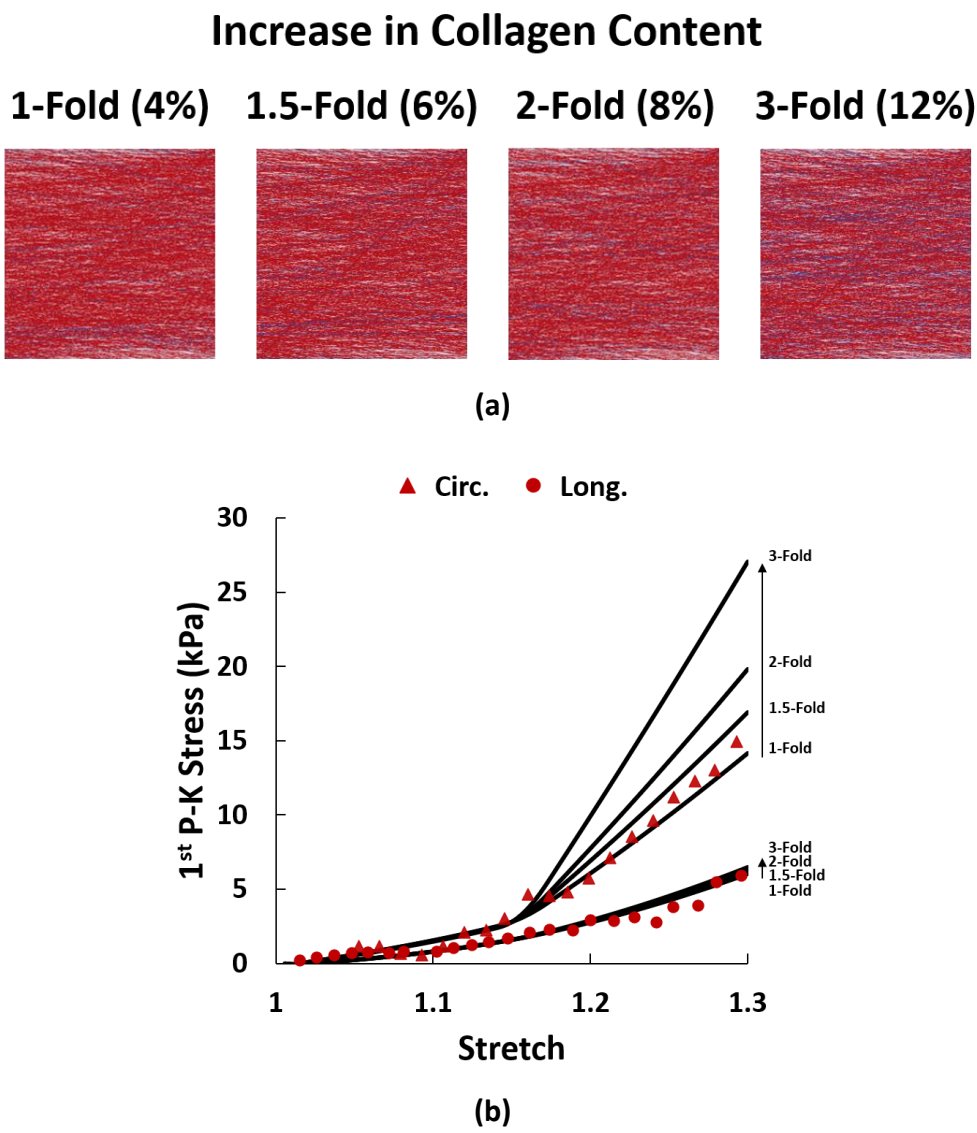

Figure 26 Simulation of increased RV collagen content (fibrosis) using the developed FE model. (a) Parametric increase in RV collagen content. Red: Myofibers, Blue: Collagen. (b) Effects of parametric increases in RV collagen content on the biaxial mechanical properties of RV myocardium. Experimental data (shown in red) obtained from the literature (Nemavhola, 2017). Material properties of the structurally-informed FE model shown with black lines.

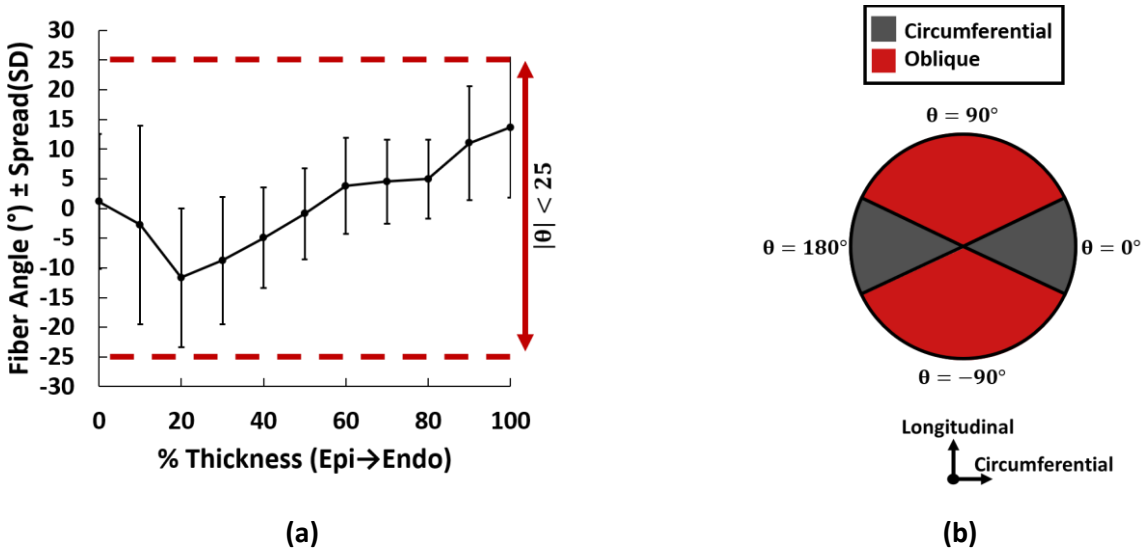

Figure 27 Rationale for the threshold used for categorizing circumferential and oblique fibers. (a) Fiber angle threshold used for categorizing circumferential fibers ($|\theta| < 25$). (b) Graphical demonstration of circumferential and oblique fibers in a circular plane. Deformed RV fiber orientations were grouped into circumferential ($|\theta| < 25$) and oblique ($25 \leq |\theta| \leq 90$) categories, following finite element simulations. The threshold for circumferential fibers was chosen in a way to include the initial HFU-measured fiber angles and at least 1 standard deviation of the fiber spread at each transmural section. Fibers outside of this threshold were labeled as "oblique". An increase in the proportion of oblique fibers indicates fiber reorientation away from the circumferential direction, towards the longitudinal direction (±90°). Error bars demonstrate the fiber spread at each transmural section (pooled standard deviation of the distribution of fiber orientations measured via HFU imaging on n=3 specimens).

In case of no statistically significant alteration in the proportion of fiber orientations, simulations were aborted after the first cycle (Fig. 28). Since, physiologically, fiber remodeling in PH happens over multiple cycles of loading (Hill et al., 2014; Avazmohammadi et al., 2019a; Sharifi Kia et al., 2020), when proportions were significantly altered, fiber orientations were updated using the deformation gradient tensor and simulations were proceeded to the next cycle (Fig. 28):

$$f_{n+1} = F_n f_n \tag{5-12}$$

Here, f_n is the undeformed orientation of any given fiber at the nth cycle, F_n is the deformation gradient tensor for the n^{th} cycle and f_{n+1} represents the undeformed fiber orientation at the start of the $n+1^{th}$ cycle. This is conceptually similar to previously developed models for stretch-induced fiber remodeling in other cardiovascular soft tissues (Driessen et al., 2008). In the current work, simulations were continued up to 4 cycles under CPO for an exploratory assessment of the trends in fiber realignment in PH. FE model post-processing was performed using ParaView (Sandia National Labs, Kitware Inc, and Los Alamos National Labs).

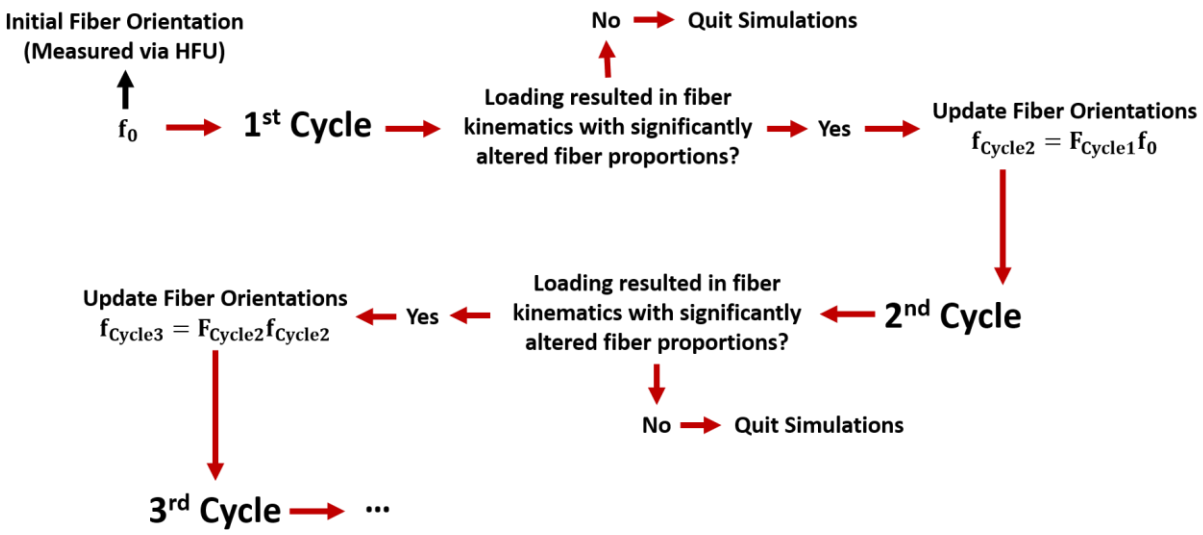

Figure 28 The remodeling algorithm used for multi-cycle simulations to study the adaptation of RV fibers towards the longitudinal direction in chronic pressure overload (CPO). Deformed fiber orientations were analyzed at the end of each cycle. If loading altered the fiber proportions in a statistically significant manner, fiber orientations were updated using the described criteria and simulations were proceeded to the next cycle. In case of no loading-induced alteration in the proportion of fibers, simulations were aborted.

5.2.3 Statistical Analysis

Data is presented with mean ± standard deviation (SD)/standard error of the mean (SEM), or proportion (%) of fibers post-categorization. A one-way repeated measures ANOVA with Tukey's post-hoc was used for pairwise comparison of RV helix slope before and after loading and theoretical predictions of affine reorientation. A R^2 measure was used to evaluate the agreement between experimentally measured uniaxial fiber kinematics and theoretical estimations or FE model predictions. In addition, R^2 measures were also used to evaluate the goodness of fit between experimentally measured biaxial mechanical properties of the RVFW and FE model predictions.

Chi-squared ($\chi 2$) tests were performed to evaluate if fiber proportions were dependent on the loading condition. Post-hoc Z-tests with Bonferroni correction were utilized to test the differences across different loading scenarios. Due to integer overflow issues and limitations of the $\chi 2$ test for very large sample sizes, fiber counts were down sampled by a factor of 10, post categorization. This was chosen as an optimal down sampling rate required to avoid numerical instabilities when working with very large sample sizes (n=79,263) from our FE model.

Statistical comparisons were performed using the R software package (R Foundation for Statistical Computing, Vienna, Austria, www.R-project.org). Due to the small sample size in our experimental data and proportion testing (as opposed to tests of the mean) for FE simulations, a more strict measure was chosen for statistical comparisons. For all purposes, $p<0.01$ (two-sided) was considered statistically significant.

5.3 Results

5.3.1 HFU Imaging

Transmural RV myofiber orientations measured via HFU imaging and histology are compared in Fig. 29. HFU imaging showed an acceptable agreement with histological staining of fiber orientations both in terms of the dominant orientation and spread of myofibers.

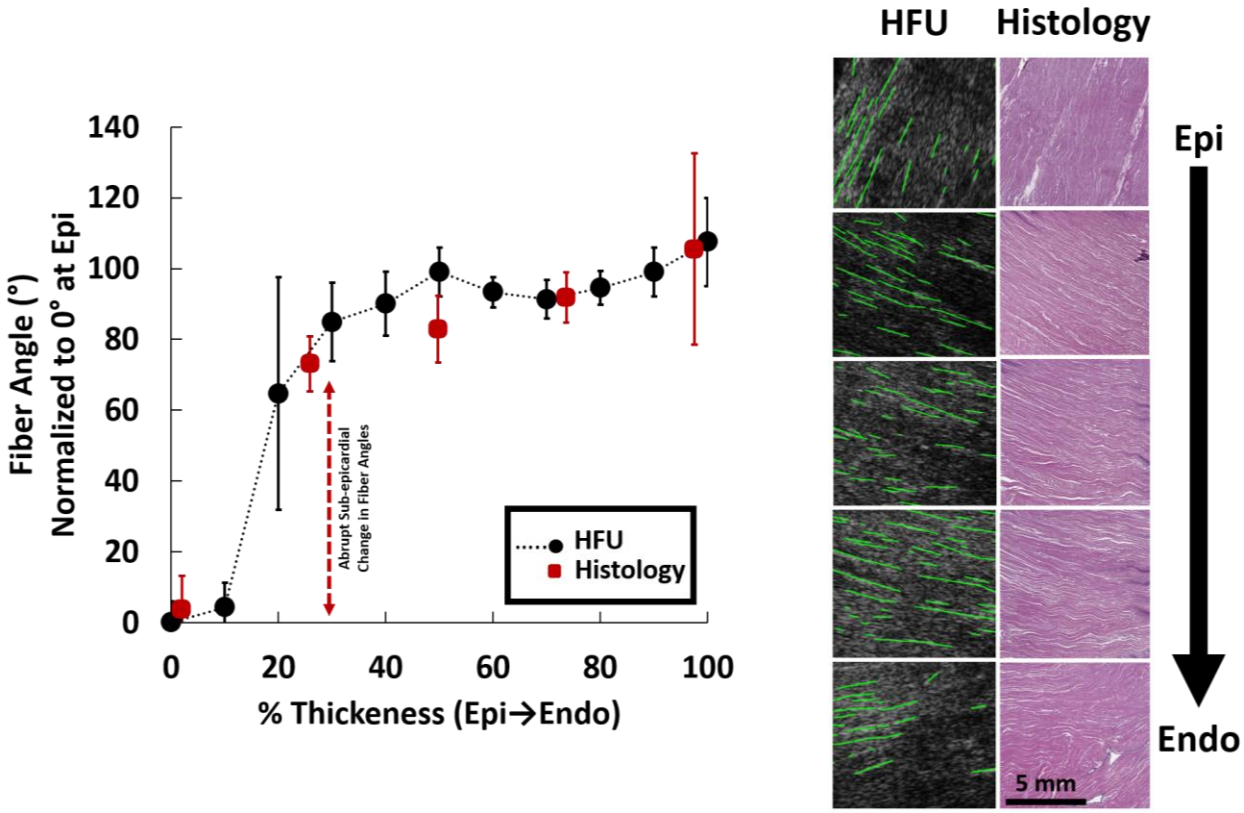

Figure 29 Algorithm verification by comparing HFU measurements with histological staining (H&E). Error bars demonstrate fiber spread (standard deviation of the distribution of fiber orientations; measure of fiber dispersion) at each transmural section. Fiber angles are normalized to 0° at the epicardial layer, to better demonstrate the transmural change in fiber angles and facilitate comparison with previous studies. Dotted lines between HFU measurements are for visualization purposes only.

Unloaded RV fiber orientations in the basal anterior zone demonstrated an abrupt change (Vetter et al., 2005) around the sub-epicardial layers (Fig. 29; 142.4±52.1°; n=4; 1 specimen used for histological validation + 3 specimens for uniaxial loading experiments), followed by a near-linear change in transmural fiber angles (Fig. 29; 28.5±9.8°; n=4). The abrupt sub-epicardial change showed high between-sample variability, ranging from 64.7° to 175.2° (n=4).

Uniaxial loading (n=3) resulted in fiber realignment towards the loading direction (Fig. 30 and Fig. 31a), in agreement with theoretical predictions of affine fiber kinematics (R^2=0.92; Fig. 31a).

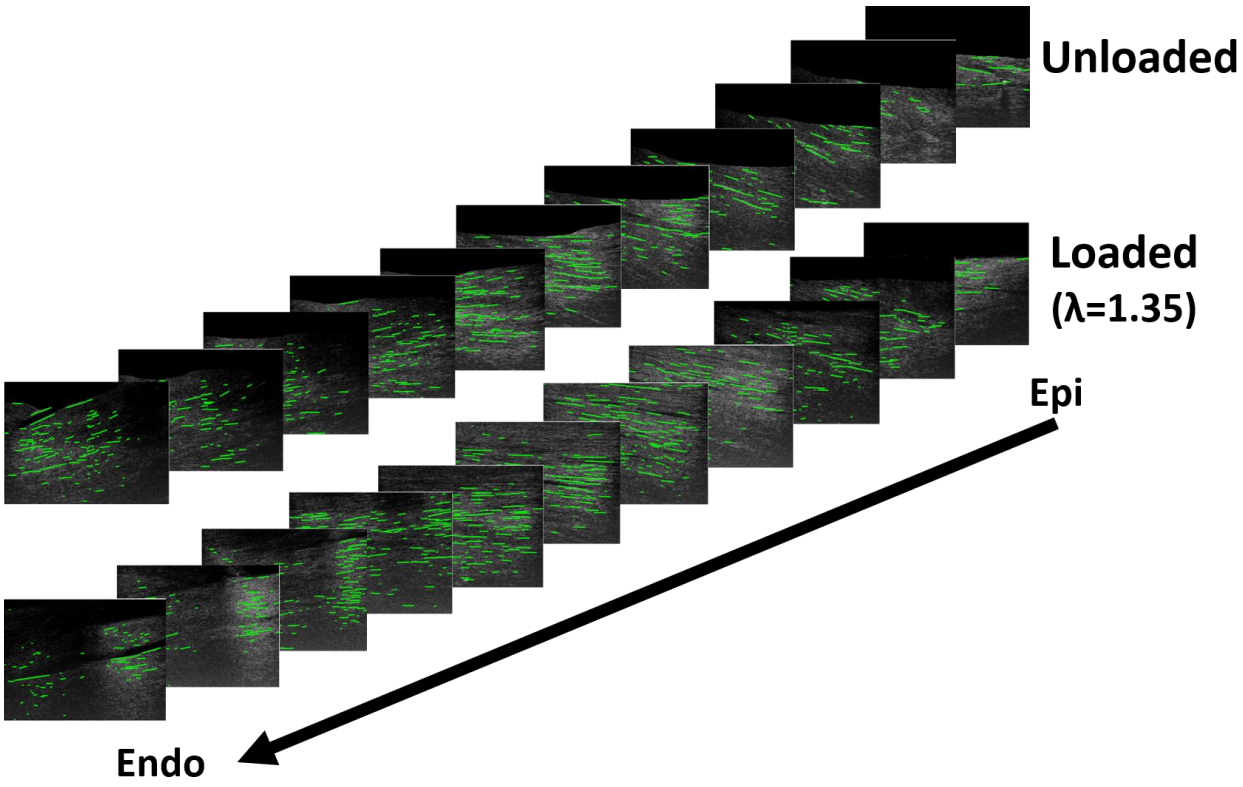

Figure 30 Representative transmural HFU images of RVFW fiber orientations, before and after loading under a stretch ratio of λ = 1.35.

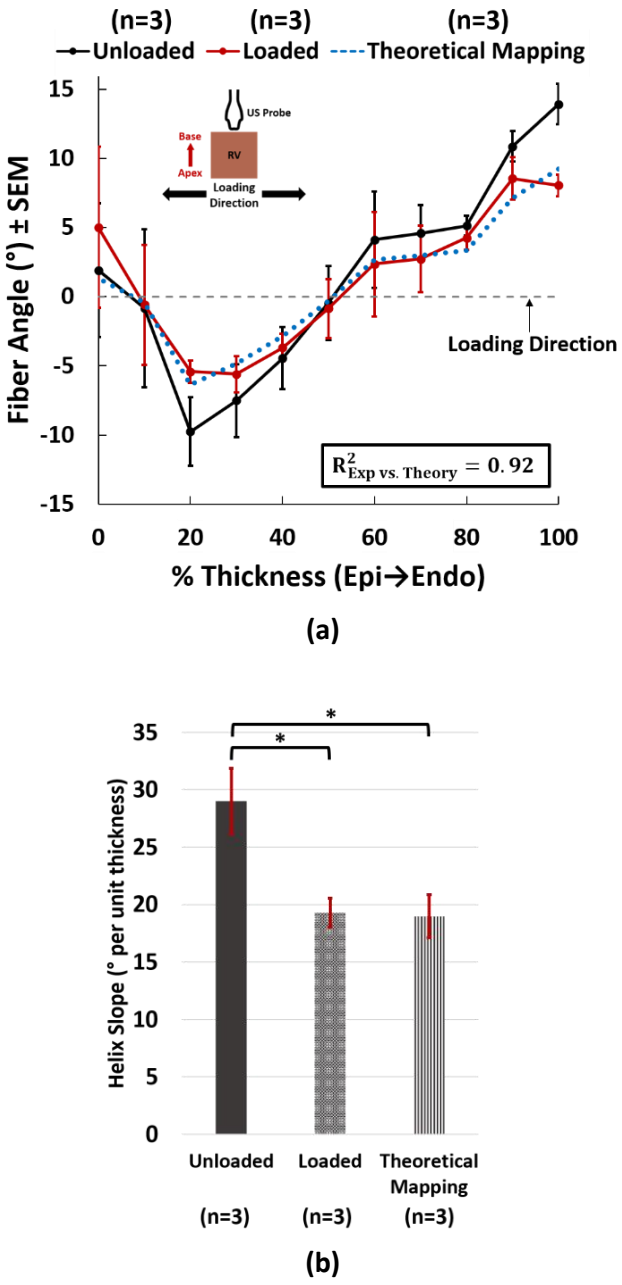

Figure 31 Uniaxial myofiber kinematics under a stretch ratio of λ = 1.35. (a) Quantification of fiber angles using the developed framework. Uniaxial loading results in fiber reorientation towards the loading direction (0°). Experimental measurements demonstrate good agreement with theoretical approximations of affine fiber kinematics for an incompressible transversely isotropic solid (R^2=0.92). (b) Effects of loading on RVFW helix slope. Loading results in decreased RVFW helix slope, which does not show any statistically significant differences with theoretical affine approximations. Error bars show standard error of the mean (SEM). * indicates p<0.01. US Probe: Ultrasound probe; Exp: Experimental.

For all kinematics analysis purposes, fiber orientations are reported in the RV circumferential-longitudinal coordinate system (Fig. 31a). Assuming a counterclockwise transmural rotation for RV fibers (Vetter et al., 2005; Hill et al., 2014; Sharifi Kia et al., 2020), the abrupt epicardial change is plotted with the shortest map to 0° to better demonstrate fiber realignment towards the loading direction (1.9° and -0.8° shown for 0% and 10% thickness in Fig. 31a correspond to 180°+1.9°=181.9° and 180°-0.8°=179.2°, respectively). Uniaxial loading resulted in significantly reduced RV helix slope (Fig. 31b; 19.3±2.2° vs. 29.0±5.0° per unit thickness for loaded and unloaded, respectively; $p<0.001$), while showing no significant differences with theoretical predictions of uniaxial affine fiber kinematics (Fig. 31b; 19.0±3.3° per unit thickness; $p<0.001$ vs. unloaded and $p=0.983$ vs. loaded).

5.3.2 FE Modeling

The developed structurally-informed FE model matched the mechanical properties of RV myocardium in both longitudinal and circumferential directions (Fig. 32a; $R^2_{Long.}=0.94$, $R^2_{Circ.}=0.99$), as well as the experimentally measured uniaxial fiber kinematics (Fig. 32b; $R^2=0.89$). Fiber proportions were calculated based on a total of n=79,263 fibers generated in the FE model. Categorizing RV fibers in an unloaded state resulted in 94.1% circumferential and 5.9% oblique fibers (proportions calculated by grouping all transmural sections together). Full statistical results of biaxial fiber kinematics in the first cycle of loading are presented in Appendix Tables S5-6. In response to a single cycle of loading, stretch-induced kinematics under normotensive and APO conditions did not increase the proportion of oblique fibers for either end-diastolic (Fig. 33a; 5.9% for Norm, 5.8% for APO) or early-systolic (Fig. 33b; 5.8% for Norm, 6.9% for APO) pressures. CPO, on the other hand, significantly increased the proportion of oblique fibers under early-

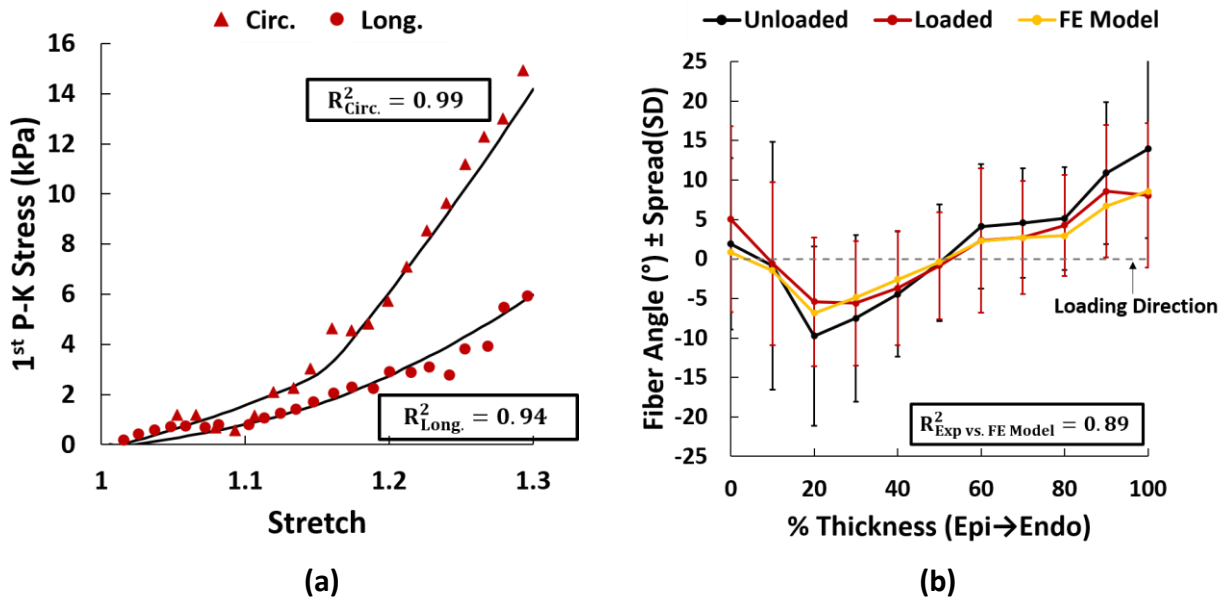

Figure 32 (a) Quality of fit of the structurally-informed FE model to previously reported biaxial material properties of porcine RV myocardium. (b) FE model predictions vs. experimentally measured uniaxial RV fiber kinematics. Error bars demonstrate the fiber spread at each transmural section. Exp: Experimental.

systolic pressures by 35%, while showing no significant effects at end-diastole (Fig. 33a-b; 8.0% for CPO at early-systole and 6.6% at end-diastole). For CPO with no concentric RV hypertrophy present in the model, proportion of oblique fibers increased by 101% at early-systole and 40% at end-diastole (Fig. 33a-b; 11.8% for CPO w/o Conc. Hyp. at early-systole and 8.2% at end-diastole). Following the first cycle of loading, multi-cycle remodeling simulations (Fig. 28) were performed for the CPO scenarios under early-systolic pressures. Simulations demonstrated RV fiber realignment towards the longitudinal direction (Fig. 34a-b), with higher remodeling rates for the case without concentric hypertrophy (Fig. 34b). Figure 35 demonstrates a representative shift in fiber distributions, with increased proportion of oblique fibers, for each loading scenario. Categorizing RV fibers at each transmural section after 4 cycles of remodeling, showed a significant increase in the proportion of oblique fibers for both scenarios (Fig. 36; $p<0.001$ for

CPO or CPO w/o Conc. Hyp. compared to Normotensive at all transmural sections). Concentric hypertrophy resulted in significantly smaller proportions of oblique fibers throughout the RVFW thickness (Fig. 36; $p<0.001$ for CPO vs. CPO w/o Conc. Hyp at all transmural sections).

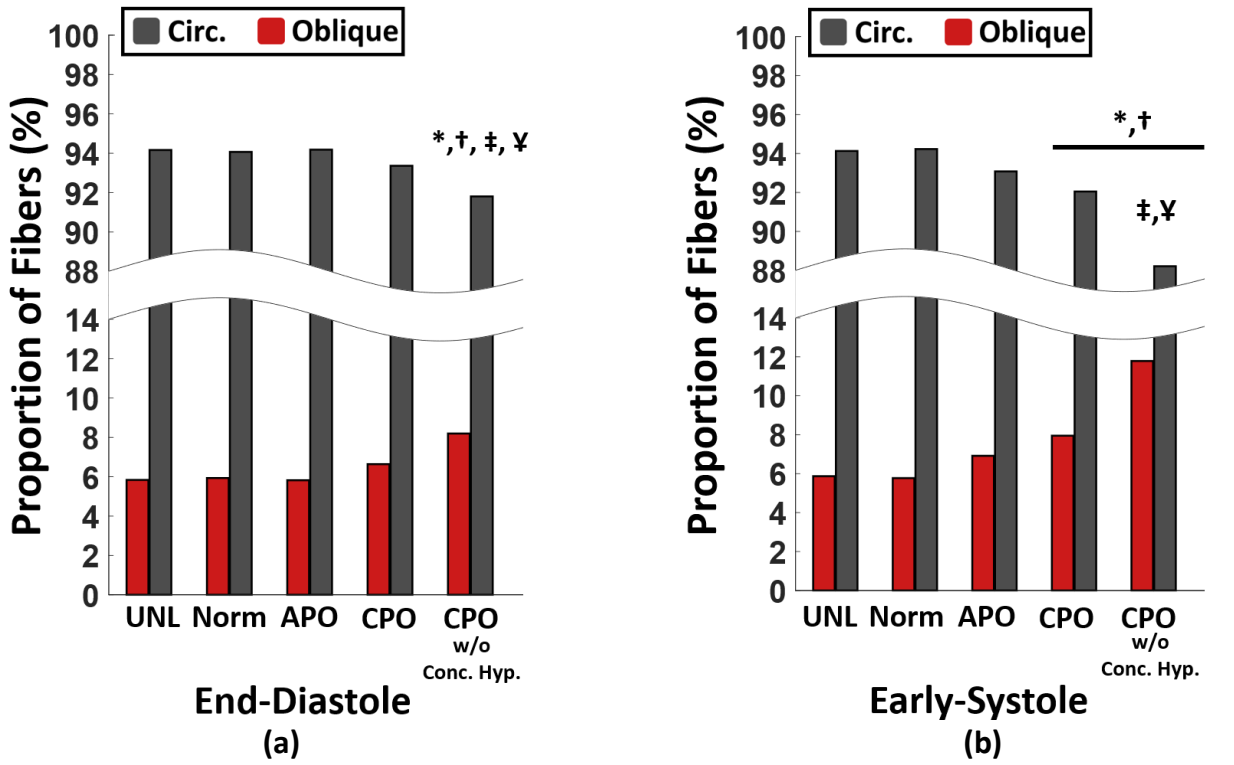

Figure 33 Effects of different loading scenarios on biaxial fiber kinematics of RV myocardium. (a) Effects of loading on end-diastolic fiber kinematics, indicating increased proportion of oblique fibers only for the CPO scenario without concentric hypertrophy (single-cycle simulations). (b) Effects of loading on early-systolic fiber kinematics, demonstrating elevated proportions of oblique fibers under both CPO scenarios with amplified proportions for CPO without concentric hypertrophy (single-cycle simulations). *, †, ‡ and ¥ indicate $p<0.01$ compared to UNL (unloaded), Norm (normotensive), APO (acute pressure overload) and CPO (chronic pressure overload), respectively. UNL: Unloaded; Norm: Normotensive; APO: Acute pressure overload; CPO: Chronic pressure overload; CPO w/o Conc. Hyp.: Chronic pressure overload without concentric hypertrophy.

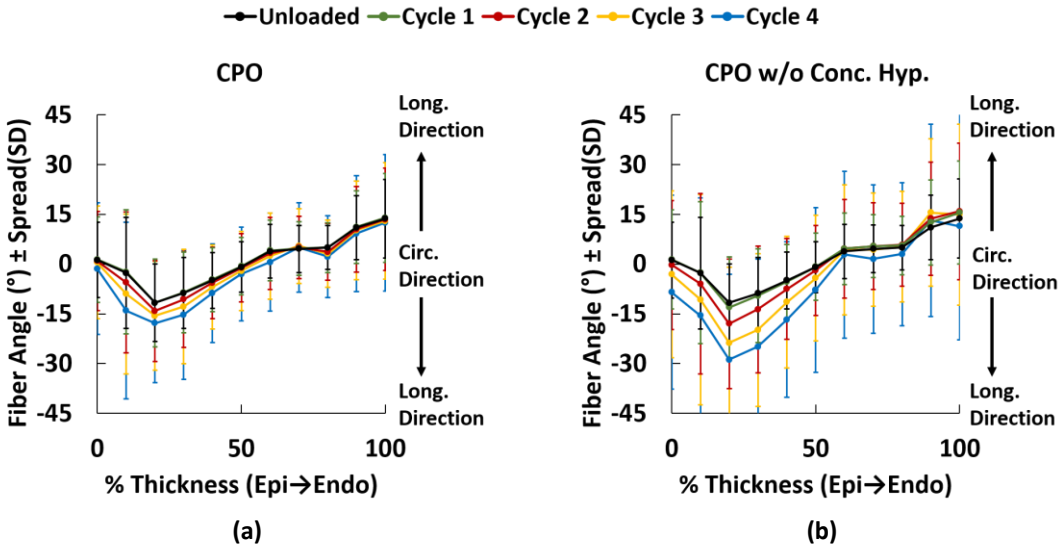

Figure 34 Multi-cycle simulations of RV fiber reorientation towards the longitudinal direction (±90°) under (a) CPO and (b) CPO without concentric RV hypertrophy. Error bars demonstrate fiber spread (standard deviation of the distribution of fiber orientations) at each transmural section. CPO: Chronic pressure overload; CPO w/o Conc. Hyp.: Chronic pressure overload without concentric hypertrophy.

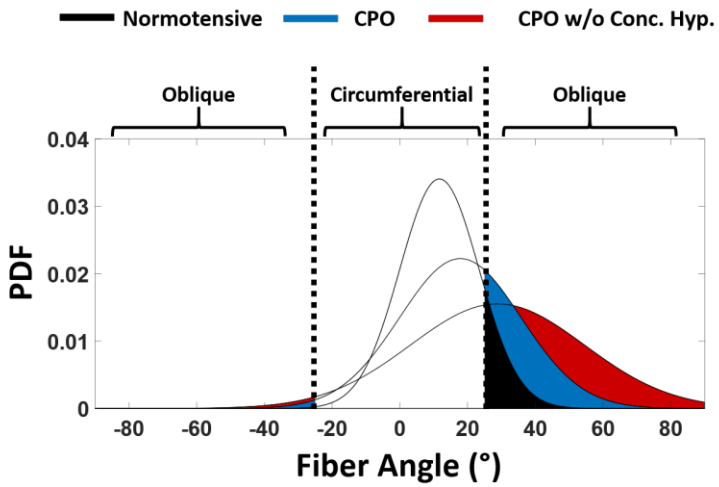

Figure 35 Representative fiber orientation distributions for multi-cycle remodeling simulations under CPO, demonstrating a shift towards oblique fibers for both scenarios. Shaded area under the curves demonstrate the oblique fibers. Both CPO scenarios result in remodeling towards the longitudinal direction (±90°) with increased proportion of oblique fibers. CPO: Chronic pressure overload, CPO w/o Conc. Hyp.: Chronic pressure overload without concentric RV hypertrophy, PDF: Probability density function.

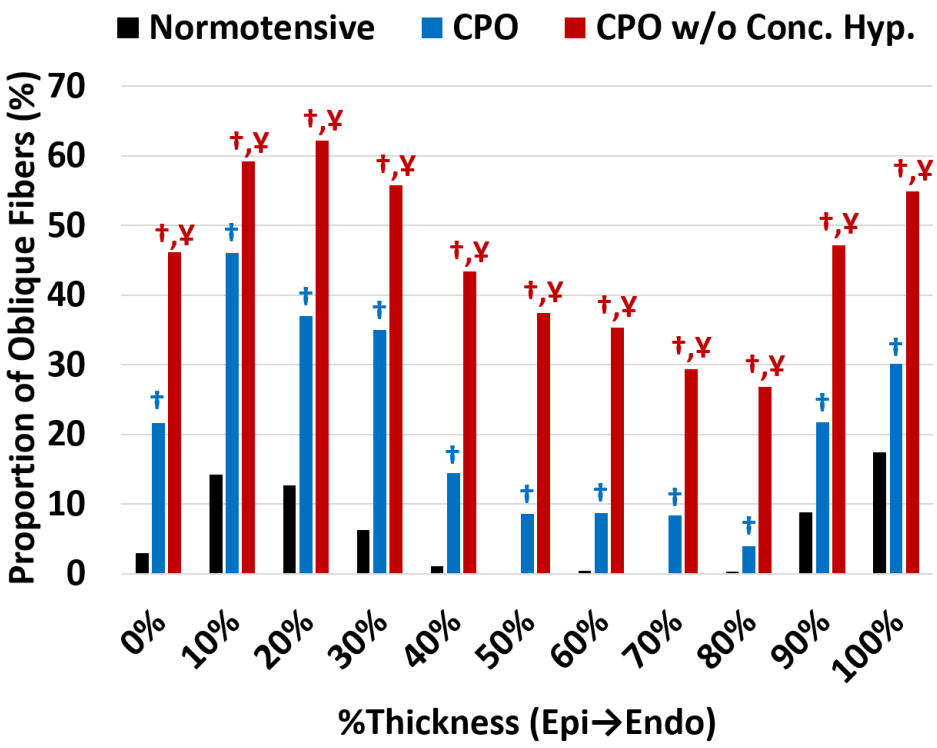

Figure 36 Proportion of oblique fibers for the normotensive scenario compared to CPO with and without concentric hypertrophy. Fiber proportions for the CPO cases are plotted following 4 cycles of remodeling simulations, while normotensive loading quits the remodeling algorithm following the first cycle of loading. Both CPO scenarios result in significant increases in the proportion of oblique fibers compared to normotensive loading at all transmural sections (epi to endocardium). Increased wall thickness (CPO vs. CPO w/o Conc. Hyp.) decreases the rate of longitudinal realignment, indicating a potential protective role for concentric hypertrophy against RV fiber reorientation in CPO. † and ¥ indicate $p<0.01$ compared to Normotensive and CPO (chronic pressure overload), respectively. CPO: Chronic pressure overload; CPO w/o Conc. Hyp.: Chronic pressure overload without concentric hypertrophy.

Fibrosis, on the other hand, did not show any significant effects on RV fiber kinematics under end-diastolic (Fig. 37a; 6.6%, 6.6%, 6.6%, and 6.6%, respectively for 1,1.5,2, and 3-fold increase in collagen content) or early-systolic pressures (Fig. 37b; 7.6%, 7.8%, 7.8%, and 8%, respectively for 1,1.5,2, and 3-fold increase in collagen content).

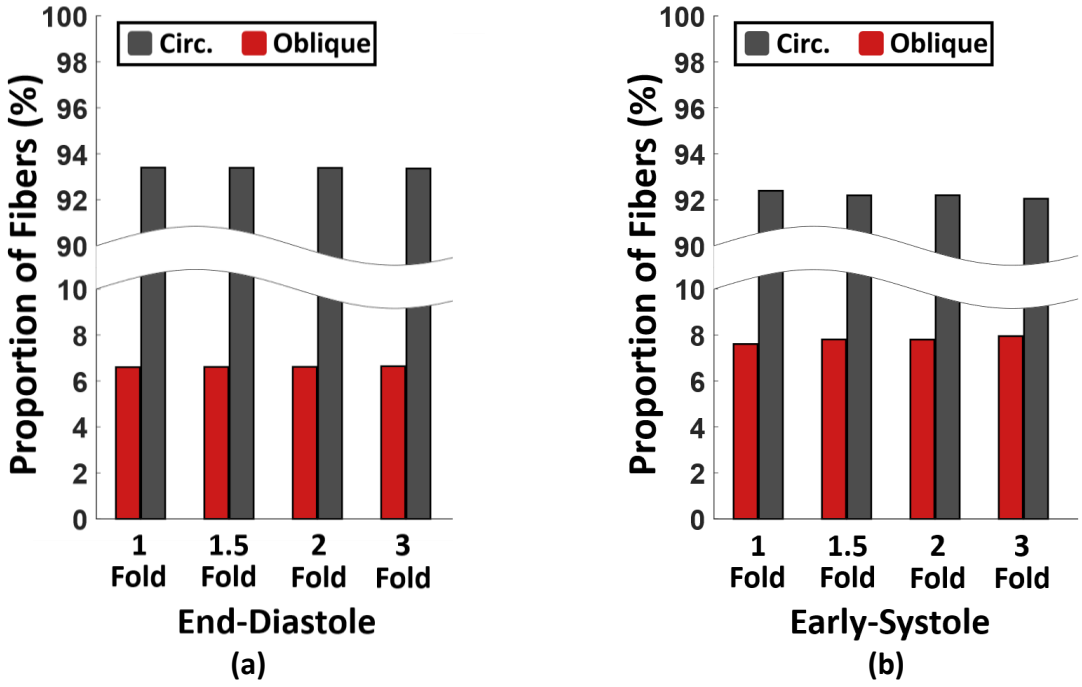

Figure 37 Effects of fibrosis on biaxial RV fiber kinematics under chronic pressure overload with concentric and eccentric hypertrophy, under (a) End-diastolic and (b) Early-systolic pressures. RV fibrosis did not demonstrate any statistically significant alteration in fiber proportions at end-diastole or early-systole.

5.4 Discussion and Conclusions

In this work, we aimed to evaluate the stretch-induced fiber kinematics of RV myocardium under different loading scenarios. The primary findings of this study were: 1) HFU imaging demonstrated a strong potential for quantifying full-thickness transmural orientations of RV myofibers in large animal models; 2) Uniaxial loading resulted in fiber realignment towards the loading direction, in agreement with theoretical predictions based on affine fiber kinematics; 3) FE modeling demonstrated that a combination of chronic pressure overload with RVFW fibrosis and concentric and eccentric hypertrophy (increased wall thickness and chamber dilation, respectively), but not solely an acute rise in RV pressures, results in kinematic shift of RV fibers

away from the circumferential direction; 4) Computational exploratory assessments revealed a potential protective role for concentric hypertrophy against longitudinal fiber realignment in PH, while eccentric hypertrophy stimulated fiber reorientation towards the longitudinal direction.

HFU imaging effectively characterized the transmural orientation distribution (dominant orientation and fiber spread) of myofibers in porcine RV myocardium (Fig. 29). Difficulties were observed in delineation of the endocardial surface via HFU imaging, mainly due to the trabeculations at endocardium, as also reported in previous studies (Partington and Kilner, 2017). This resulted in differences between the HFU and histologically measured fiber spreads at endocardium, while dominant fiber orientations were accurately characterized (Fig. 29). As previously reported in porcine models of RV structure (Vetter et al., 2005), an abrupt change in fiber angles with high between-sample variability was observed near the sub-epicardial layers. This was followed by a near-linear change in orientations towards the endocardium (Fig. 29). The observed transmural variation in fiber angles (epi→endo) in the basal anterior zone (28.5±9.8°) was smaller than previously reported values, potentially due to the body size and procurement source of tissues used in this study (farmed animals with ≈80-120 kg body weight) compared to younger animals used in previous work, with ≈5-20 kg body weight (Agger et al., 2017; Omann et al., 2019). Decreased transmural variation in fiber orientations with increased body size has also been reported in prior investigations (Healy et al., 2011).

As expected, uniaxial loading of RV myocardium resulted in realignment of fibers towards the loading direction with decreased transmural variation (Fig. 30 and Fig. 31). While not representing a physiological loading experienced by the RVFW in-vivo, uniaxial loading can provide fundamental insights into the kinematic response of RV fibers, which remains poorly understood. Since fiber reorientation in PH happens over multiple cycles of growth and remodeling

(Avazmohammadi et al., 2019a), as anticipated, we did not observe dramatic changes in fiber angles under a single cycle of passive uniaxial loading. However, RV myofibers demonstrated a strong agreement with theoretical predictions of uniaxial affine kinematics (Fig. 31), thus indicating affine assumptions can effectively approximate myofiber realignment in the RVFW. To the best of our knowledge, this is the first report on quantitative HFU assessment of full-thickness RV fiber kinematics.

FE simulations revealed the role of stretch-induced deformations on longitudinal kinematics of RV fibers in PH. In an unloaded state, circumferential fibers dominated the fiber proportions in the RVFW (Fig. 33). This is in general agreement with previous studies on a porcine model (Omann et al., 2019), indicating the basal anterior zone of RVFW as one of the most circumferentially aligned regions. Small, but significant alterations in fiber proportions were noted after a single cycle of loading under pressure overload conditions (Fig. 33). The observed changes in fiber angles in the first cycle of loading are in general agreement with previously reported values (Ashikaga et al., 2009). As anticipated, normotensive loading did not demonstrate any significant effects on the proportions of RV fibers (Fig. 33a-b). Even though an acute pressure rise imposes the largest wall stresses on the RVFW (Table 7), surprisingly, this did not significantly alter the proportion of RV fibers. This is potentially due to the importance of the ratio (and not just absolute values) of the biomechanical stimuli (strain) in fiber reorientation (Driessen et al., 2008). While RV stresses are highest during APO, this may not result in deformed configurations required for stimulating longitudinal fiber kinematics (Fig. 20). This is mainly a combined effect from hemodynamic pressures, RV geometry and RVFW biomechanical properties in APO that lead to deformation states where ratio of longitudinal:circumferential strains does not stimulate longitudinal fiber reorientation. In contrast, CPO with a combination of remodeling events (Table

6; increased wall thickness, RV dilation, and fibrosis) significantly increased the proportion of oblique fibers (Fig. 33), indicating fiber remodeling away from the circumferential direction. This is in agreement with prior studies, identifying fiber realignment as an end-stage event in PH (Hill et al., 2014; Avazmohammadi et al., 2019a). Elimination of increased wall thickness from our FE models amplified fiber realignment towards the longitudinal direction (Fig. 34 and Fig. 36). This suggests a potential protective role for increased wall thickness against fiber reorientation in PH. Animal models of PH without concentric hypertrophy (Avazmohammadi et al., 2019a) have demonstrated similar levels of fiber remodeling under significantly lower RV pressures compared to those developing concentric hypertrophy (Hill et al., 2014; Sharifi Kia et al., 2020). A potential explanation to be further explored in future studies is simultaneous reduction of RV wall stress and alterations in the ratio of longitudinal:circumferential strains via increased wall thickness in PH.

Parametric studies on the level of RV fibrosis did not show any effects on fiber proportions under early-systolic or end-diastolic pressures (Fig. 37). Between the three remodeling events studied here (increased wall thickness, dilation, and fibrosis), this leaves RV dilation as a potential contributor to the kinematic shift of RV fibers towards the longitudinal direction in PH. Others have shown longitudinal fiber realignment in PH to be accompanied by progressive RV dilation and reduced ejection fractions (Avazmohammadi et al., 2019a). Our results suggest another pathway for RV dilation to modulate longitudinal fiber remodeling via altered RVFW wall stress and stretch ratios, in addition to the previously addressed dilation-induced fiber kinematics due to volumetric growth (Avazmohammadi et al., 2019a). A potential mechanism to be investigated in future work is alteration in the biomechanical stimuli (ratio and magnitude of stress/strains) in the myofiber niche due to progressive RV dilation.

There are limitations to the experimental and FE modeling techniques used in the current work. HFU images were acquired under uniaxial loading, as it is currently not feasible under biaxial loading due to the requirement of imaging normal to the transmural axis (parallel to the RVFW) which necessitates at least one side of the RVFW specimen to be free for imaging. Ongoing work focuses on development of improved algorithms using spatial coherence maps to facilitate 3D imaging parallel to the RV transmural axis. While demonstrating strong statistics and minimal variabilities, the small sample size (n=3) used for our exploratory experimental analysis remains as a limitation of the current study. Although our models provide insights into the stretch-induced fiber kinematics of RV myocardium under biaxial loading, future experimental studies are needed to confirm the generated hypotheses via FE modeling. Furthermore, as described in Fig. 19, the deformed state of RVFW during early-systole (IVC) includes a stretch-driven deformation in addition to a myofiber contraction mode. Our FE models did not include the contraction mode (myofiber shortening), mainly due to the computational complexity of modeling contraction on a RVE without representing the 3D RV geometry. However, systolic myofiber shortening has been shown to result in deformations with ratio of longitudinal:circumferential strains close to 1 (ratio of global longitudinal to circumferential strains ranging from 0.99 to 1.04 for normotensive subjects, as well as subjects with hypertrophic or dilated cardiomyopathy (Stokke et al., 2017)). Therefore, while this affects the magnitude of the strains calculated in our models, it is less likely to affect the ratio of longitudinal:cirecumferential strains (mainly responsible for stimulating fiber rotations; Fig. 20) in a way to obstruct the observed trends in longitudinal realignment of RV fiber. Additionally, end-stage PH has been shown to reduce systolic myofiber shortening (Voeller et al., 2011), which makes the contraction mode less likely to mechanistically stimulate transmural fiber reorientation in PH. Our results only explain a specific stretch-driven aspect of RV fiber

realignment and future work will focus on development of 3D organ-level FE simulations to effectively model the fiber kinematics at early-systole considering both deformation modes. Moreover, even though the underlying mechanisms of fiber reorientation in PH remains largely unexplored, reorientation due to altered fiber kinematics and biomechanical stimuli in the myofiber niche (Wilson et al., 2006; Driessen et al., 2008; Avazmohammadi et al., 2019a) is only one of the several potential mechanisms responsible for this remodeling event. Other mechanisms such as degradation of circumferentially aligned fibers accompanied by sarcomerogenesis of longitudinal fibers (Avazmohammadi et al., 2019a) need to be further investigated in future fiber-level studies.

In conclusion, we employed HFU imaging and structurally-informed computational models for an exploratory study on the stretch-induced kinematics of RV fibers under different loading scenarios. The developed imaging framework provides a noninvasive modality to characterize the transmural fiber kinematics of RV myocardium. Simulations suggest a potential protective role for concentric RV hypertrophy (increased wall thickness) against fiber reorientation. On the other hand, accounting for eccentric hypertrophy (RV dilation) in FE models resulted in kinematic shift of fibers towards the longitudinal direction, due to altered stretch ratios in the RVFW. While this helps better understanding the role of different remodeling events and biomechanical forces in transmural realignment of RV fibers in PH, future experimentations are warranted to test the model-generated hypotheses.

6.0 Conclusions and Future Directions

In this work, we aimed to evaluate right ventricular (RV) biomechanics in health, and in the setting of pressure overload due to pulmonary hypertension (PH). Effects of combined angiotensin receptor-neprilysin inhibition (using Sacubitril/Valsartan; Sac/Val) on RV remodeling in PH was analyzed at the organ, tissue, and fiber level. Moreover, we evaluated the effects of healthy aging on RV structure and biomechanical properties. Additionally, an ultrasound image processing framework (in combination with computational models) was utilized to study the effects of different loading scenarios on the reorientation patterns of RV myofibers in porcine myocardium. The primary findings of this study are:

- Sac/Val has the potential to prevent maladaptive RV remodeling in a pressure overload model via amelioration of RV pressure rise, hypertrophy, collagen and myofiber re-orientation as well as RV stiffening both at the tissue and myofiber level.
- Healthy aging modulates RV remodeling via increased peak pressures, cardiomyocyte loss, fiber reorientation, and altered collagen/myofiber stiffness, with similar remodeling patterns to those of RV remodeling in PH.
- The developed high-frequency ultrasound imaging framework demonstrates promising capabilities for characterization of the transmural orientation distribution of RV myofibers in porcine myocardium, showing a strong potential for noninvasive evaluation of transmural RV myofiber kinematics in large animal models.
- Image-based experimental evaluation of fiber kinematics in porcine myocardium reveals the capability of affine assumptions to effectively approximate myofiber realignment in the RV free wall.

- Computational models (finite element simulations) suggest a potential protective role for concentric hypertrophy (increased wall thickness) against fiber reorientation, while indicating a longitudinal shift in fiber orientations due to eccentric hypertrophy (RV dilation).

While our study improves the current understanding of multi-scale biomechanics of RV remodeling in PH, there remains a number of questions warranting further investigation. As discussed in chapter 3, a pulmonary artery banding model of PH was used in this study to focus on the biomechanical response of RV myocardium in the absence of confounding conditions such as hypoxia or pulmonary circulation disease. However, further investigation of effects of Sac/Val in other animal models of PH is warranted. Moreover, we employed a preventive treatment approach to analyze the effects of Sac/Val on PH in a 3-week period. Different treatment windows as well as treatment scenarios after fully developing PH needs to be further investigated. A phenomenological constitutive model was used for analysis of our biomechanical testing data in chapters 3 and 4, without considering the structural organization of RV collagen and myofibers. Structurally-informed constitutive models enable analyzing the relative contributions of different tissue constituents and RV free wall architecture to the tissue-level mechanical response. Additionally, as discussed in chapters 3 and 4, fiber-level collagen and myofiber stiffness measures in this study represent the effective response of RV fibers, estimated from tissue-level behavior. Further direct measurements at the fiber level would facilitate decoupling the effects of RV structure from intrinsic mechanical properties. High-frequency ultrasound images in chapter 5 were acquired under uniaxial loading, due to the complexity of combined biaxial loading and ultrasound imaging and limitations of the developed algorithm. While our computational models provide important insights into the stretch-induced fiber kinematics of RV myocardium under

biaxial loading, future experimental studies are required to confirm the model-generated hypotheses. Moreover, our finite element models only evaluated the passive components of RV myofiber kinematics and did not include the contraction mode (myofiber shortening). Development of organ-level 3D structurally-detailed models of the RV facilitate analyzing the effects of RV contraction and segmental shortening on the kinematics of myofibers.

To achieve our overarching goal of acquiring a holistic understanding of the underlying biomechanics of RV remodeling in PH, future work will focus on:

- Evaluation of the effects of Sac/Val treatment on PH-induced RV remodeling, using other animal models of PH (Sugen-Hypoxia and Monocrotaline)
- Analyzing the potential of Sac/Val treatment in reversal of maladaptive RV remodeling in PH, post-development of symptoms (treatment approach vs. the prevention approach used in the current work)
- Employment of a structurally-detailed constitutive model for biomechanical analysis of the effects of Sac/Val treatment on collagen-myofiber interactions in PH
- Fiber-level biomechanical testing of RV collagen and myofibers in health, disease, and treatment
- Analyzing the potential of lysyl oxidase-mediated alterations in RV free wall collagen cross-linking with healthy aging
- Development of improved ultrasound imaging algorithms, using spatial coherence maps, to facilitate simultaneous biaxial loading and ultrasound imaging of RV myofiber kinematics

- Development of structurally-detailed 3D organ-level finite element models of RV function, coupled with lumped-parameter models of the pulmonary circulation, to evaluate the effects of different loading scenarios and remodeling events on active and passive RV myofiber kinematics
- Experimental evaluation of the potential of an adaptive role for increased wall thickness and a maladaptive role for RV dilation in longitudinal fiber reorientation in PH, as suggested by computational modeling results

Appendix A Supplemental Tables

Appendix Table S1 p values obtained for pairwise comparison of different hemodynamic outcomes

	Control vs. PH	Control vs. Sac/Val	PH vs. Sac/Val
Maximum Pressure (P_{max})	<0.0001	<0.0001	0.0018
Stroke Volume	0.0033	0.1113	1.0
dP/dt_{max}	<0.0001	0.0015	0.0119
dP/dt_{min}	<0.0001	0.0004	0.0426
PA Elastance (E_a)	<0.0001	0.0002	0.0158
RV Elastance (E_{es})	<0.0001	0.0110	0.8440
E_{es}/E_a	0.0005	0.5914	0.1087

Appendix Table S2 p values obtained for pairwise comparison of morphological measurements

	Control vs. PH	Control vs. Sac/Val	PH vs. Sac/Val
RVFW Thickness	<0.0001	<0.0001	0.0061
RV/LV Mass Ratio	<0.0001	<0.0001	0.5500

Appendix Table S3 p values obtained for pairwise comparison of histological measurements

	Control vs. PH	Control vs. Sac/Val	PH vs. Sac/Val
Dominant Orientation	0.0026	0.5687	0.0106
Collagen Area Fraction	0.0444	0.0065	1.0
RVFW Density	0.0049	0.1246	0.1487

Appendix Table S4 p values obtained for pairwise comparison of biaxial mechanical properties and constitutive modeling results

	Control vs. PH	Control vs. Sac/Val	PH vs. Sac/Val
Myofiber Stiffness	0.0470	1.0	0.0320
Collagen Recruitment Strain	0.0002	0.0003	0.7023
Long. Stiffness (B_0*b_1)	<0.0001	0.0003	0.0259
Circ. Stiffness (B_0*b_2)	0.0022	0.3990	0.0039
Coupled Stiffness (B_0*b_3)	<0.0001	0.0160	0.0950

Appendix Table S5 p values obtained for pairwise comparison of different loading scenarios at end-diastole (Fig. 33a)

	Norm	APO	CPO	CPO w/o Conc. Hyp.
UNL	1.0	1.0	0.4582	<0.001
Norm	-	1.0	0.8105	<0.001
APO	-	-	0.4137	<0.001
CPO	-	-	-	0.0034

Appendix Table S6 p values obtained for pairwise comparison of different loading scenarios at early-systole (Fig. 33b)

	Norm	APO	CPO	CPO w/o Conc. Hyp.
UNL	1.0	0.0968	<0.001	<0.001
Norm	-	0.0446	<0.001	<0.001
APO	-	-	0.1801	<0.001
CPO	-	-	-	<0.001

Bibliography

Agger, P., Ilkjær, C., Laustsen, C., Smerup, M., Frandsen, J. R., Ringgaard, S., et al. (2017). Changes in overall ventricular myocardial architecture in the setting of a porcine animal model of right ventricular dilation. *J. Cardiovasc. Magn. Reson.* 19, 93. doi:10.1186/s12968-017-0404-0.

Agger, P., Lakshminrusimha, S., Laustsen, C., Gugino, S., Frandsen, J. R., Smerup, M., et al. (2016). The myocardial architecture changes in persistent pulmonary hypertension of the newborn in an ovine animal model. *Pediatr. Res.* 79, 565–574. doi:10.1038/pr.2015.263.

Akazawa, Y., Okumura, K., Ishii, R., Slorach, C., Hui, W., Ide, H., et al. (2020). Pulmonary artery banding is a relevant model to study the right ventricular remodeling and dysfunction that occurs in pulmonary arterial hypertension. *J. Appl. Physiol.* 129, 238–246. doi:10.1152/japplphysiol.00148.2020.

Akhavein, F., Jean St-Michel, E., Seifert, E., and Rohlicek, C. V. (2007). Decreased left ventricular function, myocarditis, and coronary arteriolar medial thickening following monocrotaline administration in adult rats. *J. Appl. Physiol.* 103, 287–295. doi:10.1152/japplphysiol.01509.2005.

Andersen, S., Schultz, J. G., Andersen, A., Ringgaard, S., Nielsen, J. M., Holmboe, S., et al. (2014). Effects of bisoprolol and losartan treatment in the hypertrophic and failing right heart. *J. Card. Fail.* 20, 864–873. doi:10.1016/j.cardfail.2014.08.003.

Anversa, P., Palackal, T., Sonnenblick, E. H., Olivetti, G., Meggs, L. G., and Capasso, J. M. (1990). Myocyte cell loss and myocyte cellular hyperplasia in the hypertrophied aging rat heart. *Circ. Res.* 67, 871–885. doi:10.1161/01.RES.67.4.871.

Ashikaga, H., van der Spoel, T. I. G., Coppola, B. A., and Omens, J. H. (2009). Transmural Myocardial Mechanics During Isovolumic Contraction. *JACC Cardiovasc. Imaging* 2, 202–211. doi:10.1016/j.jcmg.2008.11.009.

Attard, M. I., Dawes, T. J. W., De Marvao, A., Biffi, C., Shi, W., Wharton, J., et al. (2019). Metabolic pathways associated with right ventricular adaptation to pulmonary hypertension: 3D analysis of cardiac magnetic resonance imaging. *Eur. Heart J. Cardiovasc. Imaging* 20, 668–676. doi:10.1093/ehjci/jey175.

Avazmohammadi, R., Hill, M. R., Simon, M. A., Zhang, W., and Sacks, M. S. (2017a). A novel constitutive model for passive right ventricular myocardium: evidence for myofiber–collagen fiber mechanical coupling. *Biomech. Model. Mechanobiol.* 16, 561–581. doi:10.1007/s10237-016-0837-7.

Avazmohammadi, R., Hill, M., Simon, M., and Sacks, M. (2017b). Transmural remodeling of right ventricular myocardium in response to pulmonary arterial hypertension. *APL Bioeng.* 1, 016105. doi:10.1063/1.5011639.

Avazmohammadi, R., Mendiola, E. A., Li, D. S., Vanderslice, P., Dixon, R. A. F., and Sacks, M. S. (2019a). Interactions Between Structural Remodeling and Hypertrophy in the Right Ventricle in Response to Pulmonary Arterial Hypertension. *J. Biomech. Eng.* 141, 0910161–13. doi:10.1115/1.4044174.

Avazmohammadi, R., Mendiola, E. A., Soares, J. S., Li, D. S., Chen, Z., Merchant, S., et al. (2019b). A Computational Cardiac Model for the Adaptation to Pulmonary Arterial Hypertension in the Rat. *Ann. Biomed. Eng.* 47, 138–153. doi:10.1007/s10439-018-02130-y.

Badesch, D. B., Raskob, G. E., Elliott, C. G., Krichman, A. M., Farber, H. W., Frost, A. E., et al. (2010). Pulmonary arterial hypertension: Baseline characteristics from the REVEAL registry. *Chest* 137, 376–387. doi:10.1378/chest.09-1140.

Benza, R. L., Park, M. H., Keogh, A., and Girgis, R. E. (2007). Management of Pulmonary Arterial Hypertension With a Focus on Combination Therapies. *J. Hear. Lung Transplant.* 26, 437–446. doi:10.1016/j.healun.2007.01.035.

Berens, P. (2009). CircStat: a MATLAB toolbox for circular statistics. *J. Stat. Softw.* 31, 1–21. doi:10.18637/jss.v031.i10.

Billiar, K. L., and Sacks, M. S. (2000). Biaxial mechanical properties of the native and glutaraldehyde-treated aortic valve cusp: Part II - A structural constitutive model. *J. Biomech. Eng.* 122, 327–336. doi:10.1115/1.1287158.

Bogaard, H. J., Natarajan, R., Henderson, S. C., Long, C. S., Kraskauskas, D., Smithson, L., et al. (2009). Chronic pulmonary artery pressure elevation is insufficient to explain right heart failure. *Circulation* 120, 1951–1960. doi:10.1161/CIRCULATIONAHA.109.883843.

Borgdorff, M. A., Bartelds, B., Dickinson, M. G., Steendijk, P., and Berger, R. M. F. (2013). A cornerstone of heart failure treatment is not effective in experimental right ventricular failure. *Int. J. Cardiol.* 169, 183–189. doi:10.1016/j.ijcard.2013.08.102.

Bossone, E., D'Andrea, A., D'Alto, M., Citro, R., Argiento, P., Ferrara, F., et al. (2013). Echocardiography in pulmonary arterial hypertension: From diagnosis to prognosis. *J. Am. Soc. Echocardiogr.* 26, 1–14. doi:10.1016/j.echo.2012.10.009.

Bovendeerd, P. H. M., Rijcken, J., Van Campen, D. H., Schoofs, A. J. G., Nicolay, K., and Arts, T. (1999). "Optimization of Left Ventricular Muscle Fiber Orientation," in *Solid Mechanics and its Applications* (Springer, Dordrecht), 285–296. doi:10.1007/0-306-46939-1_25.

Burke, R. M., Lighthouse, J. K., Mickelsen, D. M., and Small, E. M. (2019). Sacubitril/Valsartan Decreases Cardiac Fibrosis in Left Ventricle Pressure Overload by Restoring PKG Signaling in Cardiac Fibroblasts. *Circ. Heart Fail.* 12, e005565. doi:10.1161/CIRCHEARTFAILURE.118.005565.

Cappelli, V., Forni, R., Poggesi, C., Reggiani, C., and Ricciardi, L. (1984). Age-dependent variations of diastolic stiffness and collagen content in rat ventricular myocardium. *Arch. Physiol. Biochem.* 92, 93–106. doi:10.3109/13813458409071133.

Carruth, E. D., McCulloch, A. D., and Omens, J. H. (2016). Transmural gradients of myocardial structure and mechanics: Implications for fiber stress and strain in pressure overload. *Prog. Biophys. Mol. Biol.* 122, 215–226. doi:10.1016/j.pbiomolbio.2016.11.004.

Chavoshnejad, P., More, S., and Razavi, M. J. (2020). From surface microrelief to big wrinkles in skin: A mechanical in-silico model. *Extrem. Mech. Lett.* 36, 100647. doi:10.1016/j.eml.2020.100647.

Cheng, T. C., Philip, J. L., Tabima, D. M., Hacker, T. A., and Chesler, N. C. (2018). Multiscale structure-function relationships in right ventricular failure due to pressure overload. *Am. J. Physiol. - Hear. Circ. Physiol.* 315, H699–H708. doi:10.1152/ajpheart.00047.2018.

Chia, E. M., Hsieh, C. H. C., Boyd, A., Pham, P., Vidaic, J., Leung, D., et al. (2014). Effects of age and gender on right ventricular systolic and diastolic function using two-dimensional speckle-tracking strain. *J. Am. Soc. Echocardiogr.* 27, 1079-1086.e1. doi:10.1016/j.echo.2014.06.007.

Choi, H. S., and Vito, R. P. (1990). Two-dimensional stress-strain relationship for canine pericardium. *J. Biomech. Eng.* 112, 153–159. doi:10.1115/1.2891166.

Chouabe, C., Ricci, E., Amsellem, J., Blaineau, S., Dalmaz, Y., Favier, R., et al. (2004). Effects of aging on the cardiac remodeling induced by chronic high-altitude hypoxia in rat. *Am. J. Physiol. - Hear. Circ. Physiol.* 287, H1246–H1253. doi:10.1152/ajpheart.00199.2004.

Chuong, C. J., Sacks, M. S., Templeton, G., Schwiep, F., and Johnson, R. L. (1991). Regional deformation and contractile function in canine right ventricular free wall. *Am. J. Physiol. - Hear. Circ. Physiol.* 260, H1224–H1235. doi:10.1152/ajpheart.1991.260.4.h1224.

Clements, R. T., Vang, A., Fernandez-Nicolas, A., Kue, N. R., Mancini, T. J., Morrison, A. R., et al. (2019). Treatment of Pulmonary Hypertension With Angiotensin II Receptor Blocker and Neprilysin Inhibitor Sacubitril/Valsartan. *Circ. Heart Fail.* 12, e005819. doi:10.1161/CIRCHEARTFAILURE.119.005819.

Clemons, T. D., Bradshaw, M., Toshniwal, P., Chaudhari, N., Stevenson, A. W., Lynch, J., et al. (2018). Coherency image analysis to quantify collagen architecture: Implications in scar assessment. *RSC Adv.* 8, 9661–9669. doi:10.1039/c7ra12693j.

D'Andrea, A., Vriz, O., Carbone, A., Ferrara, F., Di Maio, M., Cocchia, R., et al. (2017). The impact of age and gender on right ventricular diastolic function among healthy adults. *J. Cardiol.* 70, 387–395. doi:10.1016/j.jjcc.2016.12.005.

De Jong, A. M., Maass, A. H., Oberdorf-Maass, S. U., Van Veldhuisen, D. J., Van Gilst, W. H., and Van Gelder, I. C. (2011). Mechanisms of atrial structural changes caused by stretch occurring before and during early atrial fibrillation. *Cardiovasc. Res.* 89, 754–765. doi:10.1093/cvr/cvq357.

De Simone, V., Guarise, P., Zanotto, G., and Morando, G. (2019). Reduction in pulmonary artery pressures with use of sacubitril/valsartan. *J. Cardiol. Cases* In Press. doi:10.1016/j.jccase.2019.08.006.

Driessen, N. J. B., Cox, M. A. J., Bouten, C. V. C., and Baaijens, F. P. T. (2008). Remodelling of the angular collagen fiber distribution in cardiovascular tissues. *Biomech. Model. Mechanobiol.* 7, 93–103. doi:10.1007/s10237-007-0078-x.

Effron, M. B., Bhatnagar, G. M., Spurgeon, H. A., Ruaño-Arroyo, G., and Lakatta, E. G. (1987). Changes in myosin isoenzymes, ATPase activity, and contraction duration in rat cardiac muscle with aging can be modulated by thyroxine. *Circ. Res.* 60, 238–245. doi:10.1161/01.RES.60.2.238.

Ehrsam, R. E., Perruchoud, A., Oberholzer, M., Burkart, F., and Herzog, H. (1983). Influence of age on pulmonary haemodynamics at rest and during supine exercise. *Clin. Sci.* 65, 653–660. doi:10.1042/cs0650653.

Faber, M. J., Dalinghaus, M., Lankhuizen, I. M., Steendijk, P., Hop, W. C., Schoemaker, R. G., et al. (2006). Right and left ventricular function after chronic pulmonary artery banding in rats assessed with biventricular pressure-volume loops. *Am. J. Physiol. - Hear. Circ. Physiol.* 291, H1580-6. doi:10.1152/ajpheart.00286.2006.

Fajemiroye, J. O., Cunha, L. C. Da, Saavedra-Rodríguez, R., Rodrigues, K. L., Naves, L. M., Mourão, A. A., et al. (2018). Aging-Induced Biological Changes and Cardiovascular Diseases. *Biomed Res. Int.* 2018, 1–14. doi:10.1155/2018/7156435.

Fan, D., Wannenburg, T., and De Tombe, P. P. (1997). Decreased myocyte tension development and calcium responsiveness in rat right ventricular pressure overload. *Circulation* 95, 2312–2317. doi:10.1161/01.CIR.95.9.2312.

Fata, B., Zhang, W., Amini, R., and Sacks, M. S. (2014). Insights into regional adaptations in the growing pulmonary artery using a meso-scale structural model: Effects of ascending aorta impingement. *J. Biomech. Eng.* 136, 0210091–13. doi:10.1115/1.4026457.

Ferreira, P. F., Kilner, P. J., Mcgill, L. A., Nielles-Vallespin, S., Scott, A. D., Ho, S. Y., et al. (2014). In vivo cardiovascular magnetic resonance diffusion tensor imaging shows evidence of abnormal myocardial laminar orientations and mobility in hypertrophic cardiomyopathy. *J. Cardiovasc. Magn. Reson.* 16, 87. doi:10.1186/s12968-014-0087-8.

Fiechter, M., Fuchs, T. A., Gebhard, C., Stehli, J., Klaeser, B., Stähli, B. E., et al. (2013). Age-related normal structural and functional ventricular values in cardiac function assessed by magnetic resonance. *BMC Med. Imaging* 13, 1–6. doi:10.1186/1471-2342-13-6.

Frangogiannis, N. G. (2017). Fibroblasts and the extracellular matrix in right ventricular disease. *Cardiovasc. Res.* 113, 1453–1464. doi:10.1093/cvr/cvx146.

Gaynor, S. L., Maniar, H. S., Bloch, J. B., Steendijk, P., and Moon, M. R. (2005). Right atrial and ventricular adaptation to chronic right ventricular pressure overload. *Circulation* 112, I-212-I–218. doi:10.1161/CIRCULATIONAHA.104.517789.

George, M. G., Schieb, L. J., Ayala, C., Talwalkar, A., and Levant, S. (2014). Pulmonary hypertension surveillance United States, 2001 to 2010. *Chest* 146, 476–495. doi:10.1378/chest.14-0527.

Giammarresi, A., Bandera, F., Losito, M., Labate, V., Alfonzetti, E., and Guazzi, M. (2019). Effect of sacubitril/valsartan on pulmonary hypertension due to left heart disease. *Eur. Hear. J. - Cardiovasc. Imaging* 20, i1197. Available at: https://esc365.escardio.org/Congress/EuroEcho-Imaging-2018/Clinical-case-poster-session-6-Cross-Modality-and-Multi-Modality-Imaging-To/183002-effect-of-sacubitril-valsartan-on-pulmonary-hypertension-due-to-left-heart-disease-a-case-report#abstract [Accessed October 22, 2019].

Golob, M. J., Wang, Z., Prostrollo, A. J., Hacker, T. A., and Chesler, N. C. (2016). Limiting collagen turnover via collagenase-resistance attenuates right ventricular dysfunction and fibrosis in pulmonary arterial hypertension. *Physiol. Rep.* 4, 1–12. doi:10.14814/phy2.12815.

Gomez, A. D., Zou, H., Bowen, M. E., Liu, X., Hsu, E. W., and McKellar, S. H. (2017). Right ventricular fiber structure as a compensatory mechanism in pressure overload: A computational study. *J. Biomech. Eng.* 139, 0810041–10. doi:10.1115/1.4036485.

Granath, A., Jonsson, B., and Strandell, T. (1964). Circulation in Healthy Old Men, Studied by Right Heart Catheterization at Rest and During Exercise in Supine and Sitting Position. *Acta Med. Scand.* 176, 425–446. doi:10.1111/j.0954-6820.1964.tb00949.x.

Grossman, W., Jones, D., and McLaurin, L. P. (1975). Wall stress and patterns of hypertrophy in the human left ventricle. *J. Clin. Invest.* 56, 56–64. doi:10.1172/JCI108079.

Gu, J., Noe, A., Chandra, P., Al-Fayoumi, S., Ligueros-Saylan, M., Sarangapani, R., et al. (2010). Pharmacokinetics and pharmacodynamics of LCZ696, a novel dual-acting angiotensin receptor-neprilysin inhibitor (ARNi). *J. Clin. Pharmacol.* 50, 401–14. doi:10.1177/0091270009343932.

Guerin, H. A. L., and Elliott, D. M. (2006). Degeneration affects the fiber reorientation of human annulus fibrosus under tensile load. *J. Biomech.* 39, 1410–1418. doi:10.1016/j.jbiomech.2005.04.007.

Guerreiro, D., Lennox, S. C., and Anderson, R. H. (1988). Experimental ventricular hypertrophy in growing pigs. *Int. J. Cardiol.* 21, 311–322. doi:10.1016/0167-5273(88)90108-8.

Guntheroth, W. G. (1974). Changes in left ventricular wall thickness during the cardiac cycle. *J. Appl. Physiol.* 36, 308–312. doi:10.1152/jappl.1974.36.3.308.

Haeck, M. L. A., Scherptong, R. W. C., Marsan, N. A., Holman, E. R., Schalij, M. J., Bax, J. J., et al. (2012). Prognostic value of right ventricular longitudinal peak systolic strain in patients with pulmonary hypertension. *Circ. Cardiovasc. Imaging* 5, 628–636. doi:10.1161/CIRCIMAGING.111.971465.

Han, J. C., Guild, S. J., Pham, T., Nisbet, L., Tran, K., Taberner, A. J., et al. (2018). Left-ventricular energetics in pulmonary arterial hypertension-induced right-ventricular hypertrophic failure. *Front. Physiol.* 8, 1–12. doi:10.3389/fphys.2017.01115.

Healy, L. J., Jiang, Y., and Hsu, E. W. (2011). Quantitative comparison of myocardial fiber structure between mice, rabbit, and sheep using diffusion tensor cardiovascular magnetic resonance. *J. Cardiovasc. Magn. Reson.* 13, 74–82. doi:10.1186/1532-429X-13-74.

Hill, M. R., Simon, M. A., Valdez-Jasso, D., Zhang, W., Champion, H. C., and Sacks, M. S. (2014). Structural and Mechanical Adaptations of Right Ventricle Free Wall Myocardium to Pressure Overload. *Ann. Biomed. Eng.* 42, 2451–2465. doi:10.1007/s10439-014-1096-3.

Hoeper, M. M., and Gibbs, J. S. R. (2014). The changing landscape of pulmonary arterial hypertension and implications for patient care. *Eur. Respir. Rev.* 23, 450–457. doi:10.1183/09059180.00007814.

Hoeper, M. M., Huscher, D., Ghofrani, H. A., Delcroix, M., Distler, O., Schweiger, C., et al. (2013). Elderly patients diagnosed with idiopathic pulmonary arterial hypertension: Results from the COMPERA registry. *Int. J. Cardiol.* 168, 871–880. doi:10.1016/j.ijcard.2012.10.026.

Hoffman, L. M., Jensen, C. C., Chaturvedi, A., Yoshigi, M., and Beckerle, M. C. (2012). Stretch-induced actin remodeling requires targeting of zyxin to stress fibers and recruitment of actin regulators. *Mol. Biol. Cell* 23, 1846–1859. doi:10.1091/mbc.E11-12-1057.

Hosoda, Y., Kawano, K., Yamasawa, F., Ishii, T., Shibata, T., and Inayama, S. (1984). Age-Dependent Changes of Collagen and Elastin Content in Human Aorta and Pulmonary Artery. *Angiology* 35, 615–621. doi:10.1177/000331978403501001.

Humbert, M., Sitbon, O., Yaïci, A., Montani, D., O'Callaghan, D. S., Jaïs, X., et al. (2010). Survival in incident and prevalent cohorts of patients with pulmonary arterial hypertension. *Eur. Respir. J.* 36, 549–555. doi:10.1183/09031936.00057010.

Humphrey, J. D., and Rajagopal, K. R. (2002). A constrained mixture model for growth and remodeling of soft tissues. *Math. Model. Methods Appl. Sci.* 12, 407–430. doi:10.1142/S0218202502001714.

Iborra-Egea, O., Gálvez-Montón, C., Roura, S., Perea-Gil, I., Prat-Vidal, C., Soler-Botija, C., et al. (2017). Mechanisms of action of sacubitril/valsartan on cardiac remodeling: a systems biology approach. *npj Syst. Biol. Appl.* 3. doi:10.1038/s41540-017-0013-4.

Innelli, P., Esposito, R., Olibet, M., Nistri, S., and Galderisi, M. (2009). The impact of ageing on right ventricular longitudinal function in healthy subjects: A pulsed tissue Doppler study. *Eur. J. Echocardiogr.* 10, 491–498. doi:10.1093/ejechocard/jen313.

Izumo, S., Nadal-Ginard, B., and Mahdavi, V. (1988). Protooncogene induction and reprogramming of cardiac gene expression produced by pressure overload. *Proc. Natl. Acad. Sci. U. S. A.* 85, 339–343. doi:10.1073/pnas.85.2.339.

Jacobs, W., Van De Veerdonk, M. C., Trip, P., De Man, F., Heymans, M. W., Marcus, J. T., et al. (2014). The Right Ventricle Explains Sex Differences in Survival in Idiopathic Pulmonary Arterial Hypertension. *Chest* 145, 1230–1236. doi:10.1378/chest.13-1291.

Jane-Lise, S., Corda, S., Chassagne, C., and Rappaport, L. (2000). The extracellular matrix and the cytoskeleton in heart hypertrophy and failure. *Heart Fail. Rev.* 5, 239–250. doi:10.1023/A:1009857403356.

Jang, S., Vanderpool, R. R., Avazmohammadi, R., Lapshin, E., Bachman, T. N., Sacks, M., et al. (2017). Biomechanical and hemodynamic measures of right ventricular diastolic function: Translating tissue biomechanics to clinical relevance. *J. Am. Heart Assoc.* 6, 1–10. doi:10.1161/JAHA.117.006084.

Javani, S., Gordon, M., and Azadani, A. N. (2016). Biomechanical Properties and Microstructure of Heart Chambers: A Paired Comparison Study in an Ovine Model. *Ann. Biomed. Eng.* 44, 3266–3283. doi:10.1007/s10439-016-1658-7.

Kaiser, R., Liu, D., Arias-Loza, P., Hu, K., Grotemeyer, K., and Nordbeck, P. (2020). Right ventricular pressure overload directly affects left ventricular torsion mechanics in patients with precapillary pulmonary hypertension. *PLoS One* 15, e0232544. doi:10.1371/journal.pone.0232544.

Kane, G. C., Sachdev, A., Villarraga, H. R., Ammash, N. M., Oh, J. K., McGoon, M. D., et al. (2016). Impact of age on pulmonary artery systolic pressures at rest and with exercise. *Echo Res. Pract.* 3, 53–61. doi:10.1530/ERP-16-0006.

Kheyfets, V. O., Dufva, M. J., Boehm, M., Tian, X., Qin, X., Tabakh, J. E., et al. (2020). The left ventricle undergoes biomechanical and gene expression changes in response to increased right ventricular pressure overload. *Physiol. Rep.* 8, 1–14. doi:10.14814/phy2.14347.

Komuro, I., Kaida, T., Shibazaki, Y., Kurabayashi, M., Katoh, Y., Hoh, E., et al. (1990). Stretching cardiac myocytes stimulates protooncogene expression. *J. Biol. Chem.* 265, 3595–3598. Available at: http://www.ncbi.nlm.nih.gov/pubmed/2105950 [Accessed April 21, 2020].

Kovalova, S., Necas, J., Cerbak, R., Malik, P., and Vespalec, J. (2005). Echocardiographic volumetry of the right ventricle. *Eur. J. Echocardiogr.* 6, 15–23. doi:10.1016/j.euje.2004.04.009.

Kroon, W., Delhaas, T., Bovendeerd, P., and Arts, T. (2009). Computational analysis of the myocardial structure: Adaptation of cardiac myofiber orientations through deformation. *Med. Image Anal.* 13, 346–353. doi:10.1016/j.media.2008.06.015.

Kural, M. H., Cai, M., Tang, D., Gwyther, T., Zheng, J., and Billiar, K. L. (2012). Planar biaxial characterization of diseased human coronary and carotid arteries for computational modeling. *J. Biomech.* 45, 790–798. doi:10.1016/j.jbiomech.2011.11.019.

Kuroha, M., Isoyama, S., Ito, N., and Takishima, T. (1991). Effects of age on right ventricular hypertrophic response to pressure-Overload in rats. *J. Mol. Cell. Cardiol.* 23, 1177–1190. doi:10.1016/0022-2828(91)90206-2.

Lahm, T., Frump, A. L., Albrecht, M. E., Fisher, A. J., Cook, T. G., Jones, T. J., et al. (2016). 17β-Estradiol mediates superior adaptation of right ventricular function to acute strenuous exercise in female rats with severe pulmonary hypertension. *Am. J. Physiol. - Lung Cell. Mol. Physiol.* 311, L375–L388. doi:10.1152/ajplung.00132.2016.

Lahm, T., Tuder, R. M., and Petrache, I. (2014). Progress in solving the sex hormone paradox in pulmonary hypertension. *Am. J. Physiol. - Lung Cell. Mol. Physiol.* 307, L7–L26. doi:10.1152/ajplung.00337.2013.

Lam, C. S. P., Borlaug, B. A., Kane, G. C., Enders, F. T., Rodeheffer, R. J., and Redfield, M. M. (2009). Age-associated increases in pulmonary artery systolic pressure in the general population. *Circulation* 119, 2663–2670. doi:10.1161/CIRCULATIONAHA.108.838698.

Levine, H. J. (1972). Compliance of the left ventricle. *Circulation* 46, 423–426. doi:10.1161/01.CIR.46.3.423.

Lieber, S. C., Aubry, N., Pain, J., Diaz, G., Kim, S. J., and Vatner, S. F. (2004). Aging increases stiffness of cardiac myocytes measured by atomic force microscopy nanoindentation. *Am. J. Physiol. - Hear. Circ. Physiol.* 287, H645–H651. doi:10.1152/ajpheart.00564.2003.

Lin, D. H. S., and Yin, F. C. P. (1998). A multiaxial constitutive law for mammalian left ventricular myocardium in steady-state barium contracture or tetanus. *J. Biomech. Eng.* 120, 504–517. doi:10.1115/1.2798021.

Liu, A., Hacker, T., Eickhoff, J. C., and Chesler, N. C. (2017a). Estrogen Preserves Pulsatile Pulmonary Arterial Hemodynamics in Pulmonary Arterial Hypertension. *Ann. Biomed. Eng.* 45, 632–643. doi:10.1007/s10439-016-1716-1.

Liu, A., Philip, J., Vinnakota, K. C., Van den Bergh, F., Tabima, D. M., Hacker, T., et al. (2017b). Estrogen maintains mitochondrial content and function in the right ventricle of rats with pulmonary hypertension. *Physiol. Rep.* 5, e13157. doi:10.14814/phy2.13157.

Liu, A., Schreier, D., Tian, L., Eickhoff, J. C., Wang, Z., Hacker, T. A., et al. (2014). Direct and indirect protection of right ventricular function by estrogen in an experimental model of pulmonary arterial hypertension. *Am. J. Physiol. - Hear. Circ. Physiol.* 307, H273–H283. doi:10.1152/ajpheart.00758.2013.

March, H. W., Ross, J. K., and Lower, R. R. (1962). Observations on the behavior of the right ventricular outflow tract, with reference to its developmental origins. *Am. J. Med.* 32, 835–845. doi:10.1016/0002-9343(62)90030-X.

Maslov, M. Y., Foianini, S., Mayer, D., Orlov, M. V., and Lovich, M. A. (2019a). Interaction Between Sacubitril and Valsartan in Preventing Heart Failure Induced by Aortic Valve Insufficiency in Rats. *J. Card. Fail.* In Press. doi:10.1016/j.cardfail.2019.09.008.

Maslov, M. Y., Foianini, S., Mayer, D., Orlov, M. V., and Lovich, M. A. (2019b). Synergy between sacubitril and valsartan leads to hemodynamic, antifibrotic, and exercise tolerance benefits in rats with preexisting heart failure. *Am. J. Physiol. - Hear. Circ. Physiol.* 316, H289–H297. doi:10.1152/ajpheart.00579.2018.

McMurray, J. J. V., Packer, M., Desai, A. S., Gong, J., Lefkowitz, M. P., Rizkala, A. R., et al. (2014). Angiotensin–Neprilysin Inhibition versus Enalapril in Heart Failure. *N. Engl. J. Med.* 371, 993–1004. doi:10.1056/NEJMoa1409077.

Menendez, J. T. (2016). The Mechanism of Action of LCZ696. *Card. Fail. Rev.* 2, 40. doi:10.15420/cfr.2016:1:1.

Methe, K., Bäckdahl, H., Johansson, B. R., Nayakawde, N., Dellgren, G., and Sumitran-Holgersson, S. (2014). An alternative approach to decellularize whole porcine heart. *Biores. Open Access* 3, 327–338. doi:10.1089/biores.2014.0046.

Nakou, E. S., Parthenakis, F. I., Kallergis, E. M., Marketou, M. E., Nakos, K. S., and Vardas, P. E. (2016). Healthy aging and myocardium: A complicated process with various effects in cardiac structure and physiology. *Int. J. Cardiol.* 209, 167–175. doi:10.1016/j.ijcard.2016.02.039.

Nemavhola, F. (2017). Biaxial quantification of passive porcine myocardium elastic properties by region. *Eng. Solid Mech.* 5, 155–166. doi:10.5267/j.esm.2017.6.003.

Nguyen, T. D., Liang, R., Woo, S. L.-Y., Burton, S. D., Wu, C., Almarza, A., et al. (2009). Effects of cell seeding and cyclic stretch on the fiber remodeling in an extracellular matrix-derived bioscaffold. *Tissue Eng. - Part A* 15, 957–963. doi:10.1089/ten.tea.2007.0384.

Nielsen, E., Smerup, M., Agger, P., Frandsen, J., Ringgard, S., Pedersen, M., et al. (2009). Normal right ventricular three-dimensional architecture, as assessed with diffusion tensor magnetic resonance imaging, is preserved during experimentally induced right ventricular hypertrophy. *Anat. Rec.* 292, 640–651. doi:10.1002/ar.20873.

Omann, C., Agger, P., Bøgh, N., Laustsen, C., Ringgaard, S., Stephenson, R. S., et al. (2019). Resolving the natural myocardial remodelling brought upon by cardiac contraction; A porcine ex-vivo cardiovascular magnetic resonance study of the left and right ventricle. *J. Cardiovasc. Magn. Reson.* 21, 35. doi:10.1186/s12968-019-0547-2.

Park, D. W., Sebastiani, A., Yap, C. H., Simon, M. A., and Kim, K. (2016). Quantification of coupled stiffness and fiber orientation remodeling in hypertensive rat right-ventricular myocardium using 3D ultrasound speckle tracking with biaxial testing. *PLoS One* 11, e0165320. doi:10.1371/journal.pone.0165320.

Partington, S. L., and Kilner, P. J. (2017). How to image the dilated right ventricle. *Circ. Cardiovasc. Imaging* 10, 1–11. doi:10.1161/CIRCIMAGING.116.004688.

Perona, P., and Malik, J. (1990). Scale-Space and Edge Detection Using Anisotropic Diffusion. *IEEE Trans. Pattern Anal. Mach. Intell.* 12, 629–639. doi:10.1109/34.56205.

Pfau, D., Thorn, S. L., Zhang, J., Mikush, N., Renaud, J. M., Klein, R., et al. (2019). Angiotensin Receptor Neprilysin Inhibitor Attenuates Myocardial Remodeling and Improves Infarct Perfusion in Experimental Heart Failure. *Sci. Rep.* 9. doi:10.1038/s41598-019-42113-0.

Pu, Q., Brassard, P., Javeshghani, D. M., Iglarz, M., Webb, R. L., Amiri, F., et al. (2008). Effects of combined AT1receptor antagonist/NEP inhibitor on vascular remodeling and cardiac fibrosis in SHRSP. *J. Hypertens.* 26, 322–333. doi:10.1097/HJH.0b013e3282f16aaf.

Püspöki, Z., Storath, M., Sage, D., and Unser, M. (2016). Transforms and operators for directional bioimage analysis: A survey. *Adv. Anat. Embryol. Cell Biol.* 219, 69–93. doi:10.1007/978-3-319-28549-8_3.

Qin, X., Cong, Z., Jiang, R., Shen, M., Wagner, M. B., Kirshbom, P., et al. (2013). Extracting cardiac myofiber orientations from high frequency ultrasound images. in *Medical Imaging 2013: Ultrasonic Imaging, Tomography, and Therapy* (International Society for Optics and Photonics), 867507. doi:10.1117/12.2006494.

Qin, X., and Fei, B. (2014). Measuring myofiber orientations from high-frequency ultrasound images using multiscale decompositions. *Phys. Med. Biol.* 59, 3907–3924. doi:10.1088/0031-9155/59/14/3907.

Raghavan, M. L., and Vorp, D. A. (2000). Toward a biomechanical tool to evaluate rupture potential of abdominal aortic aneurysm: Identification of a finite strain constitutive model and evaluation of its applicability. *J. Biomech.* 33, 475–482. doi:10.1016/S0021-9290(99)00201-8.

Rain, S., Handoko, M. L., Trip, P., Gan, C. T. J., Westerhof, N., Stienen, G. J., et al. (2013). Right ventricular diastolic impairment in patients with pulmonary arterial hypertension. *Circulation* 128, 2016–2025. doi:10.1161/CIRCULATIONAHA.113.001873.

Rezakhaniha, R., Agianniotis, A., Schrauwen, J. T. C., Griffa, A., Sage, D., Bouten, C. V. C., et al. (2012). Experimental investigation of collagen waviness and orientation in the arterial adventitia using confocal laser scanning microscopy. *Biomech. Model. Mechanobiol.* 11, 461–473. doi:10.1007/s10237-011-0325-z.

Richter, M. J., Badagliacca, R., Wan, J., Vanderpool, R., Dalmer, A., Ghofrani, H. A., et al. (2020). Right ventricular dyssynchrony: from load-independent right ventricular function to wall stress in severe pulmonary arterial hypertension. *Pulm. Circ.* 10, 1–4. doi:10.1177/2045894020925759.

Rouhana, S., Farah, C., Roy, J., Finan, A., Rodrigues de Araujo, G., Bideaux, P., et al. (2019). Early calcium handling imbalance in pressure overload-induced heart failure with nearly normal left ventricular ejection fraction. *Biochim. Biophys. Acta - Mol. Basis Dis.* 1865, 230–242. doi:10.1016/j.bbadis.2018.08.005.

Sachdev, A., Villarraga, H. R., Frantz, R. P., McGoon, M. D., Hsiao, J. F., Maalouf, J. F., et al. (2011). Right ventricular strain for prediction of survival in patients with pulmonary arterial hypertension. *Chest* 139, 1299–1309. doi:10.1378/chest.10-2015.

Sacks, M. S. (1999). A Method for Planar Biaxial Mechanical Testing That Includes In-Plane Shear. *J. Biomech. Eng.* 121, 551–555. doi:10.1115/1.2835086.

Sacks, M. S. (2003). Incorporation of Experimentally-Derived Fiber Orientation into a Structural Constitutive Model for Planar Collagenous Tissues. *J. Biomech. Eng.* 125, 280–287. doi:10.1115/1.1544508.

Sacks, M. S., and Chuong, C. J. (1993). Biaxial mechanical properties of passive right ventricular free wall myocardium. *J. Biomech. Eng.* 115, 202–205. doi:10.1115/1.2894122.

Santamore, W. P., and Dell'Italia, L. J. (1998). Ventricular interdependence: Significant left ventricular contributions to right ventricular systolic function. *Prog. Cardiovasc. Dis.* 40, 289–308. doi:10.1016/S0033-0620(98)80049-2.

Schmuck, E. G., Hacker, T. A., Schreier, D. A., Chesler, N. C., and Wang, Z. (2019). Beneficial effects of mesenchymal stem cell delivery via a novel cardiac bioscaffold on right ventricles of pulmonary arterial hypertensive rats. *Am. J. Physiol. - Hear. Circ. Physiol.* 316, H1005–H1013. doi:10.1152/ajpheart.00091.2018.

Schupp, M., Bowry, R., and Tousignant, C. P. (2007). Right Ventricular Tissue Doppler Parameters in a Patient with Massive Pulmonary Embolus. *J. Am. Soc. Echocardiogr.* 20, 198.e6-198.e10. doi:10.1016/j.echo.2006.09.004.

Sharifi Kia, D., Benza, E., Bachman, T. N., Tushak, C., Kim, K., and Simon, M. A. (2020). Angiotensin Receptor-Neprilysin Inhibition Attenuates Right Ventricular Remodeling in Pulmonary Hypertension. *J. Am. Heart Assoc.* 9, e015708. doi:10.1161/JAHA.119.015708.

Shen, Y., Goncharov, D. A., Avolio, T., Ray, A., Okorie, E., DeLisser, H., et al. (2020). Differential effects of integrin-linked kinase inhibitor Cpd22 on severe pulmonary hypertension in male and female rats. *Pulm. Circ.* 10, 1–12. doi:10.1177/2045894019898593.

Sicard, D., Haak, A. J., Choi, K. M., Craig, A. R., Fredenburgh, L. E., and Tschumperlin, D. J. (2018). Aging and anatomical variations in lung tissue stiffness. *Am. J. Physiol. - Lung Cell. Mol. Physiol.* 314, L946–L955. doi:10.1152/ajplung.00415.2017.

Simon, M. A., Vanderpool, R. R., Nouraie, M., Bachman, T. N., White, P. M., Sugahara, M., et al. (2016). Acute hemodynamic effects of inhaled sodium nitrite in pulmonary hypertension associated with heart failure with preserved ejection fraction. *JCI Insight* 1, 89620. doi:10.1172/jci.insight.89620.

Solomon, S. D., McMurray, J. J. V., Anand, I. S., Ge, J., Lam, C. S. P., Maggioni, A. P., et al. (2019). Angiotensin–Neprilysin Inhibition in Heart Failure with Preserved Ejection Fraction. *N. Engl. J. Med.* doi:10.1056/nejmoa1908655.

Sommer, G., Schriefl, A. J., Andrä, M., Sacherer, M., Viertler, C., Wolinski, H., et al. (2015). Biomechanical properties and microstructure of human ventricular myocardium. *Acta Biomater.* 24, 172–192. doi:10.1016/j.actbio.2015.06.031.

Stokke, T. M., Hasselberg, N. E., Smedsrud, M. K., Sarvari, S. I., Haugaa, K. H., Smiseth, O. A., et al. (2017). Geometry as a confounder when assessing ventricular systolic function: comparison between ejection fraction and strain. *J. Am. Coll. Cardiol.* 70, 942–954. doi:10.1016/j.jacc.2017.06.046.

Streeter, D. D., and Hanna, W. T. (1973). Engineering mechanics for successive states in canine left ventricular myocardium. II. Fiber angle and sarcomere length. *Circ. Res.* 33, 656–664. doi:10.1161/01.RES.33.6.656.

Streeter, D. D., Spotnitz, H. M., Patel, D. P., Ross, J., and Sonnenblick, E. H. (1969). Fiber orientation in the canine left ventricle during diastole and systole. *Circ. Res.* 24, 339–347. doi:10.1161/01.RES.24.3.339.

Stroud, J. D., Baicu, C. F., Barnes, M. A., Spinale, F. G., and Zile, M. R. (2002). Viscoelastic properties of pressure overload hypertrophied myocardium: Effect of serine protease treatment. *Am. J. Physiol. - Hear. Circ. Physiol.* 282, H2324–H2335. doi:10.1152/ajpheart.00711.2001.

Tabima, D. M., Philip, J. L., and Chesler, N. C. (2017). Right ventricular-pulmonary vascular interactions. *Physiology* 32, 346–356. doi:10.1152/physiol.00040.2016.

Tadic, M., Cuspidi, C., Bombelli, M., and Grassi, G. (2018). Right heart remodeling induced by arterial hypertension: Could strain assessment be helpful? *J. Clin. Hypertens.* 20, 400–407. doi:10.1111/jch.13186.

Tello, K., Dalmer, A., Axmann, J., Vanderpool, R., Ghofrani, H. A., Naeije, R., et al. (2019). Reserve of Right Ventricular-Arterial Coupling in the Setting of Chronic Overload. *Circ. Heart Fail.* 12, e005512. doi:10.1161/CIRCHEARTFAILURE.118.005512.

Tello, K., Richter, M. J., Yogeswaran, A., Ghofrani, H. A., Naeije, R., Vanderpool, R., et al. (2020). Sex Differences in Right Ventricular-pulmonary Arterial Coupling in Pulmonary Arterial Hypertension. *Am. J. Respir. Crit. Care Med.*, In Press. doi:10.1164/rccm.202003-0807le.

Tezuka, F., Hart, W., Lange, P. E., and Nürnberg, J. H. (1990). Muscle Fiber Orientation in the Development and Regression of Right Ventricular Hypertrophy in Pigs. *Pathol. Int.* 40, 402–407. doi:10.1111/j.1440-1827.1990.tb01579.x.

Thiwanka Wijeratne, D., Lajkosz, K., Brogly, S. B., Diane Lougheed, M., Jiang, L., Housin, A., et al. (2018). Increasing Incidence and Prevalence of World Health Organization Groups 1 to 4 Pulmonary Hypertension: A Population-Based Cohort Study in Ontario, Canada. *Circ. Cardiovasc. Qual. Outcomes* 11, 1–13. doi:10.1161/CIRCOUTCOMES.117.003973.

Thunes, J. R., Pal, S., Fortunato, R. N., Phillippi, J. A., Gleason, T. G., Vorp, D. A., et al. (2016). A structural finite element model for lamellar unit of aortic media indicates heterogeneous stress field after collagen recruitment. *J. Biomech.* 49, 1562–1569. doi:10.1016/j.jbiomech.2016.03.034.

Thunes, J. R., Phillippi, J. A., Gleason, T. G., Vorp, D. A., and Maiti, S. (2018). Structural modeling reveals microstructure-strength relationship for human ascending thoracic aorta. *J. Biomech.* 71, 84–93. doi:10.1016/j.jbiomech.2018.01.037.

Trivedi, R. K., Polhemus, D. J., Li, Z., Yoo, D., Koiwaya, H., Scarborough, A., et al. (2018). Combined angiotensin receptor-neprilysin inhibitors improve cardiac and vascular function via increased NO bioavailability in heart failure. *J. Am. Heart Assoc.* 7, e008268. doi:10.1161/JAHA.117.008268.

Tsamis, A., Bothe, W., Kvitting, J. P. E., Swanson, J. C., Miller, D. C., and Kuhl, E. (2011). Active contraction of cardiac muscle: In vivo characterization of mechanical activation sequences in the beating heart. *J. Mech. Behav. Biomed. Mater.* 4, 1167–1176. doi:10.1016/j.jmbbm.2011.03.027.

Valdez-Jasso, D., Simon, M. A., Champion, H. C., and Sacks, M. S. (2012). A murine experimental model for the mechanical behaviour of viable right-ventricular myocardium. *J. Physiol.* 590, 4571–4584. doi:10.1113/jphysiol.2012.233015.

Van Essen, G. J., Hekkert, M. T. L., Sorop, O., Heinonen, I., Van Der Velden, J., Merkus, D., et al. (2018). Cardiovascular function of modern pigs does not comply with allometric scaling laws. *Sci. Rep.* 8, 1–10. doi:10.1038/s41598-017-18775-z.

Vanderpool, R. R., Pinsky, M. R., Naeije, R., Deible, C., Kosaraju, V., Bunner, C., et al. (2015). RV-pulmonary arterial coupling predicts outcome in patients referred for pulmonary hypertension. *Heart* 101, 37–43. doi:10.1136/heartjnl-2014-306142.

Vanderpool, R. R., Puri, R., Osorio, A., Wickstrom, K., Desai, A. A., Black, S. M., et al. (2020). Surfing the right ventricular pressure waveform: methods to assess global, systolic and diastolic RV function from a clinical right heart catheterization. *Pulm. Circ.* 10, 1–11. doi:10.1177/2045894019850993.

Vélez-Rendón, D., Pursell, E. R., Shieh, J., and Valdez-Jasso, D. (2019). Relative Contributions of Matrix and Myocytes to Biaxial Mechanics of the Right Ventricle in Pulmonary Arterial Hypertension. *J. Biomech. Eng.* 141, 0910111–0910118. doi:10.1115/1.4044225.

Vetter, F. J., Simons, S. B., Mironov, S., Hyatt, C. J., and Pertsov, A. M. (2005). Epicardial fiber organization in swine right ventricle and its impact on propagation. *Circ. Res.* 96, 244–251. doi:10.1161/01.RES.0000153979.71859.e7.

Voelke, N. F., Natarajan, R., Drake, J. I., and Bogaard, H. J. (2011). Right ventricle in pulmonary hypertension. *Compr. Physiol.* 1, 525–540. doi:10.1002/cphy.c090008.

Voeller, R. K., Aziz, A., Maniar, H. S., Ufere, N. N., Taggar, A. K., Bernabe, N. J., et al. (2011). Differential modulation of right ventricular strain and right atrial mechanics in mild vs. severe pressure overload. *Am. J. Physiol. - Hear. Circ. Physiol.* 301, H2362–H2371. doi:10.1152/ajpheart.00138.2011.

Von Lueder, T. G., Sangaralingham, S. J., Wang, B. H., Kompa, A. R., Atar, D., Burnett, J. C., et al. (2013). Renin-angiotensin blockade combined with natriuretic peptide system augmentation novel therapeutic concepts to combat heart failure. *Circ. Hear. Fail.* 6, 594–605. doi:10.1161/CIRCHEARTFAILURE.112.000289.

Walker, E. M., Nillas, M. S., Mangiarua, E. I., Cansino, S., Morrison, R. G., Perdue, R. R., et al. (2006). Age-associated changes in hearts of male fischer 344/Brown Norway F1 rats. *Ann. Clin. Lab. Sci.* 36, 427–438. Available at: www.annclinlabsci.org [Accessed June 23, 2020].

Wang, Z., Patel, J. R., Schreier, D. A., Hacker, T. A., Moss, R. L., and Chesler, N. C. (2018). Organ-level right ventricular dysfunction with preserved Frank-Starling mechanism in a mouse model of pulmonary arterial hypertension. *J. Appl. Physiol.* 124, 1244–1253. doi:10.1152/japplphysiol.00725.2017.

Wang, Z., Schreier, D. A., Hacker, T. A., and Chesler, N. C. (2013). Progressive right ventricular functional and structural changes in a mouse model of pulmonary arterial hypertension. *Physiol. Rep.* 1, 1–11. doi:10.1002/phy2.184.

Weickert, J. (1999). Coherence-enhancing diffusion filtering. *Int. J. Comput. Vis.* 31, 111–127. doi:10.1023/A:1008009714131.

Wilson, W., Driessen, N. J. B., van Donkelaar, C. C., and Ito, K. (2006). Prediction of collagen orientation in articular cartilage by a collagen remodeling algorithm. *Osteoarthr. Cartil.* 14, 1196–1202. doi:10.1016/j.joca.2006.05.006.

Yoshigi, M., Clark, E. B., and Yost, H. J. (2003). Quantification of stretch-induced cytoskeletal remodeling in vascular endothelial cells by image processing. *Cytometry* 55A, 109–118. doi:10.1002/cyto.a.10076.

Zannad, F., and Ferreira, J. P. (2019). Is Sacubitril/Valsartan Antifibrotic? *J. Am. Coll. Cardiol.* 73, 807–809. doi:10.1016/j.jacc.2018.11.041.

Zhang, W., Feng, Y., Lee, C.-H., Billiar, K. L., and Sacks, M. S. (2015). A Generalized Method for the Analysis of Planar Biaxial Mechanical Data Using Tethered Testing Configurations. *J. Biomech. Eng.* 137, 064501–13. doi:10.1115/1.4029266.

Zile, M. R., O'Meara, E., Claggett, B., Prescott, M. F., Solomon, S. D., Swedberg, K., et al. (2019). Effects of Sacubitril/Valsartan on Biomarkers of Extracellular Matrix Regulation in Patients With HFrEF. *J. Am. Coll. Cardiol.* 73, 795–806. doi:10.1016/j.jacc.2018.11.042.